

# Photocurrent in Organic Solar Cells

Dissertation zur Erlangung des  
naturwissenschaftlichen Doktorgrades  
der Julius-Maximilians-Universität Würzburg



vorgelegt von  
**Markus Harald Mingebach**

aus  
Limburg a. d. Lahn

Würzburg 2012

Eingereicht am:  
bei der Fakultät für Physik und Astronomie

1. Gutachter: Prof. Dr. Vladimir Dyakonov  
2. Gutachter: Prof. Dr. Derck Schlettwein  
der Dissertation.

1. Prüfer: Prof. Dr. Vladimir Dyakonov  
2. Prüfer: Prof. Dr. Derck Schlettwein  
3. Prüfer: Prof. Dr. Wolfgang Kinzel  
im Promotionskolloquium.

Tag des Promotionskolloquiums: 02.11.2012

Doktorurkunde ausgehändigt am:

» ICH WEISS NICHT, WIE MICH DIE WELT EINST SEHEN WIRD. WAS MICH BETRIFFT, SO KOMME ICH MIR VOR WIE EIN KLEINER JUNGE, DER AM STRAND SPIELT UND AB UND ZU EINEN STEIN ODER EINE MUSCHEL FINDET, DIE SCHÖNER ALS DIE GEWÖHNLICHEN SIND, WÄHREND DER GROSSE OZEAN DER WAHRHEIT UNENTDECKT VOR MIR LIEGT. «

Sir Isaac Newton (1643-1727)

---

## Kurzfassung

Ein relativ neuer Ansatz für eine günstige Massenproduktion flexibler Solarzellen ist dabei die organische Photovoltaik. Obwohl die Wirkungsgrade in den letzten Jahren schnell anstiegen, sind weitere Verbesserungen für eine erfolgreiche Markteinführung dringend nötig. Ein wichtiger Faktor ist dabei der Photostrom einer Solarzelle, der als Differenz zwischen Hell- und Dunkelstrom definiert ist. Im Gegensatz zu anorganischen Solarzellen ist dieser im Falle der organischen "bulk heterojunction" (Heterogemisch, Abk.: BHJ) Solarzellen von der angelegten Spannung abhängig. Dies führt zu einer Reduzierung des Füllfaktors und so zu einem noch stärkeren Einflusses des Photostroms auf die Leistung der Solarzelle. Es ist daher äußerst wichtig die grundlegenden, den Photostrom bestimmenden Prozesse zu verstehen, um die Leistung der organischen Solarzellen weiter steigern zu können.

Zunächst wurde der Photostrom von P3HT:PC<sub>61</sub>BM Solarzellen mittels einer gepulsten Messmethode untersucht, die störende Einflüsse durch das Erwärmen der Probe unter kontinuierlicher Beleuchtung verhindern soll. Der resultierende Photostrom wies einen dem Tangens Hyperbolicus ähnlichen Verlauf auf und zeigte dabei eine Punktsymmetrie, deren Ursprung und Bedeutung im Verlauf dieser Arbeit genauer diskutiert werden. Für die Beschreibung des spannungsabhängigen Photostroms wird außerdem ein kombiniertes Modell vorgestellt, welches auf den Theorien von Braun-Onsager und Sokel-Hughes für die feldabhängige Polaronenpaartrennung bzw. die Ladungsträgerextraktion basiert

Nach der makroskopischen Betrachtung des Photostroms wird sich der Fokus dann auf die grundlegenden, den Photostrom bestimmenden Prozesse verschoben: Photogeneration und Rekombination der Ladungsträger. Die Feldabhängigkeit dieser Prozesse wurde dabei mittels time-delayed collection field (TDCF) Messungen an den beiden Referenz-Systemen P3HT:PC<sub>61</sub>BM und MDMO-PPV:PC<sub>61</sub>BM untersucht. Dadurch ließen sich neben deutlichen Unterschieden in der nichtgeminalen Rekombinationsdynamik freier Ladungsträger auch bei deren Photogeneration zwei unterschiedliche dominierende Prozesse identifizieren: Im ersten Szenario werden freie Ladungsträger über einen relaxierten Ladungstransferzustand ("charge transfer state" — CTS) generiert. Dieser Prozess ist jedoch durch einen deutlichen Einfluss der geminalen Rekombination stark feldabhängig und somit weniger effizient. Im zweiten Szenario werden die freien Ladungsträger entweder direkt oder über einen angeregten ("hot") CTS erzeugt. Ähnliche Versuche wurden zudem für zwei neuartige Polymere mit niedrigen Bandlücken präsentiert, die sich jeweils nur durch das Brückenatom im Cyclopentadithiophen unterscheiden (PCPDTBT:PC<sub>71</sub>BM im Vergleich zu Si-PCPDTBT:PC<sub>71</sub>BM). Dies hatte jedoch deutliche Auswir-

kungen auf die Photogeneration freier Ladungsträger und die Morphologie der aktiven Schicht. Die entsprechenden Ergebnisse wurden dann in Relation zu den Strom–Spannungs–Kennlinien gesetzt, um die deutlichen Unterschiede in der Effizienz der Solarzellen zu diskutieren.

Ein weiterer wichtiger, die Leistung einer Solarzelle begrenzender Parameter ist deren Diffusionsspannung (built-in potential,  $V_{Bi}$ ). In der Physik halbleitender pn–Übergänge ist die Mott–Schottky Analyse eine etablierte Methode um  $V_{Bi}$  zu bestimmen. Diese wurde ursprünglich für abrupte pn–Übergänge hergeleitet, weshalb hier deren Gültigkeit für organische BHJ Solarzellen — und damit ein bipolares, effektives Medium — diskutiert wird. Die experimentellen Ergebnisse ebenso wie die Widersprüche zur Mott–Schottky Theorie deuten darauf hin, dass eine direkte Übertragbarkeit dieser Methode auf organische BHJ Solarzellen nicht gegeben ist.

Abschließend werden noch die Ergebnisse des MOPS-Projekts (Massengedruckte Organische Papier-Solarzellen) präsentiert, in dessen Verlauf die ersten komplett auf Papier gedruckten Solarzellen entwickelt wurden.

---

## Abstract

A quite new approach to low-cost mass production of flexible solar cells are organic photovoltaics. Even though the device efficiencies increased rapidly during the last years, further improvements are essential for a successful market launch. One important factor influencing the device efficiency is the photocurrent of a solar cell, which is defined as the difference between the current under illumination and in the dark. In case of organic bulk heterojunction (BHJ) solar cells it is — in contrast to inorganic devices — dependent on the applied bias voltage. The voltage dependence results in a reduced fill factor and thus an even more pronounced influence of the photocurrent on the device efficiency. It is therefore crucial to understand the underlying processes determining the photocurrent in order to be able to further improve the solar cell performance.

In a first step the photocurrent of P3HT:PC<sub>61</sub>BM devices was investigated by a pulsed measurement technique in order to prevent disturbing influences due to device heating under continuous illumination. The resulting photocurrent was hyperbolic tangent like and featured a point symmetry, whose origin and meaning were discussed. In addition, the photocurrent was described by a combined model of Braun–Onsager and Sokel–Hughes theory for field dependent polaron pair dissociation and charge extraction, respectively.

After this macroscopic view on the photocurrent, the focus of this work moves to the more basic processes determining the photocurrent: charge photogeneration and recombination. In a comparative study the field-dependence of these was investigated by time-delayed collection field (TDCF) measurements for two well-known reference systems, namely P3HT:PC<sub>61</sub>BM and MDMO-PPV:PC<sub>61</sub>BM. It was possible to identify two different dominating scenarios for the generation of free charge carriers. The first one — via a thermalized charge transfer state (CTS) — is clearly influenced by geminate recombination and therefore less efficient. In the second scenario, the free charge carriers are either generated directly or via an excited, “hot” CTS. In addition, clear differences in the nongeminate recombination dynamics of both material systems were found. Similar studies were also presented with two modern low bandgap polymers which only differ by the bridging atom in the cyclopentadithiophene (PCPDTBT:PC<sub>71</sub>BM vs. Si-PCPDTBT:PC<sub>71</sub>BM). Such small changes in the chemical structure were already sufficient to affect the charge photogeneration as well as the morphology of the blend. These findings were set into relation to current–voltage characteristics in order to discuss the origin of the clear differences in the solar cell performance of both materials.

Another crucial parameter limiting the solar cell efficiency is the built-in potential of a device. Within the range of semiconducting pn-junctions,

## IV

---

Mott–Schottky analysis is an established method to determine the built-in potential. As it was originally derived for abrupt pn-junctions, its validity for organic BHJ solar cells — a bipolar, effective medium — was discussed. Experimental findings as well as the contradictions to Mott–Schottky theory indicated, that a direct transfer of this method to organic photovoltaics is not appropriate.

Finally, the results obtained in the framework of the MOPS-project (Mas-sengedruckte Organische Papier-Solarzellen) will be presented, in which the first completely roll-to-roll printed paper solar cells were realized.

# Contents

<b>1</b>	<b>Introduction</b>	<b>1</b>
<b>2</b>	<b>Organic Photovoltaics</b>	<b>5</b>
2.1	Historical Overview . . . . .	5
2.2	Organic Semiconductors . . . . .	6
2.3	Working Principles of Organic BHJ Solar Cells . . . . .	11
<b>3</b>	<b>Photocurrent Generation</b>	<b>15</b>
3.1	Polaron Pair Generation . . . . .	15
3.2	Polaron Pair Dissociation . . . . .	16
3.3	Charge Extraction . . . . .	18
3.4	Photocurrent Model . . . . .	20
<b>4</b>	<b>Recombination Dynamics</b>	<b>21</b>
4.1	Geminate Recombination . . . . .	21
4.2	Nongeminate Recombination . . . . .	23
4.3	Langevin Theory . . . . .	24
<b>5</b>	<b>Experimental</b>	<b>27</b>
5.1	Organic Solar Cell Materials . . . . .	27
5.2	Sample Preparation . . . . .	30
5.3	Experimental Setups and Techniques . . . . .	31
5.3.1	Pulsed Photocurrent . . . . .	31
5.3.2	Time-Delayed Collection Field . . . . .	34
5.3.3	Impedance Spectroscopy . . . . .	40
<b>6</b>	<b>Voltage-Dependent Photocurrent</b>	<b>47</b>
6.1	Point of Optimal Symmetry . . . . .	47
6.1.1	Origin of the Point of Optimal Symmetry . . . . .	48
6.1.2	Voltage-Independent Offset . . . . .	50
6.2	Modeling the Photocurrent . . . . .	52
6.3	Conclusion . . . . .	55
<b>7</b>	<b>Charge Photogeneration and Recombination</b>	<b>57</b>
7.1	Field-Dependent Polaron Pair Dissociation . . . . .	57
7.2	Nongeminate Recombination . . . . .	61
7.3	Conclusion . . . . .	63



---

<b>8</b>	<b>Influence of the Bridging Atom on Charge Photogeneration</b>	<b>65</b>
8.1	Field-Dependent Charge Photogeneration . . . . .	65
8.2	Morphological Aspects . . . . .	67
8.3	Influence on the Current–Voltage Characteristics . . . . .	69
8.4	Conclusion . . . . .	71
<b>9</b>	<b>Validity of Mott–Schottky Analysis in Organic BHJ Solar Cells</b>	<b>73</b>
9.1	Mott–Schottky Analysis . . . . .	73
9.2	Conclusion . . . . .	77
<b>10</b>	<b>Printed Paper Photovoltaics - 3PV</b>	<b>79</b>
10.1	Printing Organic Photovoltaics on Paper . . . . .	79
10.2	Results and Discussion . . . . .	80
10.3	Conclusion . . . . .	85
<b>11</b>	<b>Conclusion</b>	<b>87</b>
	<b>Bibliography</b>	<b>93</b>
<b>A</b>	<b>List of Publications</b>	<b>105</b>
<b>B</b>	<b>Danksagung</b>	<b>109</b>
<b>C</b>	<b>Lebenslauf</b>	<b>111</b>
<b>D</b>	<b>Eidesstattliche Erklärung</b>	<b>113</b>

## CHAPTER 1

# Introduction

---

Renewable energies are a topic of strongly increasing interest during the last years, since fossil fuels such as crude oil already reached their global production peak in 2006, as estimated by the German Energy Watch Group [1] and the International Energy Agency [2]. Nevertheless the worldwide energy demand will further increase and hence, there will be a need for alternative energy sources. One possibility is the use of nuclear energy, but recent disasters as in Fukushima 2011 show that this technology is still hard to control and a safe energy production cannot be guaranteed. Another problem that has not been solved yet is the long term storage of the resulting radioactive waste. For future generations we therefore need a sustainable energy production that also reduces the emission of environmentally harmful carbon dioxide.

Besides wind, water and bio-energy, solar energy conversion is a fast growing part of renewable energies. In Germany, for example, solar collectors generated in 2011 more than 18 billion kilowatt hours electricity, which means an increase by 60% in comparison to the year before. Still, the contribution to the German energy market is only about 3%, but the fast growth will lead to a market share of about 10% in 2020 [3].

The first modern silicon solar cell was developed by Daryl Chapin, Calvin Souther Fuller and Gerald Pearson at the Bell Laboratories in 1954 with a power conversion efficiency (PCE) of about 6% [4]. During the following decades the PCE of these monocrystalline p-n junctions increased up to 25% [5]. This is close to the theoretically calculated upper limit of PCE by W. Shockley and H. J. Queisser, which is about 30% for a single layer silicon solar cell [6]. In their calculations the authors assumed sun and solar cell to be black bodies with 6000 K and 300 K, respectively, and evaluated light absorption versus radiative recombination losses inside the solar cell. Due to the band gap of 1.1 eV, all sun light with energies below this threshold cannot be absorbed, which is about half of the AM 1.5 spectrum. In addition the excess energy above 1.1 eV can only be converted into thermal energy in the crystal and hence is lost as well.

The major obstacle of photovoltaic energy conversion is the high production costs of the solar modules, especially in the case of silicon based technologies. In order to further improve the impact of solar energy conversion on the future energy market, the production costs need to be reduced while the PCE

needs to further increase. One promising step is the use of thin film technologies as copper indium gallium (di)selenide (CIGS) or cadmium telluride (CdTe) solar cells. Due to the high absorption coefficients of these materials, thin layers ( $\sim \mu\text{m}$ ) are sufficient to absorb almost all of the incoming light. Besides the advantage of low production costs due to the small amount of needed material, this technology also allows for the creation of multilayer systems (multiple absorbing layers with different band gaps), which have a higher Shockley–Queisser limit than single junction solar cells. Nevertheless, these technologies also have a major drawback. In order to enable high device efficiencies the use of rare elements such as indium or gallium is essential. Due to their application in many mass products such as mobile phones and flat screens they will become much more expensive in future, counteracting the aim of reducing production costs.

A totally new approach for cheap mass production of thin film solar cells is the use of organic semiconductors. These are based on the discovery of conductive polymers by Hideki Shirakawa, Alan MacDiarmid and Alan J. Heeger, who were awarded the Nobel prize in chemistry in the year 2000. Organic light emitting diodes (OLED) based on these polymers have already been established on the market and lead the way for organic solar cells. The PCE of organic bulk heterojunction (BHJ) solar cells increased during the last 15 years rapidly up to 10% in laboratory scale and exceeded 4% for solar modules [5], as shown in Figure 1.1. The big advantage of this new approach

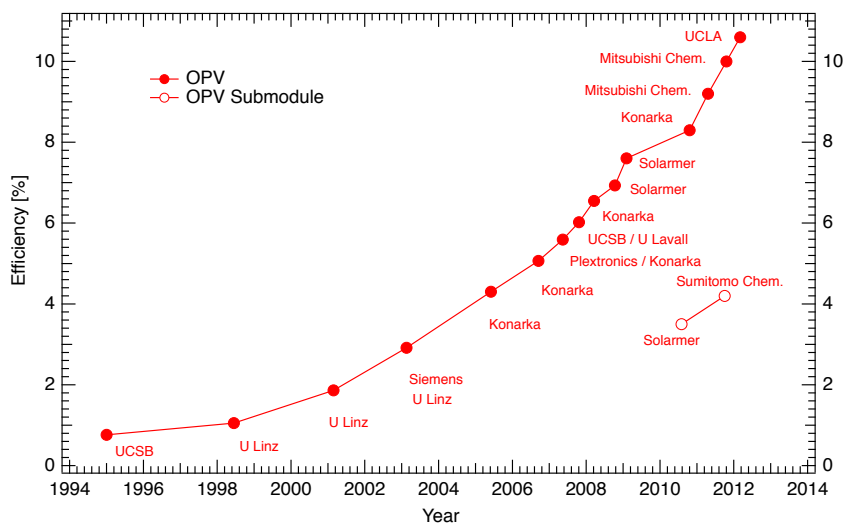


Figure 1.1: Development of the power conversion efficiency of organic bulk heterojunction solar cells in a laboratory scale (filled circles) and for entire modules (open circles), after [5]

is the applicability of fast mass printing techniques such as roll-to-roll printing that allow for a high production output with a very low material consumption. Furthermore cheap flexible substrates such as plastic foils or even paper (as will be shown in chapter 10) help to decrease production costs far below 1 USD per Watt peak [7]. Hence, to enable a successful commercialization of organic solar cells, the module efficiency needs to further increase to 10% as well as the device lifetimes that should reach about 10 years [8]. To realize this goal, the basic working principles of organic BHJ solar cells need to be understood in more detail.

In this thesis I will first give a short historical overview about the development of organic BHJ solar cells and their basic working principles. After presenting sample preparation techniques and experimental methods, I will discuss the experimental results concerning photocurrent generation and charge carrier recombination dynamics for different donor-acceptor blends. Finally, I will introduce the first roll-to-roll printed organic BHJ solar cell on a cheap and environmentally friendly paper substrate, marking an important step towards large scale production of organic solar cells.



# Organic Photovoltaics

---

## 2.1 Historical Overview

The first step towards organic solar cells was the discovery of dark conductivity in halogen doped organic compounds in 1954. Nevertheless, the conductivity was rather low and many of the compounds were not stable [9]. It took almost two decades until the first highly conductive polymers were synthesized, by doping polyacetylene with different halogens [10]. In the year 2000, Hideki Shirakawa, Alan MacDiarmid and Alan J. Heeger were awarded with the Nobel prize in chemistry for their discovery.

Based on these highly conductive polymers, the first organic solar cells were developed, which consisted of a single organic layer between two electrodes. The power conversion efficiencies of these first organic single layer cells were clearly below 1%. This rather poor performance was due to the difficulties dissociating the strongly Coulomb-bound excitons that are generated via light absorption. The thermal energy is not high enough to dissociate them effectively and hence, only the excitons that reach one of the contacts within their short diffusion length can be dissociated. In addition, this process is very inefficient [11].

The next step in organic solar cell development was the introduction of bilayer systems in 1986. In these devices the main part of the incoming light is absorbed by the donor layer. Afterwards, the generated excitons have to diffuse to the interface with the strongly electronegative acceptor layer, where they can be dissociated. This new layout lead to power conversion efficiencies of about 1% [12]. The major drawback was still the short exciton diffusion length of about 10 nm. To absorb almost all of the incoming light, a donor layer with a thickness of circa 100 nm is needed. Hence, only 10% of the generated excitons can reach the interface and contribute to the generation of free charge carriers.

In 1992, Sariçiftçi et al. discovered the photoinduced electron transfer in composites of conjugated polymers and fullerenes [13], which resulted in the development of the bulk heterojunction concept. Instead of a donor and an acceptor layer, only one layer consisting of a blend of both materials was applied between the electrodes [14]. In this way the interface area can be

increased considerably and nearly all generated excitons can reach a donor–acceptor interface. For these devices, the morphology of the active layer plays an important role, since good percolation paths are needed. Otherwise the separated charge carriers are not able to reach the contacts and are lost due to recombination. The three major approaches to control morphology are by the choice of the organic solvent [15], by using additives [16] or by thermal treatment of the active layer [17]. The BHJ concept and the development of new acceptor materials lead to rapidly increasing power conversion efficiencies up to 10% [5], which means that organic solar cells are at the brink of market introduction.

Besides device efficiency, another important aspect for a successful introduction to the market is the stability of organic solar cells. During the last decades a lot of research in this field was done, too, and the device stability improved considerably from only a few minutes up to several thousand hours nowadays. These developments were reviewed by Jørgensen et al. [18, 19] in detail.

The recent steps in organic solar cell development mentioned here give only a very brief overview of the last decades. More detailed summaries can be found in the reviews by Deibel et al. [20] and Brabec et al. [8].

## 2.2 Organic Semiconductors

In this section, I will briefly explain the origin of the semiconducting character of conjugated polymers and how charge transport in these kinds of materials can be understood.

### Origin of the semiconducting character

In organic semiconductors two major classes can be distinguished: Conjugated small molecules that need to be evaporated and result in well ordered films and conjugated polymers that are solution processable and result in less ordered films. In this thesis we will focus on the more common conjugated polymers, since no vacuum evaporation steps are necessary and fast roll-to-roll mass printing techniques are feasible as will be shown later in chapter 10.

A conjugated polymer is defined by its alternating single and double bonds of its carbon atoms as shown in Figure 2.1, which is crucial for its semiconducting properties. The ground state of a carbon atom is the  $1s^2 2s^2 2p^2$  configuration with four valence electrons. If multiple carbon atoms are bound, one  $2s$  and two of the  $p$  orbitals ( $p_x$  and  $p_y$ ) form three equivalent  $sp^2$  hybrid orbitals. They arrange in a plane and are separated by angles of  $120^\circ$ , each. The

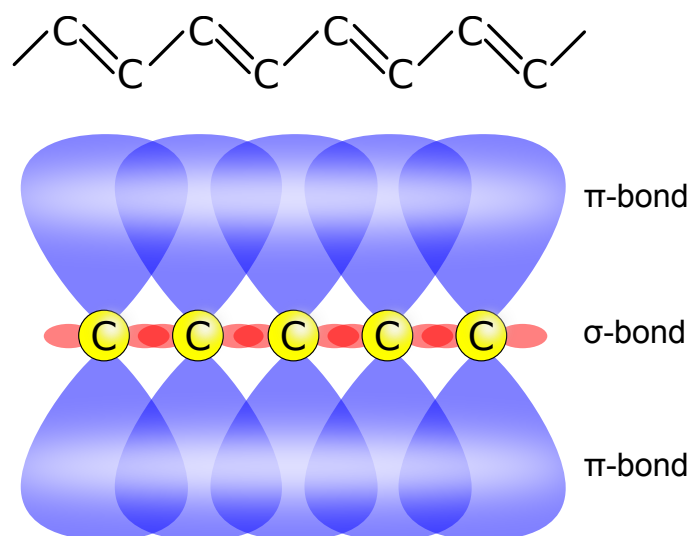


Figure 2.1: A conjugated polymer is based on a chain of carbon atoms with alternating single and double bonds (upper figure). The conjugation leads to the formation of  $sp^2$  orbitals that arrange in a plane and form  $\sigma$  bonds. Perpendicular to this plane the overlapping  $\pi$  bonds result in delocalized electron wave functions above and below this plane which are responsible for the conductivity of the polymer.

fourth  $p_z$  orbital aligns perpendicular to this plane. In conjugated polymers, overlapping  $sp^2$  hybrid orbitals form covalent  $\sigma$  bonds that result in strongly localized electrons, that do not contribute to charge transport in the organic semiconductor. In contrast, the overlapping  $p_z$  orbitals form  $\pi$  bonds above and below the hybrid orbital plane, on which the electrons are delocalized over all carbon atoms that are involved (see Figure 2.1). These delocalized  $\pi$  electrons can move quasi-free on the molecule and therefore contribute to the conductivity.

Another consequence of the interaction of several carbon atoms is the splitting of the  $p_z$  orbitals into multiple binding and antibinding orbitals. If the number of interacting carbon atoms is high enough, energy bands are formed that are denoted as highest molecular orbital (HOMO) and lowest unoccupied molecular orbital (LUMO), as shown in Figure 2.2. In comparison to inorganic semiconductors, HOMO and LUMO correspond to valence and conduction band. The separation of these two bands by a bandgap of about one to three electron volts is partially due to Peierls instability, which is a result of the alternating single and double bonds of the carbon atoms and hence the alternating inter-atomic distances. The bandgap is crucial for the semiconducting character of conjugated polymers and enables the absorption



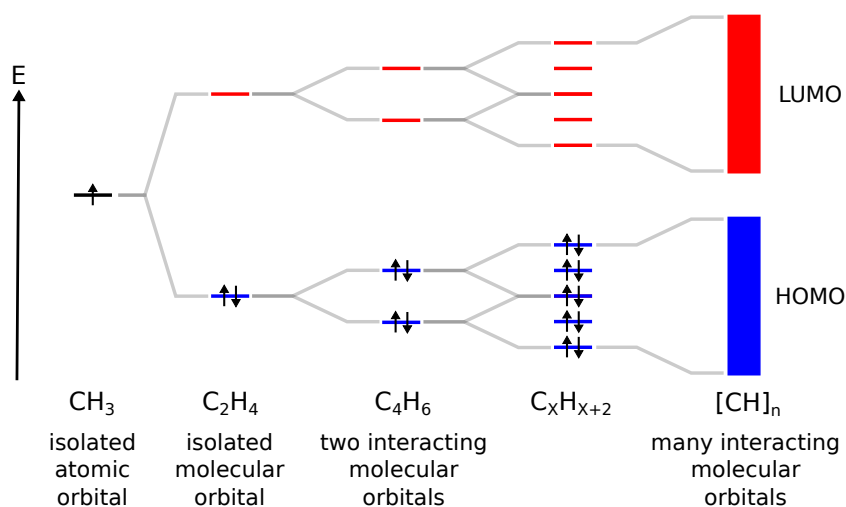


Figure 2.2: Splitting of the  $p_z$  orbitals into binding and antibinding orbitals. The splitting increases with increasing number of contributing carbon atoms until  $\pi$  bands are formed, which are denoted as HOMO and LUMO. Due to Peierls instability, they are separated by a bandgap of one to three eV.

of visible light. Therefore conjugated polymers are an interesting material class for organic solar cells.

The conjugation length of a polymer describes the number of monomer units, on which the delocalized  $\pi$  electrons can move and contribute to the charge transport. This effect is due to structural defects in the polymer chain, which disrupt the conjugation. Since the conjugation lengths of different molecules are randomly distributed, the HOMO and LUMO levels of these different molecules are energetically distributed, too. This energetic distribution of localized HOMO and LUMO states will be further denoted as energetic disorder.

## Charge Transport

Organic semiconductors are disordered systems and thus the corresponding charge transport mechanisms clearly differ from those in highly ordered inorganic semiconductors. In the latter case, the number of atoms contributing to the energy level splitting is much larger and therefore continuous bands are formed. The electron wave functions are delocalized over the entire crystal and hence the electrons can move quasi-free in the conduction band of the crystal. In contrast, the electrons in disordered organic semiconductors are only delocalized over single molecules. The HOMO and LUMO energy levels are distributed due to the energetic and spatial disorder of individual molecules. As mentioned before the energetic disorder is due to the distribution of conju-

gation lengths for different molecules and an additional spatial disorder. The latter is caused by the spatial arrangement of the molecules and, therefore, the overlap of their  $\pi$  orbitals. So, basically two kinds of charge transport in conjugated polymers can be distinguished:

**intra-chain** Very efficient charge transport along the polymer chain due to delocalization of the electron.

**inter-chain** Charge transport between different molecules and thus energetically and spatially localized states by hopping [21, 22].

In disordered systems such as organic semiconductors, the limiting factor for charge transport is the inter-chain hopping of the charge carriers. During the past years, several models were developed, in order to describe this hopping transport and I will briefly introduce the most important ones. In principle, there are two widely-used hopping-rate models, which focus on the description of single hops from one localized molecular orbital to a neighboring one. Both define hopping rates, which in general consist of two major contributions. The first one is a tunneling term to overcome the spatial distance between the neighboring states, and the second one is a Boltzmann term to account for the energetical difference of the states. In 1956, Marcus presented his theory [21, 23], which is valid for disordered materials with a strong electron-phonon coupling. Afterwards, Miller and Abrahams [22] proposed in 1960 a similar model for disordered materials with weak polaron effects. Hence, in the latter model the Boltzmann term is only significant for hops to energetically higher states and set unity otherwise.

A macroscopic way to describe charge transport mechanisms is the multiple trapping and release (MTR) model. It was introduced by Schmidlin et al. [24] and Noolandi et al. [25] in 1977 for amorphous inorganic semiconductors. They assumed a band edge, below which charge carriers are considered to be trapped in localized states and need to be thermally activated before they can further contribute to the hopping transport. In 1985 Monroe [26] proposed a transport energy ( $E_{trans}$ ) for an exponential density of states, which is similar to the band edge and relevant for hopping transport within the band tail of amorphous semiconductors at low temperatures. Therefore, charge carriers need to be activated to the transport energy, and not the band edge for charge transport. Baranovskii et al. showed in 1997, that this concept is also valid for Gaussian densities of states (GDOS) [27]. Hence, the MTR model is also applicable for organic disordered systems, which can be described by a GDOS [28]. The principle of the MTR model is depicted in Figure 2.3 (top).

Another prominent model to describe charge transport in organic disordered systems is the Gaussian disorder model (GDM) [28] (see Figure 2.3,

bottom). Based on absorption measurements, Bäessler et al. assumed a Gaussian density of states (GDOS) for the energetic and spatial disorder of the localized states, respectively. Nevertheless, both distributions are supposed not to be correlated in the GDM. The electron–phonon coupling is considered here to be very weak and can therefore be neglected. Hence, the hopping rates between neighboring states are given by the model of Miller and Abrahams [22]. During hopping transport, the charge carriers tend to thermalize to a quasi-equilibrium state and need to be thermally excited above the transport energy in order to further contribute to the charge transport. A more detailed discussion of charge transport in organic disordered systems can be found in the reviews of Bäessler from 1993 [28] and 2012 [29].

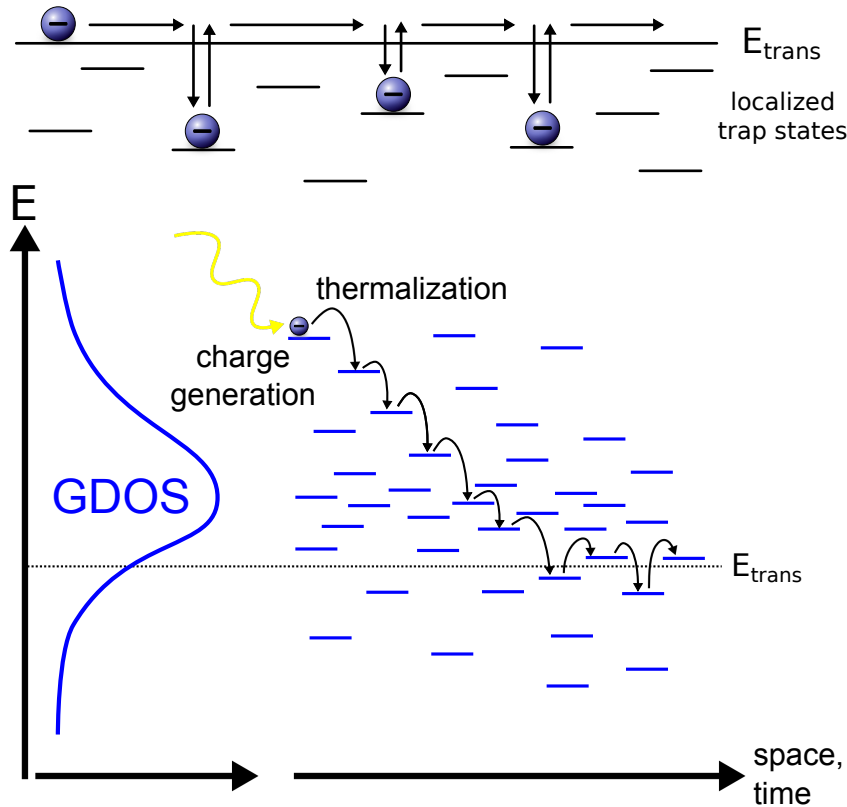


Figure 2.3: Top: MTR model: Mobile charge carriers can be trapped in localized states during inter-chain hopping transport and need to be thermally activated above the transport energy ( $E_{trans}$ ) before they can further contribute to the transport. Bottom: GDM model: Gaussian density of states for spatial and energetical disordered system. Charge carriers tend to thermalize during hopping transport to a quasi-equilibrium state. Above  $E_{trans}$  the charge carriers can move as if they were quasi-free (after [20]).

## 2.3 Working Principles of Organic BHJ Solar Cells

I will first give a very short overview of the basic steps of photocurrent generation in organic solar cells, as it will be discussed in more detail in chapter 3. In the next part, basic solar cell parameters as open circuit voltage ( $V_{OC}$ ), short circuit current ( $I_{SC}$ ) etc. will be introduced, which are relevant for all kinds of solar cells.

### Photocurrent generation

The typical layout of an organic BHJ solar cell is shown in Figure 2.4 (a). The anode consists of a glass substrate which is covered by a transparent conducting oxide (TCO) such as indium tin oxide (ITO), which was used in this thesis. On top a hole transport layer of PEDOT:PSS is followed by the photoactive blend of a conjugated polymer and a fullerene. The final layer is the metallic electrode, that acts as cathode.

The generation of photocurrent in these organic BHJ solar cells can be briefly explained as follows and is shown in Figure 2.4 (b). All processes mentioned here will be discussed in more detail in chapter 3. Basically, the incident light is absorbed by the conjugated polymer of the photoactive blend and generates a strongly bound exciton (Figure 2.4 (b) I), as it was found by Frenkel in 1931 for mono- and diatomic crystals [30, 31]. In order to be able to generate a photocurrent this exciton needs to diffuse to a donor–acceptor interface within its diffusion length of about 10 nm. At the interface an ultrafast charge transfer of the electron from the conjugated polymer to the fullerene acceptor occurs within femtoseconds [13], making this process extremely efficient (Figure 2.4 (b) II). Thereafter, electron and hole can still be coulombically bound, despite being located on different molecules. Nevertheless, the binding energy of this polaron pair is weakened due to their spatial separation, which is also enhanced by the delocalization of the charge carriers on their particular molecules. Hence, the internal electric field is now able to separate the weakly bound polaron pair and both charge carriers can be transported to their respective electrode, where they are extracted (Figure 2.4 (b) III and IV). In organic semiconductors these free charge carriers are called polarons, since they polarize their surrounding while moving through the organic material. This moving “polarization cloud” around the free charge carriers is typical for organic semiconductors and is due to their low dielectric constant. One has to keep in mind, that the photocurrent generation as explained above accounts for the ideal case, when every incident photon is converted into current. In a realistic device loss mechanisms such as geminate recombination of

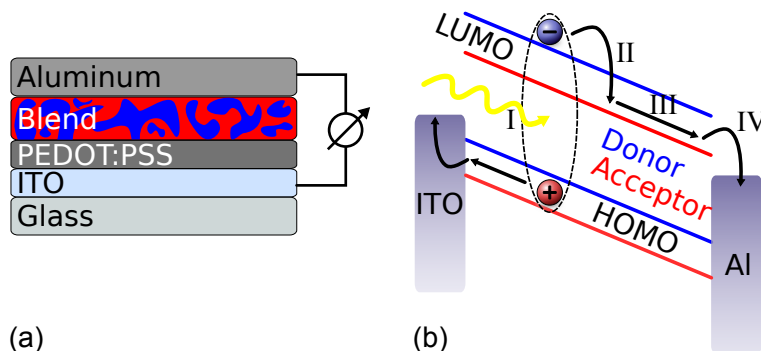


Figure 2.4: (a) Device layout of a standard organic BHJ solar cell, which is illuminated via the transparent anode (glass/ITO) (b) Respective band diagram: The incoming light is absorbed by the donor and a strongly bound exciton is generated. The electron is transferred to the acceptor LUMO, which enables the exciton to be separated by the internal electric field. Finally both charges are transported to their respective electrode.

the polaron pair (electron and hole from same precursor state) or nongeminate recombination during charge transport (different precursor states) can occur. These will be addressed in more detail in chapter 4.

## Solar cell characteristics

All different kinds of solar cells are based on the photoelectric effect, where light is converted into electric energy. This effect was already discovered by Hertz in 1887 [32] and explained by Einstein with the absorption of quanta of light, i.e. photons, in 1905 [33].

In principle, every solar cell can be described by its current–voltage (IV) curve which corresponds to the characteristic of a diode. Under illumination the whole curve is shifted to more negative currents and several characteristic points in the IV curve arise as shown in Figure 2.5. These typical points describe special configurations of the energy bands and determine the performance of the solar cell. Under reverse bias (Figure 2.5 a) the generated free electrons move on the LUMO of the acceptor (blue) towards the aluminum cathode, where they are extracted. Vice versa, the holes move on the HOMO of the donor (red) and are extracted at the ITO anode. In this case, the internal electric field is high enough to extract all generated charges and the injection barriers for holes at the cathode and electrons at the anode are high enough to prevent charge injection. Hence the resulting current in reverse bias is constant. If no external bias is applied (Figure 2.5 b), short circuit conditions are obtained and the internal electric field is only due to the difference

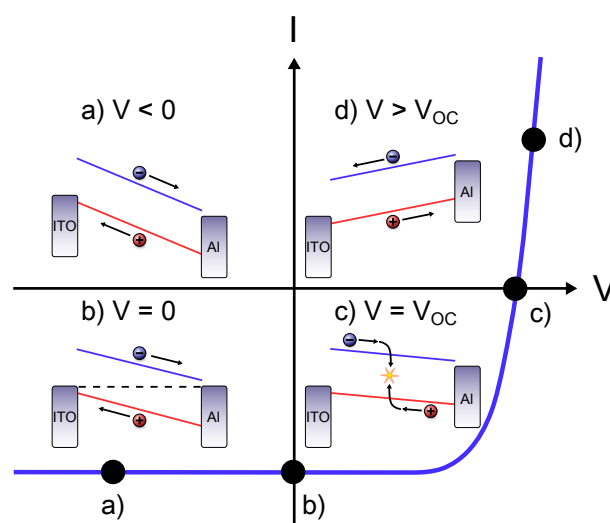


Figure 2.5: Current–voltage characteristics of a solar cell: a) Reverse bias: All generated charge carriers are extracted. b) Short circuit conditions: Internal electric field only due to difference of electrode work functions. c) Open circuit conditions: Charge carrier generation is compensated by recombination. d) High forward bias: Inverted current flow and charge injection at the electrodes.

of the work functions of the electrodes. The corresponding current flowing is denoted as short circuit current  $I_{SC}$ . The third important point is the case when open circuit conditions are reached (Figure 2.5 c). At  $V_{OC}$  the charge carrier generation is compensated by recombination processes and therefore no net current is flowing. The theoretical maximum value of  $V_{OC}$  is given by the effective band gap, i.e. the difference of the acceptor LUMO and the donor HOMO. As Rauh et al. pointed out, this theoretical maximum value cannot be reached in real devices due to recombination losses and injection barriers at the contacts. Especially at low temperatures, the injection barriers dominate the behavior of the device and  $V_{OC}$  converges to the built-in potential ( $V_{Bi}$ ) [34], the difference of the electrode work functions. Hence, the energy bands under open circuit conditions are not flat yet. Furthermore, in chapter 6 will be shown that the built-in potential in organic solar cells does not really correspond to the case of flat energy bands. Due to band-bending at the contacts, we introduce a case of quasi flat energy band (QFB), which is more appropriate for a zero field situation inside the device. By further increasing the applied voltage, exceeding  $V_{OC}$ , the energy bands are tilted in the opposite direction (Figure 2.5 d). Now, electrons are moving towards the ITO and holes to the aluminum contact and the injection barriers for both kinds of charge carriers are considerably lowered. Hence, charges are injected at the electrodes, resulting in a strongly increasing current with increasing

voltage.

However,  $V_{OC}$  and  $I_{SC}$  on their own are not sufficient to reliably characterize a solar cell. Another important factor is the maximum power point (MPP) where a solar cell will preferably be operated. It is defined to be at the maximum of the current–voltage product, as shown in picture 2.6. The fill factor (FF) is defined as shown in Equation 2.1 and describes the quality of a device, i.e., how “rectangular” is the IV curve in the 4<sup>th</sup> quadrant.

$$FF = \frac{I_{MPP} \cdot V_{MPP}}{I_{SC} \cdot V_{OC}} \quad (2.1)$$

So, in an ideal solar cell with a fill factor of 100%, the maximum power point would be theoretically defined by  $I_{SC}$  and  $V_{OC}$ . The most important parameter of a solar cell is its power conversion efficiency  $\eta$  as shown in Equation 2.2, which is the ratio of the power generated by the device at the MPP and the power of the incident radiation  $P_L$ .

$$\eta = \frac{I_{SC} \cdot V_{OC} \cdot FF}{P_L} \quad (2.2)$$

In order to enable a worldwide comparability of power conversion efficiencies for different kinds of solar cells, standard testing conditions (STC) need to be defined. In general this means, that the illumination level is set to 100 mW/cm<sup>2</sup> under an AM1.5G sun spectrum and an active layer temperature of 25°C. For organic solar cells, Shrotriya et al. [35] gave a detailed description for accurate and reliable power conversion efficiency measurements.

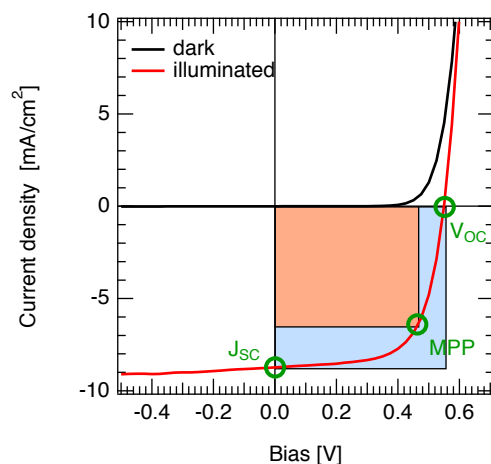


Figure 2.6: Current–voltage characteristics of a P3HT:PC<sub>61</sub>BM (1:1 blend ratio) BHJ solar cell. The ratio of the red and the blue rectangle defines the fill factor of the device.

# Photocurrent Generation

---

The photocurrent density  $J_{Ph}$  in solar cells is defined as the difference between light  $J_{Light}$  and dark  $J_{Dark}$  current density (see Equation 3.1). In classical silicon solar cells the photocurrent is voltage-independent, as  $J_{Light}$  and  $J_{Dark}$  only differ by a constant offset, which is the short circuit current density under illumination. In contrast, for inorganic thin film technologies generally, as well as for organic solar cells, the photocurrent depends on the bias voltage which results in a reduction of the FF and hence solar cell efficiency [36].

$$J_{Ph}(V) = J_{Light}(V) - J_{Dark}(V) \quad (3.1)$$

In this chapter the crucial steps for photocurrent generation in organic BHJ solar cells will be discussed in more detail. The first part will address photon absorption and polaron pair generation. Thereafter, I will discuss polaron pair dissociation which can be described by a field dependent model of Braun and Onsager. Charge extraction will be subsequently discussed in terms of a model by Sokel and Hughes. Finally, a combined model of Braun–Onsager and Sokel-Hughes theory will be shown, which is able to explain the voltage dependence of the photocurrent in organic BHJ solar cells.

## 3.1 Polaron Pair Generation

The first step in polaron pair generation in organic BHJ solar cells is the absorption of a photon by the conjugated polymer. Due to the low dielectric constant of about 3 to 4 in organic materials [37, 38], the generated exciton is a so called strongly bound Frenkel–exciton [30, 31] with a typical coulombic binding energy of about 0.5 eV [37, 39]. In this case, the internal electric field is not high enough to separate the charges efficiently and therefore an intermediate step via a less strong bound polaron pair is needed. To do so, the exciton has to diffuse to a donor–acceptor interface. The most problematic issue in this process is the short exciton diffusion length of about 4 - 9 nm in case of the conjugated polymer P3HT [40, 41], which is the reason for the clearly better performance of the bulk heterojunction concept in contrast to bilayer devices. When the exciton reaches an interface, the electron is transferred from the donor to the acceptor due to the strong electronegativity of the



latter. This charge transfer has been shown to be ultrafast in the femtosecond region [13, 42]. In comparison to these timescales, competing loss mechanisms are much slower making the electron transfer from the donor to the acceptor highly efficient. At the resulting charge transfer state (CTS) the Coulomb binding energy of the polaron pair is reduced, due to the spatial separation of electron and hole, being located on different molecules. The delocalization of the charge carriers on their respective molecules further lowers the Coulomb binding energy of the polaron pair, making total charge separation by the internal electric field possible.

Concerning the processes discussed in this section, for a maximum charge transfer yield and hence polaron pair generation, a perfect blend would be preferable, enabling every generated exciton to reach a donor–acceptor interface within its diffusion length. Nevertheless, a higher phase separation is desirable for good polaron pair dissociation and charge transport. So, there is always an interplay between these two opposing prerequisites to obtain maximum device efficiency.

## 3.2 Polaron Pair Dissociation

As mentioned before, the polaron pair, consisting of an electron on the acceptor and a hole on the donor, is still coulombically bound and needs to be dissociated, before both charges can be transported to their respective electrode and contribute to the photogenerated current. A general approach to describe polaron pair dissociation at a given electric field  $F$  is based on a model that was presented by Onsager in 1938. In this field dependent model the recombination and dissociation probabilities of two oppositely charged ions with a certain spatial separation were derived from Brownian motion [43]. Braun extended this model in 1984 to the dissociation of charge transfer states with finite lifetimes [44], which is applicable for polaron pairs, too. In his model, Braun derived the polaron pair dissociation probability  $P_{Braun}(F)$  by taking three major processes the polaron pair can undergo into account. As shown in Figure 3.1, it can either decay to the ground state with a rate  $k_f$  or dissociate into free polarons with a field dependent rate  $k_d(F)$ . In addition the free polarons can undergo nongeminate recombination, resulting in a coulombically bound polaron pair again, with a rate  $k_r$ . The influence of geminate recombination of the polaron pair will be discussed in section 4.1. Based on the three rates mentioned above, the polaron pair dissociation probability at a defined electric field can be expressed as shown in Equation 3.2, where  $\tau_f(F) = (k_d(F) + k_f)^{-1}$  is the finite lifetime of the polaron pair. The decay

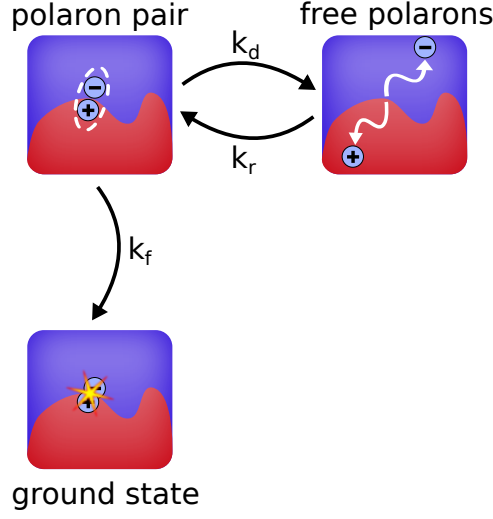


Figure 3.1: Brauñ–Oñsager model for field dependent polaron pair dissociation with PP dissociation rate  $k_d(F)$ , nongeminate recombination rate  $k_r(F)$  and decay rate to the ground state  $k_f$ .

rate to the ground state  $k_f$  is assumed to be independent of the electric field.

$$P_{Braun}(F) = \frac{k_d(F)}{k_d(F) + k_f} = k_d(F)\tau_f(F) \quad (3.2)$$

Both rates,  $k_d(F)$  and  $k_r$ , are linked via detailed balance, which means equilibrium conditions. The corresponding prefactor in Equation 3.3 was estimated by Fuoss et al. for ion pairs [45].

$$\frac{k_d(F=0)}{k_r} = \underbrace{\frac{3}{4\pi r_{PP}^3}}_{\text{Fuoss}} \underbrace{\exp\left(-\frac{E_B}{k_B T}\right)}_{\text{detailed balance}} \quad (3.3)$$

$E_B$  is the coulombic binding energy of a polaron pair with a spatial separation of the polarons  $r_{PP}$ .  $E_B$  needs to be overcome in order to dissociate the polaron pair into free polarons and is given by Equation 3.4, where  $e$  is the elementary charge and  $\varepsilon_r \varepsilon_0$  the effective dielectric constant of the blend:

$$E_B = \frac{e^2}{4\pi \varepsilon_r \varepsilon_0 r_{PP}} \quad (3.4)$$

The nongeminate recombination rate  $k_r$  can be described by Langevin theory [46], where  $\gamma$  is the Langevin recombination prefactor,  $\langle \varepsilon \rangle$  the spatially averaged dielectric constant and  $\langle \mu \rangle$  the spatially averaged sum of electron and hole charge carrier mobility.

$$k_r = \gamma = \frac{\langle \mu \rangle e}{\langle \varepsilon_r \rangle \varepsilon_0} \quad (3.5)$$

To include the field dependence of  $k_d(F)$ , Braun used the model of Onsager, where the field dependent PP dissociation rate is related to the field independent one. This is shown in Equation 3.6

$$\frac{k_d(F)}{k_d(0)} = \frac{J_1(2\sqrt{-2b})}{\sqrt{-2b}} \quad (3.6)$$

where  $J_1$  is the first order Bessel function and  $b$  the reduced field as defined in Equation 3.7.  $k_B$  is the Boltzmann constant and  $T$  the temperature.

$$b = \frac{e^3 F}{8 \pi \epsilon_r \epsilon_0 k_B^2 T^2} \quad (3.7)$$

Overall, this results in the polaron pair dissociation probability shown in Equation 3.8.

$$P_{Braun}(r_{PP}, F) = \frac{J_1(2\sqrt{-2b})}{\sqrt{-2b}} \frac{\mu e}{\epsilon_r \epsilon_0} \frac{3}{4\pi r_{PP}^3} \exp\left(-\frac{\Delta W}{k_B T}\right) \tau_f(F) \quad (3.8)$$

Deibel et al. pointed out that  $\mu$  and  $\tau_f$  are linearly dependent and thus can be used as a single parameter [47].

### 3.3 Charge Extraction

After free polarons are generated via the intermediate step of a coulombically bound polaron pair, they drift to their respective electrode. If there are continuous pathways to the electrodes and if the polarons are not lost due to nongeminate recombination processes, they can be extracted.

To do so we apply a model by Sokel and Hughes who investigated transient photoconductivity in insulators [48]. Besides their general, numerical solution they also present a special case which is solved analytically and is appropriate to describe the extraction of photogenerated charge carriers in organic solar cells. This special case is based on the following assumptions:

- The device corresponds to an extremely thin parallel plate capacitor in comparison to its lateral expansion: True for our devices with active layer thicknesses of about 100 nm and active areas of several mm<sup>2</sup>.
- The dielectric medium between the capacitor plates is only conductive under illumination: Reasonable assumption, since we investigate photocurrent and therefore only photogenerated charge carriers.
- Electrons and holes are generated uniformly in the dielectric medium: True for the bulk of our devices. Due to band bending at the contacts, this assumption is not valid there and they need to be considered separately.

- No trapping and recombination of charge carriers: Appropriate, since classical Langevin recombination is strongly reduced in this case [49].

In their model, Sokel and Hughes describe the charge transport with the continuity equation for electrons and holes, as shown in Equation 3.9.

$$\frac{\partial n}{\partial t} = \frac{1}{e} \frac{\partial J_n}{\partial x} + G \qquad \frac{\partial p}{\partial t} = -\frac{1}{e} \frac{\partial J_p}{\partial x} + G \quad (3.9)$$

$G$  denotes the charge carrier generation rate,  $e$  the elementary charge,  $n$  and  $p$  the charge carrier densities of electrons and holes, respectively. Their corresponding current densities  $J_n$  and  $J_p$  are displayed in Equation 3.10, where  $F$  is the electric field,  $\mu_n$  and  $\mu_p$  are the mobilities and  $D_n$  and  $D_p$  the diffusion constants of electrons and holes.

$$J_n = en\mu_n F + enD_n \frac{\partial n}{\partial x} \qquad J_p = ep\mu_p F + epD_p \frac{\partial p}{\partial x} \quad (3.10)$$

The charge transport of electrons and holes is connected via Poisson equation (Equation 3.11), where  $\varepsilon$  is the dielectric constant.

$$\frac{\partial F}{\partial x} = \frac{e}{\varepsilon} (p - n) \quad (3.11)$$

Including the following boundary conditions, where  $L$  corresponds to the thickness of the dielectric medium,

- At time  $t = 0$  the material is not charged and no free charge carriers exist:  $n(x, 0) = p(x, 0) = 0$
- Infinite surface recombination velocity:  $n(0, t) = n(L, t) = p(0, t) = p(L, t) = 0$

this results in the photocurrent density  $J_{Ph}$  shown in Equation 3.12. So, the photocurrent can be split into two contributions. The first one is the factor  $eGL$ , corresponding to the maximum photocurrent which can be extracted. The second contribution in square brackets describes the probability for these polarons, to be extracted.

$$J_{Ph} = eGL \cdot \left[ \coth \left( \frac{eV}{2k_B T} \right) - \frac{2k_B T}{eV} \right] \quad (3.12)$$

### 3.4 Photocurrent Model

With a combination of both models presented in this chapter, it is possible to describe the field dependent photocurrent in organic BHJ solar cells. The resulting model is shown in Equation 3.13 and consists of three major contributions:

- The maximum photocurrent  $J_{Ph,max}$ , which mainly depends on the exciton generation rate  $G$ .
- The field and temperature dependent charge extraction term by Sokel and Hughes.
- The field and temperature dependent polaron pair (PP) dissociation probability by Braun and Onsager.

$$J_{Ph} = \underbrace{eGL}_{J_{Ph,max}} \cdot \underbrace{\left[ \coth\left(\frac{eV}{2k_B T}\right) - \frac{2k_B T}{eV} \right]}_{\text{charge extraction}} \cdot \underbrace{P_{Braun}(F)}_{\text{PP dissociation}} \quad (3.13)$$

In 2004 Mihailetchi et al. described the experimentally determined photocurrent of PPV:PC<sub>61</sub>BM solar cells by introducing an effective field to the model and assuming Gaussian distributed polaron pair radii (see section 3.2) [50]. The effective field was defined with respect to  $V_0$ , the voltage where the photocurrent equals zero. The major drawback of their approach was the definition of the effective voltage, which allows only for a description of the photocurrent in reverse direction. As I will show in chapter 6 a pulsed photocurrent measurement technique and an effective electric field, which is defined with respect to the point of optimal symmetry (POS) of the photocurrent, enable us to describe the experimental photocurrent in reverse and forward direction for different electrode materials [51].

# Recombination Dynamics

---

In the following chapter the recombination dynamics in organic disordered systems will be discussed in detail, as they provide important loss mechanisms for charge carriers in our devices. I will distinguish between two basic recombination processes. The first one is the geminate recombination of Coulomb bound charge transfer excitons at the donor–acceptor interface. Its influence on the free charge carrier generation will be discussed in section 4.1. In contrast, the second one is nongeminate recombination of already separated polarons during charge transport to their respective electrode. This will be addressed in section 4.2. Finally, the Langevin recombination model will be introduced in section 4.3. Despite being derived for two oppositely charged ions in a large reservoir [46], it has been adapted to describe bimolecular recombination processes in organic BHJ solar cells [52].

## 4.1 Geminate Recombination

As mentioned in the introduction of this chapter, geminate recombination denotes the recombination of two oppositely charged polarons at the donor–acceptor heterointerface, which are coulombically bound. Since both polarons originate from the same precursor state there is always the same number of positive and negative polarons to recombine and hence, geminate recombination is referred to as a first order or monomolecular recombination process. As indicated in Figure 4.1 (a), monomolecular recombination competes with polaron pair dissociation and is a loss mechanism during generation of free charge carriers. Hence, both processes directly influence the photocurrent generation.

The polaron pair is also called charge transfer state (CTS) and is generated via an ultrafast charge transfer [42] from the singlet exciton  $S_1$  as shown in Figure 4.1 (a). It is an intermediate state in the charge separation process and has a finite lifetime in the regime of 1–100 ns [53, 54] in polymer–fullerene blends. In order to generate free charge carriers, which means reaching the charge separated state (CSS), the Coulomb binding energy  $E_B$  of the polaron pair needs to be overcome.  $E_B$  can be estimated from the Coulomb potential (Equation 3.4) to the order of 0.4 to 0.5 eV for P3HT:PCBM by assuming

a dielectric constant  $\epsilon_r = 3.3$  and a spatial separation of the polarons  $r_{PP} = 1$  nm. In case of MDMO-PPV:PCBM,  $E_B$  can be accessed by photoluminescence measurements, which result in exciton binding energies up to 200 meV [55, 56]. In both cases  $E_B$  is clearly above the thermal energy of 25 meV, which is therefore not sufficient for efficient generation of free charge carriers and the geminate recombination rate depends on the height of  $E_B$ . By applying an external electric field, this electric barrier for polaron pair dissociation can be lowered and thus the influence of geminate recombination on photocurrent generation can be reduced. In contrast to this charge transfer state mediated photogeneration of free charge carriers, other scenarios might be possible, too. The charge carriers can be either separated directly or via an excited or “hot” CTS as presented in Figure 4.1 (b), which is also an ultrafast process ( $\sim 100$  fs) [57]. In both cases the influence of geminate recombination on the polaron pair dissociation yield is negligible and results in a high photogeneration yield as found by Howard et al. for P3HT:PCBM by means of transient absorption measurements [58]. Hence, the height of  $E_B$  is not relevant for an efficient free charge carrier generation and therefore almost no field dependence is expected in contrast to the scenario mentioned before.

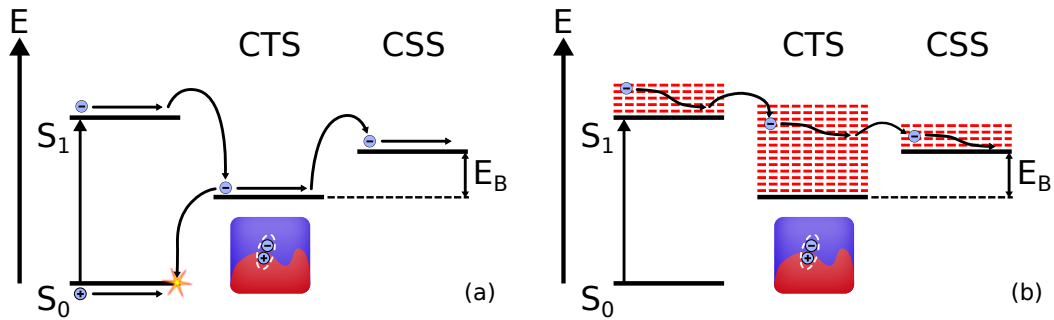


Figure 4.1: (a) Polaron pair dissociation via a CTS: Ultrafast charge transfer from singlet exciton  $S_1$  to the CTS.  $E_B$  needs to be overcome in order to reach the CSS, otherwise the polaron pair is lost due to geminate recombination. (b) Polaron pair dissociation via an excited (“hot”) CTS: Ultrafast charge separation in the 100 fs regime [57]. Due to the excitation of the CTS,  $E_B$  can be easily overcome and therefore the amount of geminate recombination is insignificant.

Field dependent polaron pair dissociation in organic BHJ solar cells will be investigated in this thesis by time-delayed collection field (TDCF) measurements. The method will be introduced in section 5.3.2 and the experimental findings will be discussed in chapters 7 and 8.

## 4.2 Nongeminate Recombination

In general, nongeminate or bimolecular recombination denotes the recombination of two polarons from different precursor states and takes place during charge transport to the electrodes. It occurs if two oppositely charged polarons approach below the Coulomb capture radius, i.e. the distance at which coulombic binding energy and thermal energy are equal. In contrast to geminate recombination being a first order process, nongeminate recombination cannot simply be considered as a second order process in general. In fact, different cases of bimolecular recombination can be distinguished, differing by the probability of a polaron to find an oppositely charged one to recombine. So, not the recombination itself, but the finding of the recombination partner is the limiting factor in this process. The basic understanding of bimolecular recombination is that two independent, mobile polarons meet during transport to their respective electrode, which is a second order process, as shown in Figure 4.2 (a). But it is also possible that a polaron is trapped and recombines with a mobile one. Here, the recombination order depends on the density of trapped charge carriers  $n_t$ . If the latter clearly exceeds the amount of free charge carriers,  $n_t$  is hardly diminished by recombination with mobile charge carriers. Therefore, the probability of finding a recombination partner for the mobile polaron is high and a first order bimolecular recombination is observed as shown in Figure 4.2 (b). Is in contrast the density of trapped charge carriers comparable or lower as the density of mobile polarons,  $n_t$  is reduced considerably by recombination and thus the process is of second order. Especially at low temperatures, recombination orders larger than two have also been observed [59, 60, 61]. These findings may be attributed to a charge carrier density dependent Langevin recombination prefactor, which is due to the influence of trapping of charges in the tail states of the Gaussian density of states [62, 59].

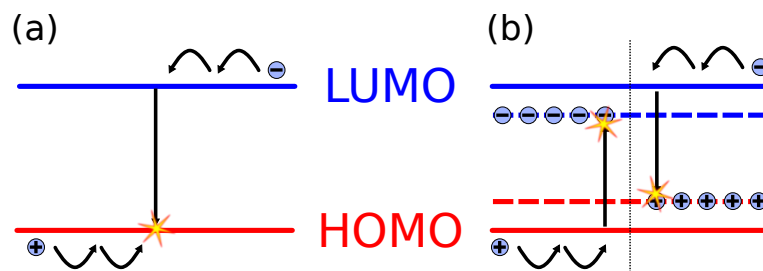


Figure 4.2: (a) Second order bimolecular recombination of two mobile charge carriers. (b) If the density of trapped charge carriers clearly exceeds the density of the mobile ones, the recombination process is a first order process. Otherwise the bimolecular recombination is of second order.



Finally, it is important to mention that nongeminate recombination can occur via an intermediate state, which is the polaron pair. Hence, there is the finite chance for this polaron pair of being dissociated again.

### 4.3 Langevin Theory

An established model to describe bimolecular recombination dynamics in organic BHJ solar cells is based on Langevin's theory, which he presented in 1903 [63]. A detailed description of its adaption to organic semiconductors can be found in the book of Pope and Swenberg [52], which will be summarized in this section.

In the Langevin model, two oppositely charged carriers recombine, if they approach each other below the Coulomb capture radius, as mentioned before. For simplification, the positive charge carrier is assumed immobile and the mobility of the negative one corresponds to the sum of both mobilities. Furthermore, it is assumed that the recombination rate is not limited by the recombination process itself, but by the probability of both charge carriers finding each other. These presuppositions are reasonable for organic disordered systems as the mobilities of both charge carriers are very low.

The Langevin recombination rate can be expressed as follows:

$$R_L = \gamma \cdot (np - n_i^2) , \quad (4.1)$$

where  $n$  and  $p$  are the respective charge carrier densities for electrons and holes and  $n_i$  the intrinsic charge carrier density.  $\gamma$  is the Langevin recombination prefactor

$$\gamma = \frac{e}{\varepsilon_r \varepsilon_0} (\mu_e + \mu_h) \quad (4.2)$$

where  $e$  is the elementary charge,  $\varepsilon_r \varepsilon_0$  the effective dielectric constant of the organic semiconductor, and  $\mu_e$  and  $\mu_h$  the electron and hole mobilities.

Nevertheless, in the case of organic BHJ systems, discrepancies to the classical Langevin theory can be expected. As mentioned above, Langevin theory was derived for two oppositely charged ions in a large reservoir, which is not entirely true in our case. In a BHJ system, electrons and holes are transported on different materials of the photoactive blend and hence the assumption of one reservoir is not sufficient. Depending on the material system, reduced Langevin recombination has been observed and the theoretically derived Langevin recombination rate  $R_L$  was extended by an additional reduction factor  $\zeta$  to match the experimental results [61]. A detailed discussion of possible origins and physical meaning of this reduction factor is non-trivial and cannot be given here in brief. For further reading, I recommend the

publications of Deibel et al. [61, 64]. The relation of Langevin theory to experimentally determined bimolecular recombination for different material systems will be discussed in the experimental part of this thesis.



# Experimental

---

Organic BHJ solar cells are prepared from solutions of polymer–fullerene blends in organic solvents such as chlorobenzene or chloroform. On a laboratory scale the most common techniques for deposition of the photoactive layer are spin coating and doctor blading. In both cases only small amounts of the active materials are required and the properties of the active layer can easily be controlled. For mass production on the other hand, these techniques are not feasible. A large scaling with a high device throughput and hence a cost-effective production are needed, which make roll-to-roll printing on flexible substrates a promising technique. BHJ solar cells which were printed on a paper substrate will be discussed in more detail in chapter 10. Otherwise, all samples mentioned in this thesis were prepared by spin coating as will be shown in this chapter.

The following sections will first briefly introduce the donor and acceptor materials we use for our devices. Afterwards, a general introduction to our sample preparation will be given. In the last section, the experimental setups for device investigation by TDCF, pulsed photocurrent and capacitance–voltage measurements will be explained in detail.

## 5.1 Organic Solar Cell Materials

### Donor Materials

The electron donating materials, or donors, used here were conjugated polymers. In principle, these are large macromolecules which consist of repeating monomer units. A very prominent example is P3HT, as shown below. If two alternating kinds of monomer units are used, the resulting macromolecules are denoted as copolymers. Extensive research in the field of material synthesis during the last decades resulted in increasing power conversion efficiencies due to better light absorption and charge transport properties of the polymers [20, 8].

### P3HT

As mentioned above, the most prominent polymer for organic BHJ solar cells is poly(3-hexylthiophene-2,5-diyl) (P3HT), which has extensively been studied [20, 8]. It consists of thiophene rings (denoted as head) with a hexyl side chain (tail), each, as shown in Figure 5.1. If these monomers are linked in alternating head-to-tail configuration, a highly crystalline polymer with a regioregularity of about 98% can be obtained. A high regioregularity allows for a better  $\pi - \pi$  - interchain stacking of the polymer chains and hence improves charge transport properties. P3HT absorbs light in the range of 400 to 600 nm. In this thesis we used P3HT (Sepiolid P200), purchased from BASF.

### MDMO-PPV

Another very well-known donor material is the polymer poly[2-methoxy-5-(3',7'-dimethyloctyloxy)-1,4-phenylenevinylene] (MDMO-PPV) as shown in Figure 5.1. It is based on poly(p-phenylenevinylene) (PPV) monomers which consist of a benzene ring with two additional carbon atoms for the coupling of the monomers. To improve solubility a 2-methoxy-5-(3',7'-dimethyloctyloxy) side chain is added. MDMO-PPV absorbs light in the range of 350 to 550 nm, which does not fit as well to the solar spectrum as P3HT. This is one reason for the lower solar cell performance of MDMO-PPV blends. The material we used was purchased from Sigma Aldrich.

### (Si-)PCPDTBT

A rather new low-bandgap material is the copolymer poly[2,6-(4,4-bis-(2-ethylhexyl)-4H-cyclopenta[2,1-b;3,4-b]-dithiophene)-alt-4,7-(2,1,3-benzothiadiazole)] (PCPDTBT), which is based on a cyclopentadithiophene unit (see Figure 5.1). In this case, the monomer consists of two thiophene rings that are bridged by a carbon atom. As a low-bandgap material, the incident light is absorbed in the range of 600 to 850 nm. To further improve solar cell performance, the thiophene rings can also be bridged by a silicon atom (Si-PCPDTBT: poly[(4,4-bis-(2-ethylhexyl)dithieno[3,2-b;2',3'-d]silole)-2,6-diyl-alt-(4,7-bis(2-thienyl)-2,1,3-benzothiadiazole)-5,5'-diyl]). Here, the materials were purchased from 1-material.

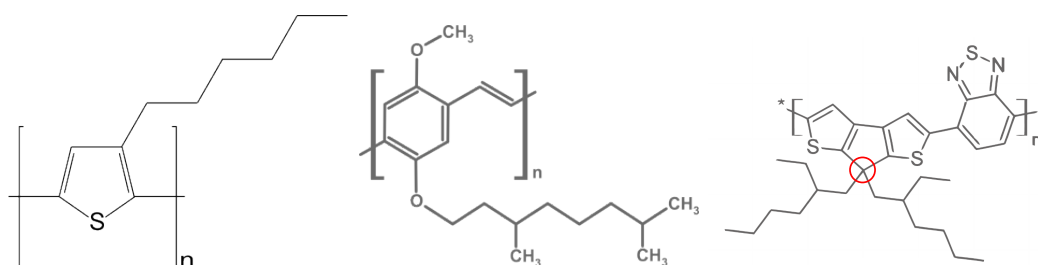


Figure 5.1: Left: P3HT monomer. Middle: MDMO-PPV monomer. Right: PCPDTBT monomer, for Si-PCPDTBT the carbon bridging atom for the thiophene rings (marked by red circle) is replaced by silicon.

## Acceptor Materials

Acceptors are strongly electronegative materials with a LUMO level which enables a fast and efficient electron transfer from the respective donor to the acceptor. Despite extensive research the best performing ones are still the fullerene derivatives used for the first solution processed organic BHJ solar cells in 1995 [14, 8].

### PCBM

The most well-known acceptor molecule is [6,6]-phenyl- $C_{60}$  butyric acid methyl ester ( $PC_{61}BM$ ), which is based on the buckminsterfullerene. The latter is a spherical fullerene molecule, which consists of a cage of 60 carbon atoms and looks like a football. Since the solubility of pure  $C_{60}$  in organic solvents is very poor [65], a side chain was added as shown in Figure 5.2. One drawback of  $PC_{61}BM$  is the bad absorption of the visible light. This can be improved by using an asymmetrical cage of 70 carbon atoms with significant visible light absorption [66, 67]. The corresponding molecule is denoted [6,6]-phenyl- $C_{71}$  butyric acid methyl ester ( $PC_{71}BM$ ) and enables a considerable hole transfer to the polymer, which results in a clear increase in photocurrent generation [68]. The major disadvantage of this better performing molecule is its higher price due to more purification steps which are necessary during material synthesis. Both materials were purchased from Solenne BV.

### PEDOT:PSS

In addition we use in our devices poly(3,4-ethylenedioxythiophene): polystyrolsulfonate (PEDOT:PSS) as a transparent hole conducting layer between the ITO anode and the photoactive layer. Its electron blocking properties improve solar cell characteristics by forming a selective electrode and there-

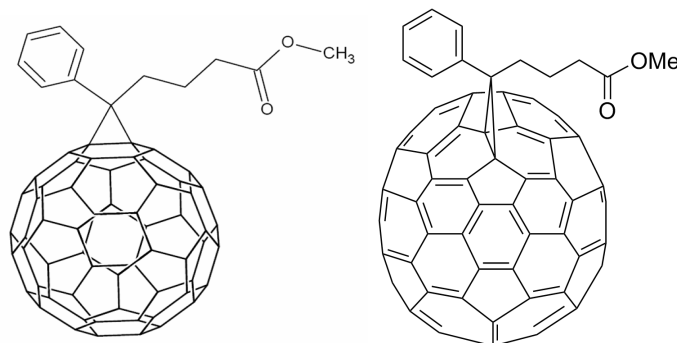


Figure 5.2: left: PC<sub>61</sub>BM consisting of a C<sub>60</sub> buckminsterfullerene and a side chain for better solubility. right: In PC<sub>71</sub>BM the fullerene cage consists of 70 carbon atoms.

fore reducing recombination at this electrode. Furthermore a thin layer of PEDOT:PSS on top of the ITO can further reduce the surface roughness and thus helps to avoid short circuits in the device. The batch of PEDOT:PSS we used (CLEVIOS P VP AI 4083) was purchased from H. C. Starck.

## 5.2 Sample Preparation

The standard layout of an organic BHJ solar cell in diode configuration is glass/ITO/PEDOT:PSS/blend/metal as shown in Figure 2.4 (a). Since the device is usually illuminated through the substrate, we typically use glass or a flexible, transparent plastic foil. The anode on top of the substrate consists of sputtered indium tin oxide (ITO) which was structured by a wet chemical lithography process. Before further treatment, all samples were cleaned by consecutive steps with soap water, deionized water, acetone and isopropanol for 10 minutes in an ultrasonic bath, each. Thereafter, a thin (approx. 40 nm), transparent layer of hole conducting PEDOT:PSS was spin cast on top of the structured anode to provide a selective contact. So far, all steps took place under ambient conditions. All subsequent processing was carried out in a two chamber glovebox system with a water and oxygen free nitrogen atmosphere. Right after inserting the PEDOT:PSS covered samples into the glovebox system, they were thermally treated on a hotplate for 10 minutes at 130 °C. In the following step, the photoactive layer was applied by spin casting a blend of donor and acceptor in an organic solvent onto the samples. Depending on the material system we chose chlorobenzene or ortho-dichlorobenzene, if not mentioned otherwise. For some of the blends another heating step on a hotplate was conducted. This second thermal treatment is called annealing and can alter the morphology as well, to provide a better charge transport and

improve solar cell characteristics [17, 69]. Another possibility to achieve similar effects is the use of additives such as octanedithiol [16]. Finally, the metal cathode consisting of 3 nm calcium and 100 nm aluminum was evaporated in a high vacuum chamber, that is attached to the glovebox system.

Basic device characterization, such as current–voltage, capacitance–voltage or photocurrent measurements took place directly after sample preparation in the second chamber of the glovebox system, so preventing any influence of oxygen and water on the devices. For temperature-dependent and TDCF measurements, the samples had to be transported to a cryostat and therefore were briefly exposed to ambient air.

In contrast to the standard device layout mentioned above, we also investigated mass printed organic BHJ solar cells on paper substrates. Due to the nontransparent paper substrate, the devices layout needs to be inverted and the samples were illuminated via the transparent top electrode. The preparation, investigation and simulation of these printed paper photovoltaics will be discussed in detail in chapter 10.

## 5.3 Experimental Setups and Techniques

In the following, the three major measurement methods applied in this thesis will be described in more detail. The first subsection concerns pulsed photocurrent measurements, which enabled us to compare the corrected, point symmetric and voltage-dependent photocurrent to a theoretical model by Braun–Onsager and Sokel–Hughes (see chapter 3). In the second subsection the experimental setup and working principles of time-delayed collection field measurements will be presented, which allow for the investigation of geminate and nongeminate recombination dynamics in organic BHJ solar cells. The third subsection is about capacitance–voltage measurements, Mott–Schottky analysis and the basic principles of impedance spectroscopy.

### 5.3.1 Pulsed Photocurrent

#### Why pulsed illumination

In order to investigate the process of charge generation in a solar cell, the current–voltage characteristics were measured under illumination. However, not all charges in the device were generated by the incoming light. Especially at forward bias, there is still a considerable influence of charge injection into the device. To cancel out this effect and obtain the current in the device solely due to photogenerated charges (i.e. the photocurrent), the dark current needs to be subtracted from the light current (see chapter 3). Nevertheless, this



correction is not sufficient to completely cancel out charge injection effects. Due to illumination, the solar cell temperature can increase by more than 10 K [70], which is an important effect especially for thin film technologies as organic photovoltaics. The higher temperature under illumination results in a higher injection current in comparison to dark conditions and in a higher charge carrier mobility [28], which are the reasons for an overestimation of the photocurrent, mainly in forward direction [70]. To correct for this effect, Ooi et al. proposed a pulsed measurement technique [71]. A detailed description of the latter, along with a discussion of its possibilities and limitations was given by Ooi in his PhD thesis [70].

### Experimental Setup

Our experimental realization of the pulsed photocurrent measurements is shown in Figure 5.3 and was controlled by a LabView routine. A basic part of this setup was the Data Acquisition card (DAQ-card) from National Instruments, that generated the voltage signals to pulse the illumination and swept the bias applied to the solar cell. In addition it was used to record the resulting photocurrent signal. For illumination we used a 10 W quad-chip "white" light emitting diode (LED), which can switch on / off fast enough for our purposes and is powerful enough to provide an illumination intensity comparable to one sun. The illumination intensity was controlled by the height of the rectangular pulse shape applied to the LED. By comparing the short circuit currents from illumination with LED and sun simulator, the illumination level was determined. This method is valid, as long as the photocurrent is linearly dependent on the light intensity [72], which was true for the illumination levels we applied in this thesis (about 0.01 to 6 suns).

### Signal

In order to measure the photocurrent, we applied a voltage step function to the device. The frequency of this step function was half of the frequency used to operate the illumination by the LED, and hence it was possible to measure dark and light current directly after another at each voltage step as shown in Figure 5.4 (left). If the illumination pulse is sufficiently short ( $\leq 1$  ms), the device will not heat up noticeably. Hence, dark and light current are recorded at approximately the same temperature and the overestimation of the photocurrent in forward direction is cancelled out (see Figure 5.4, right). Nevertheless, the pulse duration must not be too short, allowing dark and light current to reach steady-state conditions, before the illumination changes again (see Figure 5.4, left). To finally extract dark and light current vs. bias

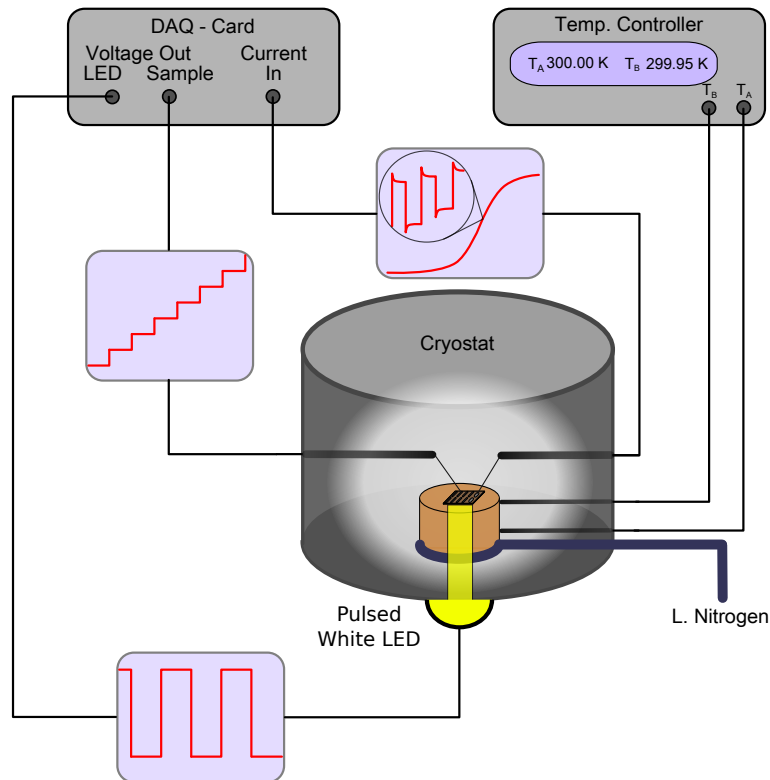


Figure 5.3: The setup for pulsed photocurrent measurements was operated by a LabView routine. The DAQ-card applied the corresponding voltage signals to LED (rectangular signal for pulsed illumination) and device (step function to sweep bias voltage). In addition, it recorded the resulting photocurrent at each bias voltage step in the dark and under illumination after reaching steady-state conditions.

voltage curves, the average value of the steady-state plateau was determined at each voltage step, resulting in one dark and one light current point for each bias voltage step. By subtracting dark and light current, the corrected photocurrent was calculated, showing a symmetric behavior when the influence of device heating was canceled out.

Without any influence of charge injection, the major relevant processes determining the corrected photocurrent are polaron pair dissociation, nongeminate recombination and charge extraction. Therefore it is possible to describe the corrected photocurrent by a combined model by the theories of Braun–Onsager and Sokel–Hughes as introduced in chapter 3. This will be shown in more detail in chapter 6.

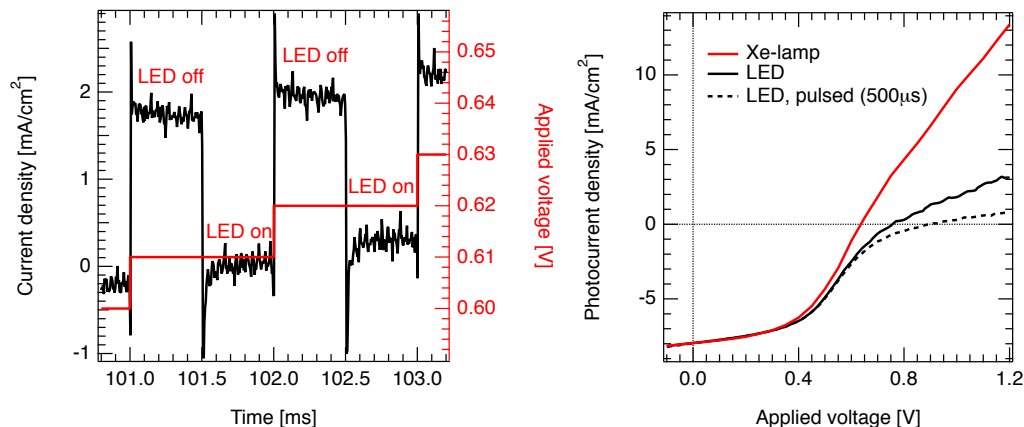


Figure 5.4: Left: Raw signal recorded by the DAQ-card: At each voltage step (red) the current density was measured in the dark and under illumination. Right: Photocurrent density in dependency of the illumination: Overestimation in forward direction due to device heating in case of Xe-lamp (red line) that was adjusted to simulate STC. A white light LED reduces (continuous illumination, solid black line) or even prevents (pulsed illumination, black dashed line) device heating and hence overestimation of the photocurrent density in forward direction.

### 5.3.2 Time-Delayed Collection Field

The time-delayed collection field (TDCF) technique was introduced by Mort et al. in 1980, when he investigated geminate and nongeminate recombination in amorphous silicon and chalcogenides [73, 74]. More than 20 years later, this method was transferred to a  $\pi$ -conjugated polymer by Hertel et al. [75], to analyze the field-dependent charge separation via an intermediate state, which means a not yet fully separated geminate electron-hole pair. Later on, recombination dynamics in organic BHJ solar cells were investigated for different material systems by Offermans et al. (MDMO-PPV:PCBM) [76] and Kniepert et al. (P3HT:PCBM) [77].

#### Experimental Setup

The experimental setup we used for TDCF measurements is shown in Figure 5.5. All samples were embedded into a helium closed-cycle cryostat, which enabled us to conduct temperature-dependent measurements. All of the technical equipment was controlled by a LabView routine, that also recorded the experimental data. For a better signal to noise ratio, every measurement was averaged 100 times by the digital oscilloscope.

In principle, TDCF is a pump–probe experiment with an optical pump and an electrical probe after a variable delay time  $t_{delay}$ , which is usually in the range of several hundred nanoseconds. To optically generate charges inside the sample, we used a pulsed neodymium-doped yttrium aluminum garnet Nd:YAG ( $\lambda = 532$  nm) laser. Its repetition rate was set as low as 5 Hz to prevent any disturbing influences on the experiment such as charging of the device. To vary the amount of charges generated in the device, the laser intensity, incident on the sample, was varied by three consecutive filter wheels with different neutral density filters. The laser intensity was detected right behind the filter wheels by a power meter. Hence, the resulting value is an upper limit for the laser intensity incident on the sample, since a fixed part of the intensity is lost during further transfer of the laser pulse between the filter wheels and the sample. Hence, we can only determine a relative change in illumination and not the absolute illumination intensity. However this is not important for our experiments, as we are only interested in the upper limit of the illumination, where no influence of nongeminate recombination in the device is observable (see “Working Conditions” later on in this section).

As probe signal, we applied a negative collection voltage  $V_{col}$  of -6 V to the sample (if not mentioned otherwise) to avoid recombination losses during charge extraction. The resulting photocurrent signal was measured by a digital oscilloscope, that recorded the voltage drop over a 50  $\Omega$  resistance in series with the sample. Probe signal as well as photocurrent signal were triggered via a photodiode, which detected scattered light from a beam splitter. The range of possible delay times in this setup was limited by two factors. The first one was the intrinsic delay of the function generator between the external trigger input channel and the signal output channel, which did not allow for  $t_{delay} < 385$  ns. This limitation could be circumvented by adding sufficient time to  $t_{delay}$  (e.g. slightly above 200 ms, depending on the laser repetition rate) to wait for the next laser pulse. The second limitation was due to the minimum repetition rate of the laser (5 Hz), which resulted in a maximum delay time slightly below 200 ms.

In order to investigate the field-dependence of charge photogeneration and recombination, a variable prebias  $V_{pre}$  was applied to the sample during  $t_{delay}$ .

## Signal

The voltage signal applied to the sample by the function generator is shown in Figure 5.6 on the left and the resulting measurement signal on the right. First,  $V_{pre}$  was applied to the sample, which defines the internal electric field

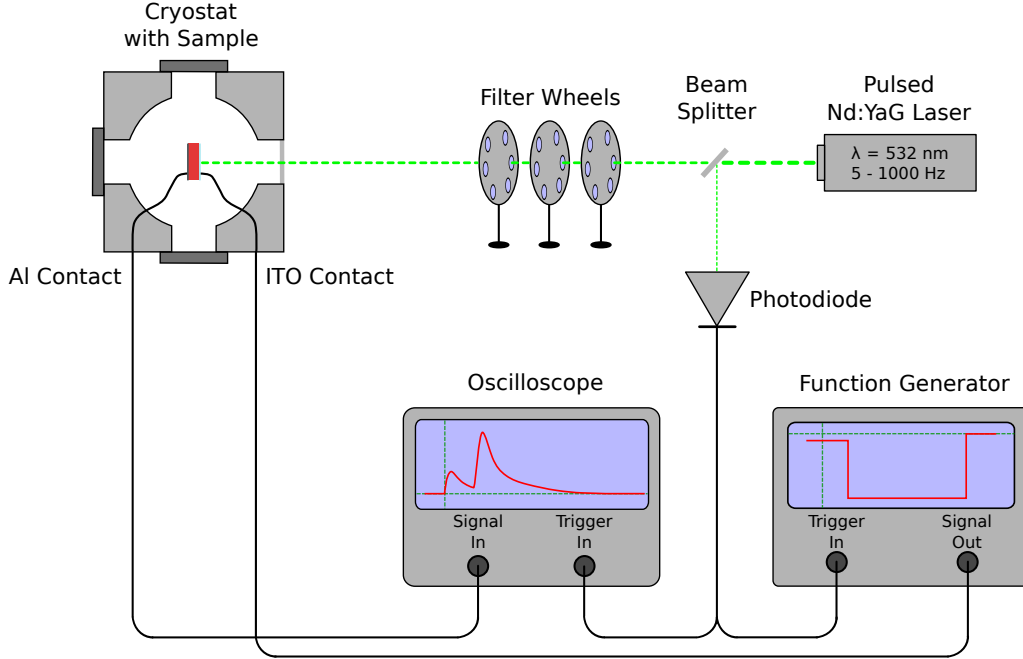


Figure 5.5: Setup for temperature-dependent TDCF measurements. Charges were generated by a pulsed Nd:YAG laser ( $\lambda = 532$  nm), while the beam intensity was varied by neutral density filters. Part of the laser pulse was redirected into a photodiode to trigger the function generator, which applied the voltage signal to the sample. The oscilloscope recorded the TDCF signal and was triggered by the photodiode, too.

$F_{int}$  as shown in Equation 5.1.

$$F_{int} \approx \frac{V_{Bi} - V_{pre}}{L} \quad (5.1)$$

Here,  $V_{Bi}$  is the built-in potential and  $L$  the thickness of the photoactive layer. Hence, if the externally applied  $V_{pre}$  is equal to the built-in potential, there is almost no internal electric field to support the polaron pair dissociation. In contrast, a highly negative  $V_{pre}$  results in an high electric field inside the sample, which can support the polaron pair dissociation.

While  $V_{pre}$  is applied, charge carriers are generated via a picosecond laser pulse and produce a photocurrent  $I_{Ph}$ , which is the sum over all charge displacements inside the sample. In case of our samples, the active layer was very thin ( $\sim 100$  nm), which means the incident photons were absorbed homogeneously throughout the whole active layer. Hence, the displacement currents are equal to the measured extraction currents of photogenerated charge carriers [77].

After the delay time  $t_{delay}$ , all remaining charges are extracted by a highly

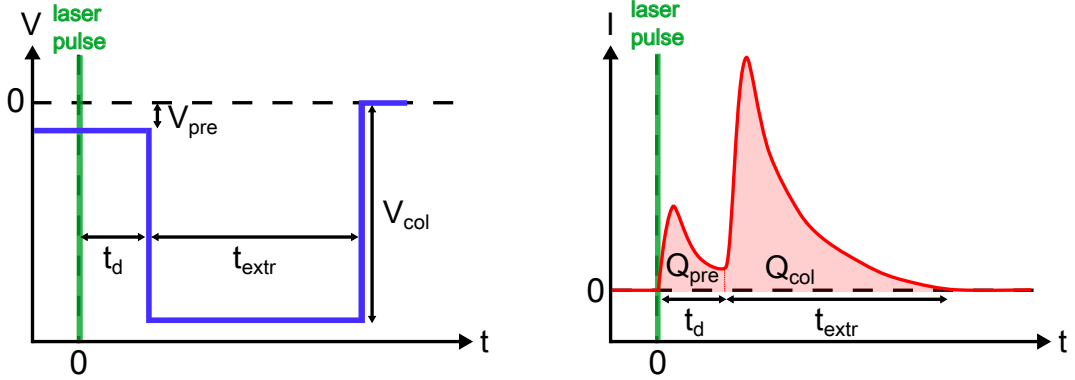


Figure 5.6: Left: Signal applied to sample via function generator. While the sample is kept at a variable prebias  $V_{pre}$ , charges are generated by a picosecond laser pulse. After delay time  $t_{delay}$ , a highly negative collection voltage  $V_{col}$  is applied to the sample for charge extraction. Right: Typical TDCF signal: First peak after laser excitation due to  $V_{pre}$  with corresponding integrated charge  $Q_{pre}$ . After  $t_{delay}$  all remaining charges are extracted by  $V_{col}$  during  $t_{extr}$  and the corresponding integrated charge is denoted as  $Q_{col}$ .

negative collection voltage  $V_{col}$ . The extraction time  $t_{extr}$ , during which  $V_{col}$  is applied, needs to be chosen sufficiently long (e.g.  $40 \mu s$  at room temperature, for lower temperatures even longer), to make sure that no photogenerated charges remain inside the sample. The amount of charge carriers extracted during delay time  $t_{delay}$ , corresponds to the area below the first peak of the TDCF signal in Figure 5.6 (right, denoted as  $Q_{pre}$ ) and is directly influenced by the applied prebias. In the same way, the second peak of the TDCF signal is due to  $V_{col}$  during the extraction time and its area is denoted as  $Q_{col}$ . Hence,  $Q_{pre}$  and  $Q_{col}$  are defined by the integrals over all charge displacements during the corresponding time interval as shown in Equation 5.2.

$$Q_{pre} = \int_0^{t_{delay}} I_{Ph}(t) dt, \quad Q_{col} = \int_0^{t_{delay} + t_{extr}} I_{Ph}(t) dt \quad (5.2)$$

Thus, the sum of  $Q_{pre}$  and  $Q_{col}$  equals the total amount of initially photogenerated charges minus those lost to recombination, and is denoted as  $Q_{tot}$ .

$$Q_{tot} = Q_{pre} + Q_{col} \quad (5.3)$$

### Working Conditions

In order to obtain reliable results, appropriate measurement conditions have to be chosen. In case of TDCF measurements there are two important fac-

tors. The first one is the collection voltage, which needs to be sufficiently high (in reverse direction) to make sure that all remaining charge carriers are extracted. Furthermore, a sufficiently high  $V_{col}$  is needed to avoid recombination losses during extraction time. On the other hand  $V_{col}$  needs to be above the reverse breakdown, since this would lead to strong charge injection effects and can destroy the device. The second important factor is the laser illumination intensity. Here, a high illumination level is desirable for a good signal to noise ratio. But if the illumination intensity is too high, not all photogenerated charges can be extracted by the collection field, since they are lost to nongeminate recombination processes during collection. For the latter, the amount of charges  $Q_{col}$ , extracted by the collection field, no longer increases linearly with increasing light intensity [77]. To verify that we meet these prerequisites, we performed illumination-dependent measurements for different prebias voltages in advance, as shown in Figure 5.7. The left graph shows the TDCF signal for different illumination intensities, while the right one depicts the resulting integrated charge  $Q_{col}$  of the collection peaks. Below pulse fluences of 30  $\mu\text{J}$ ,  $Q_{col}$  increases linearly with increasing illumination intensity, which corresponds to the desired working conditions. For higher pulse fluence, a sub-linear rise is observed, indicating nongeminate recombination losses during charge collection [77]. Hence, we chose for all TDCF experiments a pulse fluence about half an order of magnitude below the beginning influence of nongeminate recombination.

### Fit Routine

To investigate bimolecular recombination in organic BHJ solar cells, as will be discussed later on, we performed TDCF measurements with a constant prebias, but varying delay times. As prebias we chose a voltage close to the open circuit voltage to minimize the current flowing through the sample. In this case, there is almost no internal field inside the sample and only a few charges are extracted during the delay time. In order to obtain the Langevin recombination prefactor  $\gamma$ , we applied an iterative fit routine, which was introduced by Kniepert et al. [77]. This routine will be described here briefly.

Starting with open circuit conditions, we initially neglect all recombination processes, which means that  $Q_{tot}$  is constant for different delay times  $t_{delay}$  as shown in Equation 5.4. Replacing  $Q_{tot}$  by  $Q_{pre}$  and  $Q_{col}$  and solving for  $Q_{col}(t_{d+\Delta t})$  leads to expression 5.6.

$$Q_{tot}(t_{delay}) = Q_{tot}(t_{delay} + \Delta t) \quad (5.4)$$

$$Q_{pre}(t_{delay}) + Q_{col}(t_{delay}) = Q_{pre}(t_{delay} + \Delta t) + Q_{col}(t_{delay} + \Delta t) \quad (5.5)$$

$$Q_{col}(t_{delay} + \Delta t) = Q_{col}(t_{delay}) - [Q_{pre}(t_{delay} + \Delta t) - Q_{pre}(t_{delay})] \quad (5.6)$$

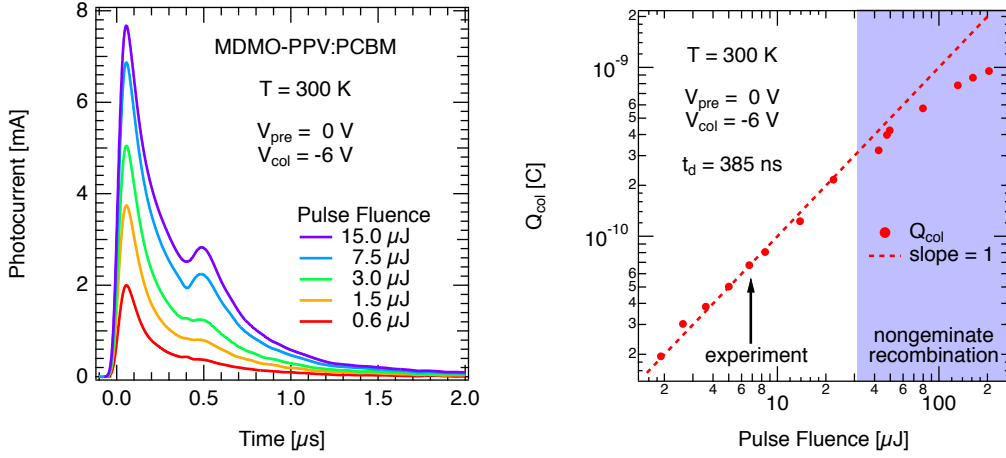


Figure 5.7: Illumination-dependent measurement of MDMO-PPV:PC<sub>61</sub>BM at room temperature. Left: TDCF signal for selected illumination intensities. Right: Illumination-dependence of the integrated collection peak charge  $Q_{col}$ . For low pulse fluences up to 30  $\mu\text{J}$ ,  $Q_{col}$  increases linearly (slope one) with laser intensity. Above 30  $\mu\text{J}$  nongeminate recombination leads to a sub-linear rise. For reliable measurement conditions in subsequent experiments, a laser intensity in the linear regime was chosen.

Assuming a homogeneous distribution of charge carriers in the device, the amount of charges, extracted after a defined delay time, is given by

$$Q_{col}(t_{delay}) = eALn(t_{delay}) \quad (5.7)$$

where  $A$  and  $L$  are size and thickness of the active layer, and  $n$  is the charge carrier density. Hence,  $n(t_{delay})$  can be expressed as

$$n(t_{delay}) = \frac{Q_{col}(t_{delay})}{eAL} \quad (5.8)$$

If we now take Langevin type bimolecular recombination into account, the amount of charges available for extraction after  $t_{delay}$  will decrease with increasing delay time. The change of the charge carrier density  $n$  due to a longer delay time  $t_{delay} + \Delta t$  is given by Langevin theory, including the bimolecular recombination factor  $\gamma$ :

$$\Delta n(t_{delay}) = \gamma n^2(t_{delay}) \Delta t \quad (5.9)$$

Therefore, Equation 5.6 has to be corrected for the charges lost in between  $t_{delay}$  and  $(t_{delay} + \Delta t)$  due to recombination:

$$Q_{col}(t_{delay}) = Q_{col}(t_{delay}) - [Q_{pre}(t_{delay} + \Delta t) - Q_{pre}(t_{delay})] - \Delta Q_{col}^{rec}(t_{delay}) \quad (5.10)$$



with

$$\Delta Q_{col}^{rec}(t_{delay}) = eAL\Delta n(t_{delay}) . \quad (5.11)$$

Inserting Equation 5.11 and 5.9 in 5.10 results in

$$Q_{col}(t_{delay} + \Delta t) = Q_{col}(t_{delay}) - [Q_{pre}(t_{d+\Delta t}) - Q_{pre}(t_{delay})] - \gamma \frac{Q_{col}(t_{delay})^2}{eAL} \Delta t \quad (5.12)$$

Here,  $Q_{col}$  and  $Q_{pre}$  for  $t_{delay}$  and  $(t_{delay} + \Delta t)$  are the experimentally determined values of two successive TDCF measurements with different delay times. Since  $A$  and  $L$  are also experimental accessible, the only fit parameter is the bimolecular Langevin recombination coefficient  $\gamma$ . Employing the fit routine shown above, the best  $\gamma$  to represent the experimental data was determined by using 15 iterations and a least square fit.

### 5.3.3 Impedance Spectroscopy

A powerful tool for electrical characterization of various materials and their interfaces is impedance spectroscopy (IS). Furthermore, IS offers the possibility to investigate the dynamics of charge carriers in the bulk and at the interface layers of a device. The method in itself is based on introducing a small perturbation by an alternating voltage signal to a system. Hence, an important prerequisite for the small perturbation is, that it must not influence the resulting measurement signal. In this section I will give a very brief overview, highlighting only some basic principles of impedance spectroscopy. For more detailed insights, I would like to refer the interested reader to the book of Barsoukov and Macdonald [78], on which this chapter is based.

#### Impedance

The impedance  $Z$  denotes the complex resistance of an electrical device under an alternating current (ac) signal. Analog to the classical case of a direct current (dc) it is defined as the ratio of the complex voltage and the complex current. This new concept of electrical impedance was introduced by Heaviside in the 1880s, who extended the existing concept of a dc resistance to a more general one. Due to the alternating current, capacitors and inductors result in a phase shift between current and voltage and therefore, a classical dc system can be seen as the special case of an ac system, when the phase shift of current and voltage equals zero.

In principle, there are two ways to describe the impedance as a complex quantity. The first one is in Cartesian coordinates

$$Z = Z' + iZ'' = R + iX , \quad (5.13)$$

where  $i$  is the imaginary unit,  $Z'$  the real part and  $Z''$  the imaginary part of the impedance. The real part corresponds to the classical ohmic resistance  $R$ , and the imaginary part is also denoted as reactance  $X$ , due to capacitors and inductors in the electrical circuit. The second possibility of describing the impedance is in polar coordinates as shown in Equation 5.14 with the absolute value of the impedance  $|Z|$  and the phase shift between current and voltage  $\Phi$ .

$$Z = |Z|e^{i\Phi} = |Z|(\cos(\Phi) + i \cdot \sin(\Phi)) \quad (5.14)$$

By using Euler's formula in Equation 5.14, the impedance can be represented as a vector in the complex plane as shown in Figure 5.8. Here,  $|Z| \cdot \cos(\Phi)$  describes the real part  $Re(Z)$  and  $|Z| \cdot \sin(\Phi)$  the imaginary part  $Im(Z)$  of the impedance. Therefore the length of the vector  $Z$  is given by

$$|Z| = \sqrt{(Re(Z))^2 + (Im(Z))^2} = \sqrt{R^2 + X^2}, \quad (5.15)$$

while the phase angle can be expressed as

$$\Phi = \arctan\left(\frac{Im(Z)}{Re(Z)}\right) = \arctan\left(\frac{X}{R}\right). \quad (5.16)$$

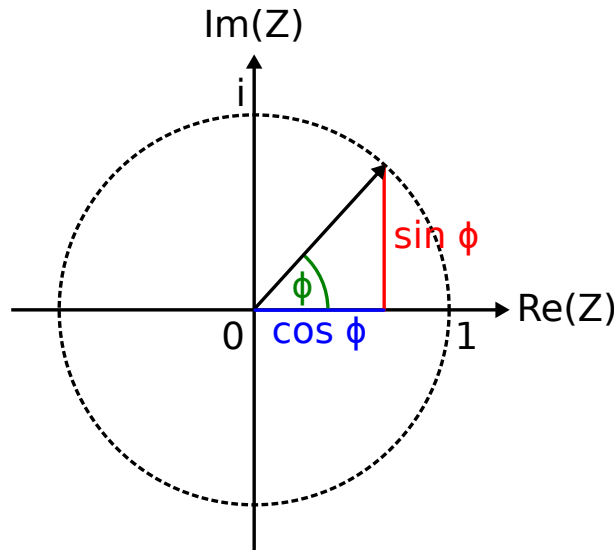


Figure 5.8: The impedance  $Z$  is displayed as a vector in the complex plane. Its projection to the abscissa denotes the real part and the projection to the ordinate the imaginary part of the impedance.

## Impedance Spectra

The first basic step for interpreting the impedance spectrum of a system is to plot the negative imaginary part versus the real part of the impedance, which is also known as Cole–Cole plot [79]. The aim is to describe the impedance spectrum by an equivalent circuit, which gives a physically reasonable interpretation of the behaviour of the device. Nevertheless, there are two major problems in the interpretation of an impedance spectrum. The first one is due to the fact that the models are based on ideal electrical elements, which is not suitable for real devices. And the second problem is the ambiguousness of the equivalent circuits, which means that different models can result in the same impedance spectrum. Hence, the equivalent circuit chosen for interpretation of the corresponding impedance spectrum should be as simple as possible and agree to the electrical properties of the device.

Some fundamental equivalent circuits with corresponding impedance spectra in Cole–Cole presentation are shown in Figure 5.9. Here,  $\omega$  denotes the angular frequency  $2\pi f$ , where  $f$  is the frequency of the ac probe signal. In (a) the impedance of a simple resistance is shown, which does not depend on the frequency of the ac signal. Hence, the imaginary part of the impedance is zero and the resulting single point on the real part axis corresponds to the classical dc resistance. In contrast, the impedance of a capacitor depends on the ac frequency and therefore results in a line perpendicular to the abscissa. In the case of an ideal capacitor, the real part of the impedance is zero (b). By connecting an additional resistance in series to the capacitance, the impedance spectrum of the latter is simply shifted in parallel by the value of the resistance  $R_S$  (c). If, in contrast, both devices (resistor and capacitor) are connected in parallel, the Cole–Cole plot will show a clear semicircle (d), starting at  $Re(Z) = 0$  for an infinitely high frequency. Thus, the capacitor is the dominating part of the equivalent circuit. The real part of the impedance increases with decreasing frequency until it reaches its maximum, when the frequency reaches zero. In this case, the imaginary part of the impedance is zero, too, and the parallel resistance  $R_P$  is dominating. An additional resistance connected in series to the former circuit results in a shift of the semicircle on the abscissa by the value of this series resistance  $R_S$  (e).

## Working Conditions

For investigation of the organic BHJ solar cells by impedance spectroscopy, we used an Agilent E4980A LCR-meter in parallel RC-circuit mode. While temperature-independent measurements were carried out in a nitrogen atmosphere glovebox system, the samples had to be transferred to a vacuum cryostat for the temperature-dependent ones. All experiments were conducted in

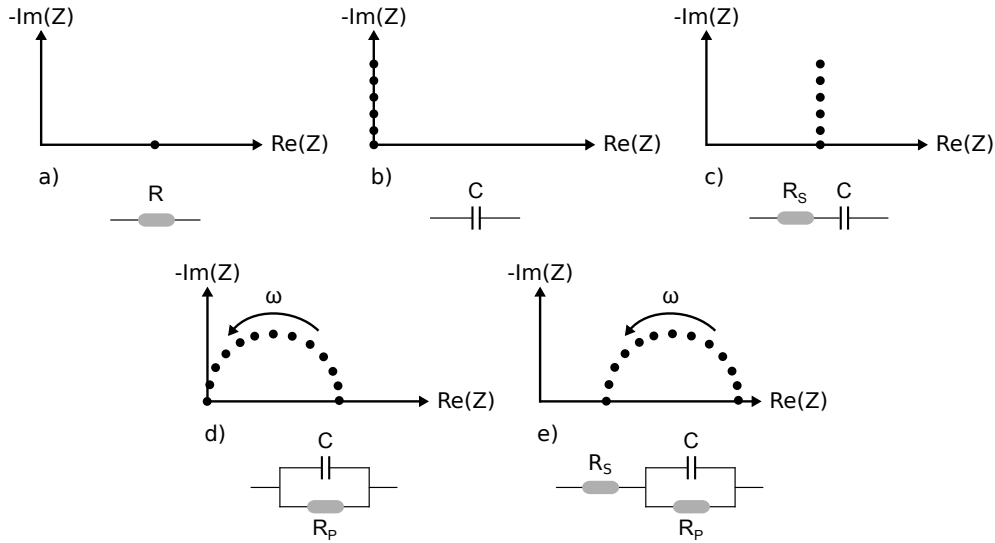


Figure 5.9: Cole–Cole diagrams for different basic equivalent circuits. A classical resistance corresponds to a single point on the abscissa (a), while the frequency-dependence of a capacitor results in a line perpendicular to the abscissa (b). If resistance and capacitance are connected in series, the line of the capacitor is shifted by the value of the resistance  $R_S$  on the abscissa (c). The parallel connection of  $R_P$  and  $C$  is depicted by a semicircle (d) that is again shifted on the abscissa, if another resistance is connected in series in front of the RC-element (e). The arrow below  $\omega$  indicates the dependence of the equivalent circuits on increasing frequency.

the dark to prevent additional capacitive effects in the device due to photogenerated charge carriers. To check the validity of the chosen parallel RC-circuit operation mode, frequency-dependent impedance measurements between 20 Hz and 2 MHz with a constant bias in reverse direction were done in advance. The resulting data showed a clear semicircle in Cole–Cole representation (see Figure 5.10, left), that was slightly shifted on the real part axis ( $R_S \sim 50 \Omega$ ). This behaviour indicates, that the equivalent circuit of organic BHJ solar cells can be represented by a small series resistance  $R_S$ , followed by another resistance  $R_P$  in parallel with a capacitance  $C$  (compare Figure 5.9 (e)). With increasing bias,  $R_P$  increases considerably up to several  $k\Omega$ , and hence the influence of  $R_S$  further decreases. Therefore, the LCR-meter can be operated in parallel RC-circuit mode.

For capacitance–voltage measurements a dc bias voltage sweep from -2 to 2 V was performed, which was superimposed by a small ac voltage. To prevent any influence of the probe signal to the measurement, it is very important to choose the right parameters as frequency and magnitude of the ac voltage.

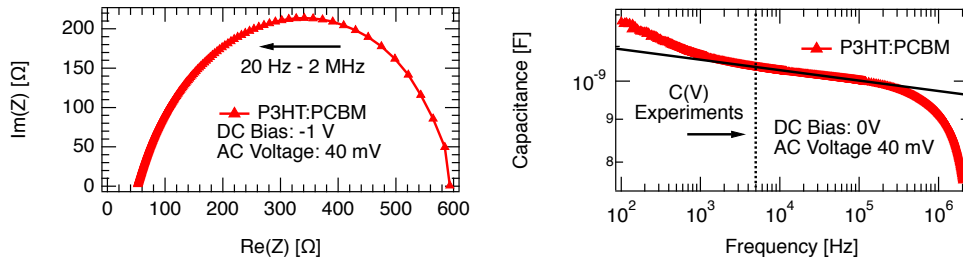


Figure 5.10: Frequency-dependent impedance measurement of an organic BHJ solar cell. Left: Cole–Cole representation shows a semicircle, which is slightly shifted on the real part axis. Corresponding equivalent circuit is shown in Figure 5.9 (e), but  $R_S \ll R_P$  and  $R_S$  can be neglected in the parallel RC-circuit mode of the LCR-meter. Right: Frequency-dependent capacitance: In the intermediate frequency region, indicated by the black solid line, the capacitance is almost frequency-independent. Thus, 5kHz was chosen for subsequent  $C(V)$  measurements.

Hence, we applied a signal amplitude of 40 mV, which is as low as possible, but still ensures a good signal to noise ratio. The appropriate ac frequency was extracted from a logarithmic capacitance versus frequency plot as shown in Figure 5.10 on the right. At very high frequencies, the charge carriers in the device are no longer able to follow the fast changes of the internal field and do no longer contribute to the capacitance. The measured capacitance therefore corresponds to the geometrical capacitance of the device (not visible, clearly beyond 2 MHz in Figure 5.10). In the mid-frequency range (here: 2 - 200 kHz) the free charge carriers contribute to the capacitance and the latter is nearly independent of the applied frequency. Below 1 kHz, an additional contribution to the capacitance due to trapped charge carriers arises. Hence, we chose 5 kHz for the ac signal, as it is in the frequency-independent regime of the measured capacitance and not yet influenced by the trapped charges.

### Mott–Schottky Analysis

Mott–Schottky analysis is a well-established tool in inorganic semiconductor physics, which was originally derived for a metal–semiconductor interface [80, 81, 82]. Furthermore, its validity for abrupt pn-junctions has been shown [83] and it has also been transferred to organic BHJ solar cells [84, 85, 86]. Since every impedance spectra can be described by an equivalent circuit, it is possible to calculate the corresponding capacitances and resistances correlated to the device. As shown in Figure 5.10, an organic BHJ solar cell can be represented by an RC-element (compare 5.9 (d)), since the additional series resistance in (e) is in most cases very small. Thus, the

impedance is given by Kirchhoff's law as

$$Z = \frac{R}{1 + i\omega RC} \quad (5.17)$$

The resistance and capacitance can therefore be calculated from the impedance by

$$R = \operatorname{Re} \left( \frac{1}{Z} \right) \quad C = \operatorname{Im} \left( \frac{1}{Z} \right) \frac{1}{\omega} . \quad (5.18)$$

By plotting one over the square of the capacitance versus the applied voltage, it is possible to extract the built-in potential  $V_{Bi}$  and the effective doping density  $N$  of a device via Equation 5.19 [83].

$$\frac{1}{C^2} = \frac{2}{e\varepsilon_0\varepsilon_s NA^2} \left( V_{Bi} - V - \frac{kT}{e} \right) \quad (5.19)$$

Here,  $V$  is the applied voltage,  $e$  the elementary charge,  $\varepsilon_0$  the vacuum permittivity,  $\varepsilon_r$  the dielectric constant and  $A$  the active area of the device. The interpretation of the Mott-Schottky plot in organic BHJ solar cells focusses on the region, in which  $1/C^2(V)$  depends linearly on the bias voltage and corresponds to the inorganic case. While the slope has been identified as a concentration of occupied trapping centers (acceptor doping density in the active layer) [84, 87], the intercept with the abscissa is attributed to the built-in potential [88]. As mentioned before, Mott-Schottky theory is valid for metal-semiconductor interfaces and abrupt pn-junctions. In contrast to these bilayer systems, its validity for organic BHJ solar cells, which consist of a blend of two materials, has not been proven yet and will be discussed in more detail in chapter 9.

### Determination of the Dielectric Constant

In case of a classical plate capacitor its geometrical capacitance ( $C_{geo}$ ) is inverse proportional to the thickness ( $L$ ) of the dielectric medium in between the capacitor plates as shown in Equation 5.20.

$$C_{geo} = \varepsilon_0\varepsilon_r \frac{A}{L} \quad (5.20)$$

Here,  $A$  is the area of the electrodes,  $\varepsilon_r$  the dielectric constant of the blend and  $\varepsilon_0$  the vacuum permittivity. Thus, the dielectric constant can be determined by measuring the geometrical capacitance in dependence of the thickness of the dielectric medium, which will be presented here for a photoactive layer containing P3HT and PC<sub>61</sub>BM in a 1:1 blend ratio. As electrodes we used

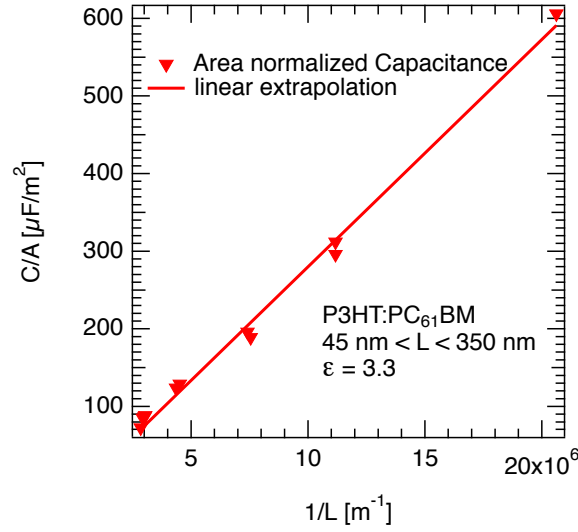


Figure 5.11: Area normalized capacitance vs. inverse active layer thickness of P3HT:PC<sub>61</sub>BM samples (ITO/blend/Ca/Al). The slope depends linearly on the dielectric constant, which agrees well to literature values [89].

ITO and Ca/Al (3 nm/ 100 nm) as for our organic BHJ solar cells and varied the active layer thickness from 45 to 350 nm. The geometrical capacitance was determined by capacitance–voltage measurements, which feature a constant capacitance at sufficiently high reverse bias as the active layer is totally depleted (compare section 9.1). When plotting the (area normalized) capacitance versus the inverse active layer thickness as shown in Figure 5.11, the slope of the linear fit to the experimental data is equal to  $\epsilon_0\epsilon_r$ . The resulting dielectric constant  $\epsilon_r = 3.3$  is in good agreement with literature values [89].

# Voltage-Dependent Photocurrent

---

In contrast to classical silicon solar cells, the photocurrent ( $J_{Light} - J_{Dark}$ ) of organic BHJ solar cells is dependent on the applied bias voltage, which reduces the fill factor and hence solar cell efficiency. However, this behavior cannot be explained by the Shockley diode equation [90]. In this chapter the voltage dependence as well as the symmetry of the photocurrent with respect to a point of optimal symmetry (POS) will be discussed for devices containing P3HT:PC<sub>61</sub>BM in a 1:1 blend ratio as photoactive layer. Meaning and origin of the POS will be explained via macroscopic device simulations. Furthermore the results will be compared to a model taking field-dependent polaron pair dissociation (Braun–Onsager) and voltage-dependent charge extraction (Sokol–Hughes) into account (see chapter 3). All data shown here was measured under an illumination level corresponding to one sun. The results presented in this chapter are based on the findings shown in paper 4 by Limpinsel et al. [51].

## 6.1 Point of Optimal Symmetry

Pulsed photocurrent measurements were conducted as described in chapter 5.3.1 in order to prevent any influence of device heating on the photocurrent. A typical, symmetric photocurrent curve of a P3HT:PC<sub>61</sub>BM device with a Ca/Al cathode is shown in Figure 6.1 (left), which is composed of two major contributions: The first one is voltage-dependent and exhibits a symmetric behavior with respect to the point of optimal symmetry. In contrast, the second contribution is a voltage-independent offset ( $J_{Ph}(V_{POS})$ ), which simply shifts the whole photocurrent curve and will be discussed in section 6.1.2 as it has a strong influence on the solar cell performance. The POS was found to occur typically in a voltage range of about  $V_{POS} \approx 0.52$  to  $0.64$  V for annealed P3HT:PC<sub>61</sub>BM samples with Ca/Al top contacts under an illumination level of one sun. These findings are in good agreement to those presented by Ooi et al. [70, 71], who observed the POS at about  $0.58$  to  $0.6$  V for similar samples with an aluminum cathode. In order to accentuate the high symmetry of the photocurrent, the origin was shifted to the POS in a logarithmic plot: In Figure 6.1 (right), photocurrent in reverse (i.e.  $V < V_{POS}$ )



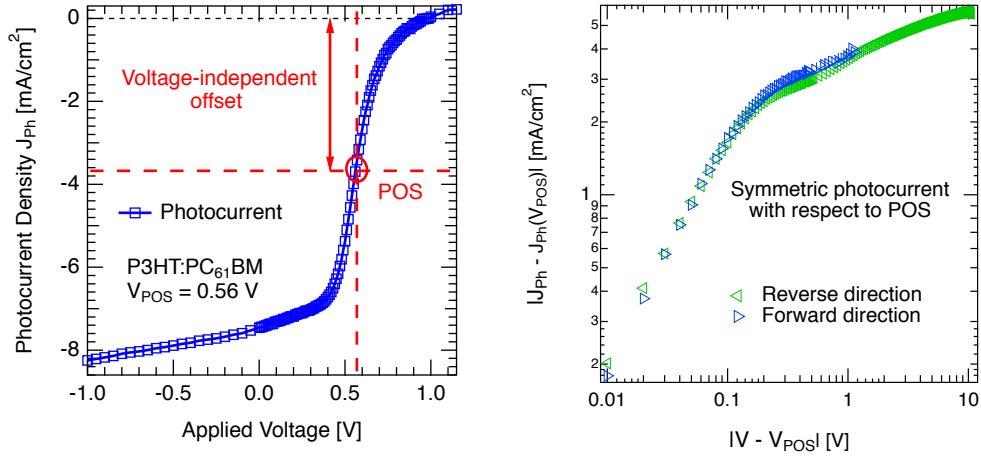


Figure 6.1: Left: Photocurrent density as determined by pulsed measurements under an illumination level of about one sun, which exhibits a point symmetry with respect to the point of optimal symmetry (red circle) and is shifted by an voltage-independent offset. Right: Logarithmic plot with origin being shifted to the POS to highlight the symmetric behavior.

and forward ( $V > V_{POS}$ ) direction are almost identical with a slightly higher current in forward direction. Charge injection in forward direction results in a higher charge carrier concentration in the device, which is able to explain the small deviation between reverse and forward photocurrent. In some samples, a small kink in the reverse photocurrent was observed, which could be attributed to the influence of air, as this kink clearly increased after exposing the sample to ambient air [91].

### 6.1.1 Origin of the Point of Optimal Symmetry

Although our experimental findings concur with those of Ooi et al., our interpretation of the POS deviates. By means of electroabsorption spectroscopy Ooi et al. identified the built-in potential of their devices ( $\sim 0.59$  V), which was in good agreement to  $V_{POS}$  from pulsed photocurrent measurements. Hence, they assumed  $V_{POS}$  to be equal to the built-in potential, despite an even higher open circuit voltage [71], which was in contrast to the conventional assumption of  $V_{Bi}$  being an upper limit for  $V_{OC}$  [92, 93, 34]. Later on it was shown by de Vries et al. that electroabsorption measurements of organic light emitting diodes (OLED) do not yield the built-in potential, in contrast to inorganic systems [94].

An explanation for the POS being not equal to the built-in potential can be found by taking a closer look at the definition of the built-in potential itself.

In a classical pn-junction,  $V_{Bi}$  refers to the case of flat energy bands in the whole device and thus zero electric field. However, in our case significant band-bending occurs in the vicinity of the metal contacts [95], which is up to several tenths of eV as shown by Kelvin probe measurements [96]. These findings of diffusion-induced band-bending were confirmed by calculations of Kemerink et al. for a semi-finite system with zero net injection, taking the drift-diffusion equation, Einstein relation and the Poisson equation into account [97]. In addition, the band-bending was also observed in our macroscopic simulations of the band structures, which are based on numerical, iterative solutions of the one-dimensional Poisson equation and the continuity equations for electrons and holes [51] (see Figure 6.2). Thus, in our organic systems the built-in potential does not correspond to flat band conditions across the whole device. Due to band-bending at the contacts the local electric field is finite while the total electric field is zero, as expected. This case, when a voltage equal to the built-in potential is applied to the sample, is shown in Figure 6.2 from macroscopic simulations of an organic solar cell (dashed lines: red for polymer HOMO, blue for fullerene LUMO).

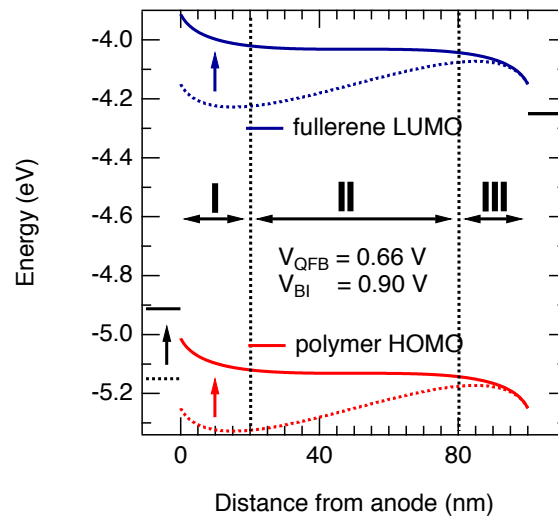


Figure 6.2: Simulated energy band diagram of an organic BHJ solar cell with ITO (left black line) and metal (right black line) contacts and an active layer thickness of 100 nm. For an applied voltage equal to  $V_{Bi}$  the HOMO and LUMO levels match at the contacts (dashed lines). Due to diffusion-induced band-bending at the contacts, the local electric field across the whole device is finite, while the total one is zero. At a lower applied voltage ( $V_{QFB} < V_{Bi}$ , solid lines) the energy bands are flat in the bulk of the device (region II) and finite in the vicinity of the contacts (regions I and III).

From this point of view a clearly better measure for flat band conditions in the device is the situation we denote as the case of quasi-flat bands (QFB) [51]. At a potential  $V_{QFB} < V_{Bi}$  flat energy bands can be reached in the bulk of the device as shown in Figure 6.2 (solid lines). Kemerink et al. first proposed this reduced voltage, but incorrectly identified it as the voltage  $V_0$  where the photocurrent is zero [97]. At the quasi-flat band potential, the electric field is zero in the bulk (region II) and finite in the vicinity of the contacts (regions I and III). The change of the externally applied voltage was indicated by the shift of the ITO contact energy level (black, left side) from  $V_{Bi}$  (dashed) to  $V_{QFB}$  (solid). This zero field situation in the bulk of the device means that a relative change of the applied bias in either direction results in the same change of the electric field for the photogenerated charge carriers in the device, but with opposite sign. Thus, a symmetric behavior of the photocurrent can be expected with respect to the case of QFB and not the built-in potential. We therefore attribute the experimentally determined POS to the case of QFB [51]. In favor of this interpretation are our findings that the POS is well below the built-in potential, as determined by temperature-dependent measurements of the open circuit voltage, and does not depend on the active layer thickness (see also Figure 9.2) [98]. Furthermore, the magnitude of diffusion-induced band-bending for both contacts can be estimated by the difference between  $V_{Bi}$  and  $V_{POS}$ . For P3HT:PC<sub>61</sub>BM at room temperature the difference is about 0.14 V, which leads to reasonable injection barriers  $\Phi_e$  and  $\Phi_h$  for electrons and holes of about 0.07 eV, each. These findings are in good agreement to  $V_{OC}(T)$  measurements, which allow for the determination of the effective band gap  $E_g$  and the built-in potential [34] and hence the sum of the injection barriers  $\Phi_e + \Phi_h = E_g - V_{Bi}/e \approx 0.14$  eV [98].

### 6.1.2 Voltage-Independent Offset

Another major contribution to the pulsed photocurrent curve is its voltage-independent offset  $J_{Ph}(V_{POS})$ . As the POS is close to the maximum power point, i.e. working conditions of the solar cell, the photocurrent is largely determined by  $J_{Ph}(V_{POS})$ . Hence, a highly negative offset is crucial for high power conversion efficiencies and needs to be optimized. We therefore investigated several processing parameters as thermal treatment, cathode material or active layer thickness, which influence the voltage-independent offset without altering the shape of the photocurrent curve.

In Figure 6.3 (left) the influence of thermal annealing of the active layer on the voltage-independent offset is shown. As reference, a pristine sample (black dashed line) without any thermal treatment of the active layer was chosen. All other samples were annealed for 10 minutes on a hotplate prior

to the evaporation of the cathode. While annealing at 140 °C resulted in a negative shift of the voltage-independent offset and thus better performance of the device, lower (80 °C) or higher (200 °C) annealing temperatures reduced the offset. These findings fit well to the results of Ma et al., who investigated the dependence of short circuit current, fill factor and device efficiency on the annealing temperature and found maxima at about 150 °C [99].

The influence of the cathode material on the voltage-independent offset is shown in Figure 6.3 (right), where a solar cell with a conventional Ca/Al cathode (green open squares) is compared to one with an Ag electrode (blue open triangles). The corresponding offsets  $J_{Ph}(V_{POS})$  are indicated by the green and blue horizontal lines. As expected, the negative offset of the better performing Ca/Al device was much larger than the one of the Ag device. The latter was almost zero, resulting in a much lower short circuit current in case of the Ag cathode. Nevertheless, the shapes of both photocurrent curves were still similar. In addition, the POS of the Ag devices ( $V_{POS} \approx 0.45$  V) was smaller than in standard Ca/Al devices, which can be attributed to the higher injection barriers and therefore lower band-bending at the contacts. These findings indicate that the contact regions are responsible for the voltage-independent offset. The voltage-dependent contribution to the photocurrent can thus be attributed to the bulk of the device [51].

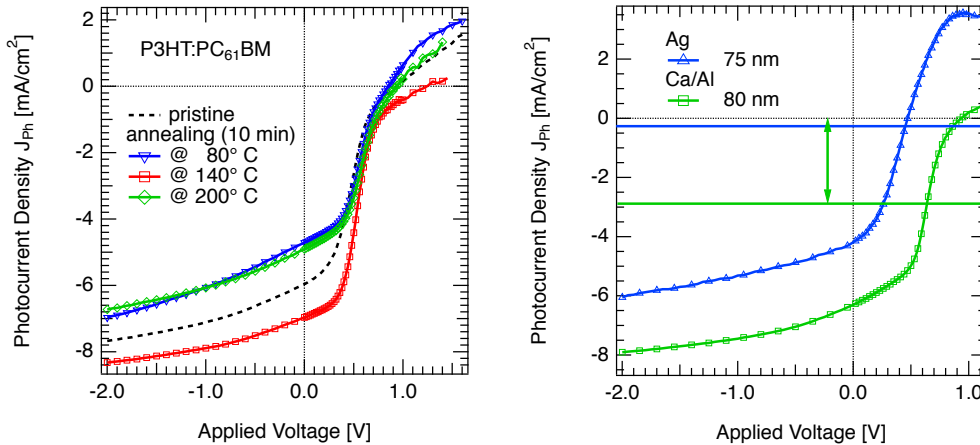


Figure 6.3: Influence of thermal annealing of the active layer (left, standard device with Ca/Al cathode) and cathode material (right) on the voltage-independent offset of the photocurrent.

Ooi et al. explained the voltage-independent offset with self-selective electrodes and predicted an inverse dependence of  $J_{Ph}(V_{POS})$  on the active layer thickness [71]. However, this dependence could not be verified by our measurements. Instead we found a maximum offset for a distinct active layer

thickness (not shown) [91, 51]. A more appropriate explanation of the voltage-independent offset is the band-bending at the contacts. It is independent of the applied bias and causes an electric field in the vicinity of the contacts, which is capable of efficiently dissociating polaron pairs (see Figure 6.2). This field results in a constant contribution to the photocurrent due to the contact regions, which depends on the degree of band-bending and therefore the height of the injection barriers. Hence, the bulk of the solar cell gives rise to the voltage-dependent contribution to the photocurrent and therefore the symmetric behavior with respect to the POS.

## 6.2 Modeling the Photocurrent

The previous sections introduced the POS, explained its origin and discussed how cathode material and thermal treatment influence the voltage-independent offset and thus the power conversion efficiency of the devices. Here, a combined model based on Braun–Onsager theory for field-dependent polaron pair dissociation and Sokel–Hughes theory for voltage-dependent charge extraction will be discussed in order to describe the voltage-dependent contribution to the photocurrent, which is responsible for the symmetric shape. This model has already been introduced in chapter 3 and lead to Equation 3.13, which is able to describe the photocurrent over a wide range of device parameters such as active layer thickness or cathode material. However, in some cases a dimensionless factor  $n$  scaling the voltage for charge extraction had to be introduced. This factor has no directly accessible physical meaning, but accounts for several effects as for example material properties, the reduced electric field in the device due to band-bending at the contacts and good ( $n < 1$ ) or bad ( $n > 1$ ) charge extraction characteristics at the electrodes.

$$J_{Ph}(V) = J_{Ph,max} \cdot \left[ \coth \left( \frac{eV}{2nk_B T} \right) - \frac{2nk_B T}{eV} \right] \cdot P_{Braun}(F) \quad (6.1)$$

The good accordance of the combined model of Braun–Onsager and Sokel–Hughes theory to the experimental data is demonstrated in Figure 6.4 in a logarithmic (left) and linear (right) scale for different kinds of solar cells. To highlight the point symmetry with respect to the POS, the origin in the logarithmic plot was shifted to the point of optimal symmetry and thus the effective photocurrent ( $|J_{Ph} - J_{Ph}(V_{POS})|$ ) was plotted versus the effective voltage ( $V_{eff} = |V - V_{POS}|$ ). Forward and reverse direction correspond to  $V > V_{POS}$  and  $V < V_{POS}$ , respectively. In addition, the graph shows the polaron pair dissociation probability ( $P_{Braun}(F)$ ), the charge extraction after

Sokel and Hughes ( $SH(V)$ ) and the combined model (red line), which agrees well to the experimental data.

We point out that the polaron pair dissociation yield at zero field is about 40 to 60% for standard devices, which means that the electric field in the bulk is clearly reduced by the injection barriers and thus band-bending at the contacts. Nevertheless, the extraction term is dominating for low effective voltages and determines the shape of the photocurrent, while the influence of the field-dependent polaron pair dissociation is only observable at higher effective voltages. The electric field was approximated by  $F = V_{eff}/L$ , which is not entirely correct, as the field in the bulk of the device is reduced due to band-bending at the contacts [51]. Hence, higher active layer thicknesses ( $L \approx 400$  nm) than experimentally determined would be necessary to fit the experimental photocurrent. As already mentioned above, this can be corrected by a factor  $n > 1$ .

The linear plot (Figure 6.4, right) was simply shifted by the voltage-independent offset  $J_{Ph}(V_{POS})$  and illustrates the good agreement of model (solid lines) and experimental data (symbols) for devices with clearly different active layer thickness and cathode materials. In all cases, only small variations of the fit parameters were necessary to describe the experimentally determined photocurrent [91]. The devices applying Ag cathodes needed a slightly higher extraction factor  $n$  up to 1.5, which can be attributed to a worse charge extraction in comparison to the Ca/Al devices.

$J_{Ph,max} = eGL$ , with  $G$  being the generation rate, was used here as a single parameter and determined by the saturated photocurrent at high reverse bias of about -10 V. The dielectric constant  $\epsilon_r$  of the 1:1 blend ratio P3HT:PC<sub>61</sub>BM was set to 3.5, being the average value of the dielectric constants (3 and 4 for P3HT and PC<sub>61</sub>BM, respectively) of both materials. We found  $\epsilon_r = 3.3$  by capacitance–voltage measurements (see section 5.3.3), which agree to the previous estimation within the limits of accuracy.

Even though the spatially averaged mobility  $\mu$  (sum of electron and hole mobility) and the polaron pair lifetime  $\tau_f$  (with respect to decay to the ground state) are distinct parameters, the  $\mu\tau_f$  product was used as a single parameter due to their linear dependency [47].  $\mu\tau_f$  was set to  $1 - 3 \times 10^{-14}$  m<sup>2</sup>/V and gives in combination with  $\mu \approx 5 \times 10^{-8}$  m<sup>2</sup>/Vs [100] an estimation for the polaron pair lifetime of several tens of picoseconds [101]. However, the experimentally determined lifetimes are in the range of several ns. This points at a major obstacle of classical models such as Braun–Onsager theory, as they cannot predict high polaron pair dissociation yields with these short lifetimes. Deibel et al. explain this discrepancy by considering  $\tau_f$  to be an effective polaron pair lifetime [102], accounting for a reduced recombination probability due to interface dipoles [103].

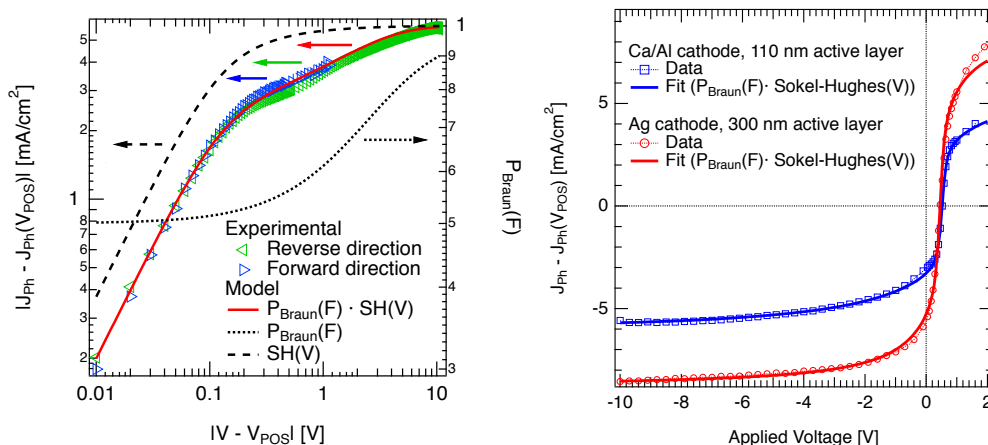


Figure 6.4: Left: The combined model (red line) of Braun–Onsager (polaron pair dissociation, right axis) and Sokel–Hughes (charge extraction, left axis) theory is able to describe the experimental photocurrent in forward (blue) and reverse (green) direction of a device with Ca/Al cathode. Right: The same model (solid lines) is also able to describe the experimental data (symbols) for devices with different cathode materials and active layer thicknesses.

The spatial separation of the polarons  $r_{PP}$  was set to values between 1.8 and 2.0 nm, which is in good accordance to Monte Carlo simulations [102]. In case of the simulations,  $r_{PP}$  was interpreted as an effective radius of the polaron pair, with the hole being delocalized on the polymer over several conjugated units. In 2004 Mihailetschi et al. presented a modified Braun–Onsager model, which assumed a Gaussian distribution of polaron pair radii in disordered materials [50]. However, a comparison of both models (fixed and gaussian distributed  $r_{PP}$ ) lead to the conclusion that fixed polaron pair radii resulted in better agreement for our experimental data to the Braun–Onsager model [91].

Another interesting fact of the combined Braun–Onsager and Sokel–Hughes model is, that the active layer thickness had only little influence on the voltage dependence of the photocurrent [51]. This is remarkable, as Braun–Onsager theory was used to describe a field-dependent polaron pair dissociation. As stated before, one reason for this unexpected behavior is the not entirely correct approximation of the internal electric field due to injection barriers at the contacts. Furthermore, these findings indicate that the Braun–Onsager model might overestimate the influence of field-dependence on polaron pair dissociation. This assumption is supported by previous results from Monte Carlo simulations [104], time-delayed collection field [105] and transient absorption measurements [58], which show a low field-dependence of about 10

to 15% for P3HT:PC<sub>61</sub>BM between short circuit and open circuit conditions. Here, the major part of free charge carriers is either generated directly or via an excited, hot, charge transfer state, which are both fast processes on the timescale of tens of picoseconds [101] (see chapter 4). However, the influence of field-dependent charge photogeneration varied considerably for different material systems (e.g. MDMO-PPV:PC<sub>61</sub>BM or PCPDTBT:PC<sub>71</sub>BM), and will be discussed in more detail in chapters 7 and 8. Hence, for high efficiency solar cell materials with almost no field-dependent charge photogeneration, the Braun–Onsager model might need to be modified to account for the more efficient polaron pair dissociation.

Another important factor influencing the photocurrent of solar cells are losses due to different kinds of recombination processes during charge generation and extraction as explained in chapter 4. Hence, it is crucial to understand the nature of these loss mechanisms in order to better understand the underlying physics of the voltage-dependent photocurrent. Street et al. claim to be able to deduce the dominating recombination process from illumination-dependent photocurrent measurements. They found a strong overlap of the photocurrent curves for various low (up to 0.3 sun) illumination intensities and conclude that the predominant recombination process is monomolecular [106]. However, Deibel et al. showed that it is also possible to reproduce this illumination-dependence with macroscopic simulations, applying a bimolecular model without any first order recombination [107]. Thus, voltage-dependent photocurrent measurements as described in this chapter are not sufficient to investigate recombination processes in organic BHJ solar cells. In the subsequent chapters 7 and 8, I will therefore focus on time-delayed collection field measurements to gain further insights in the recombination dynamics of organic BHJ solar cells.

## 6.3 Conclusion

In this chapter, the voltage-dependent photocurrent of organic BHJ solar cells was investigated by means of pulsed photocurrent measurements, as proposed by Ooi et al. [71, 70]. In addition, the experimental data were compared to a combined model for field-dependent polaron pair dissociation and charge extraction, as introduced in chapter 3. In good agreement to the previous work mentioned above, the photocurrent of our P3HT:PC<sub>61</sub>BM devices featured a symmetric behavior with respect to the point of optimal symmetry (POS) at about 0.53 to 0.64 V. However, our interpretation clearly differed, as we assigned the POS to the case of quasi-flat energy bands (QFB). Macroscopic simulations showed, that diffusion-induced band-bending at the contacts re-



sults in a reduced voltage ( $V_{POS} = V_{QFB} < V_{Bi}$ ), which accounts for flat energy bands in the bulk of the device, but a finite field at the contacts. As the field is zero in the bulk and changes symmetrically in both directions, a symmetric behavior with respect to the QFB is reasonable. As expected, we found the POS to be independent on the active layer thickness and comparisons to the built-in potential lead to acceptable injection barriers of 0.07 V at each contact.

Furthermore, we found the photocurrent to be composed of two major contributions. The first one is the voltage-independent offset. As a high offset is crucial for good solar cell performance, we investigated the influence of thermal treatment and cathode material on the photocurrent. While the offset was shifted, depending on the processing parameters, the shape of the photocurrent was not altered and thus we attributed the voltage-independent offset to the band-bending at the contacts. The second contribution to the photocurrent is voltage-dependent, related to the bulk properties and can be described by the combined model of Braun–Onsager and Sokel–Hughes with respect to the POS. A wide range of different solar cells (variation in cathode material and active layer thickness) could be described very well by the model, with only small variations of the parameters. Nevertheless, we also observed limitations to the model, as the approximation of the electric field is not entirely correct and does not take band-bending at the contacts into account. Furthermore, the influence of field-dependent polaron pair dissociation is overestimated, as in some material systems (e.g. P3HT:PC<sub>61</sub>BM) only a small part of the charge carrier generation (10 - 15%) is field-dependent. As shown by Deibel et al. [107] illumination-dependent photocurrent measurements are not sufficient to investigate the recombination dynamics in the device. Thus, the latter were investigated by time-delayed collection field measurements as shown in the following chapters.

# Charge Photogeneration and Recombination

---

So far, the overall photocurrent of organic BHJ solar cells was investigated. In this chapter, we will take a closer look at the underlying processes limiting the device performance, which are basically charge photogeneration and recombination. For highly efficient solar cells, a fast generation of free charge carriers is crucial, while the losses due to recombination need to be minimized [20, 8]. We applied temperature-dependent time-delayed collection field measurements to study two well-known reference systems, namely MDMO-PPV:PC<sub>61</sub>BM and P3HT:PC<sub>61</sub>BM. In the first part of this chapter, the influence of geminate recombination and field-dependent polaron pair dissociation on charge photogeneration will be discussed. The second part will address the nongeminate recombination processes in the devices. The results presented here are based on the findings reported in paper 7 by Mingeback et al. [105].

## 7.1 Field-Dependent Polaron Pair Dissociation

As already explained in chapter 4, there are three major scenarios for generation of free charge carriers in organic BHJ solar cells. The first one is via a thermalized charge transfer state (CTS) and therefore exhibits a field-dependence, as the Coulomb binding energy of the polaron pair needs to be overcome [47, 108]. In contrast, the other scenarios circumvent this obstacle, as the free charge carriers are either generated directly or via an excited, “hot”, CTS [57]. Hence, the latter two processes are desirable for high efficiency devices, as they are ultrafast and reduce the amount of geminate recombination losses. The samples investigated in this chapter applied active layers of either MDMO-PPV:PC<sub>61</sub>BM or P3HT:PC<sub>61</sub>BM with thicknesses of 90 and 155 nm, respectively, and exhibited power conversion efficiencies of 1.3% and 3.2% with fill factors of 48% and 67%. In order to exclude the influence of nongeminate recombination in the field-dependent measurements, the illumination intensity was chosen low enough to scale linearly with the amount of charges extracted by the collection field (see section 5.3.2). Delay time and collection voltage were set to 385 ns and -6 V, respectively, while the prebias was varied from

-5 V to the open circuit voltage of the sample. The results for both material systems are depicted in Figure 7.1 and were normalized to  $Q_{tot}(-5V)$  for a better comparability of both data sets.

In case of MDMO-PPV:PC<sub>61</sub>BM (left graph) the total amount of charges  $Q_{tot}$  (purple diamonds) was clearly dependent on the prebias applied during the delay time and decreased to about 30% of its maximum, not yet saturated value, when the internal field approached zero ( $V_{pre} \approx V_{OC}$ ). The field-dependence under high reverse bias can be mainly attributed to field-dependent charge photogeneration, as the influence of geminate and nongeminate recombination are negligible in this regime. While nongeminate recombination can be neglected due to the low illumination level for  $V < 0$  V, geminate recombination is inhibited by the high internal fields, even though free charge carriers are generated via the thermalized CTS route. However, the field-dependence of  $Q_{tot}$  becomes more pronounced for lower internal fields, as an additional contribution due to geminate recombination arises. With decreasing internal field less charges are extracted during  $t_{delay}$  and therefore  $Q_{pre}$  (red triangles) decreases. As no additional charges are extracted by the collection field ( $Q_{col}$  remains constant, green triangles), the “missing” charges are lost due to geminate recombination during  $t_{delay}$ . Hence,  $Q_{tot}$  as the sum of  $Q_{pre}$  and  $Q_{col}$  decreases considerably and leads to the conclusion, that free charge carriers are generated via a thermalized CTS with a fraction clearly exceeding 70%. These findings are in good agreement to photoluminescence measurements, which determined high exciton binding energies of up to 200 meV [55, 56] and support our scenario of charge photogeneration.

The corresponding graph for P3HT:PC<sub>61</sub>BM is shown on the right side of Figure 7.1.  $Q_{tot}$  exhibits a very weak field-dependence of less than 20% between -5 V and open circuit conditions, even though  $Q_{pre}$  clearly decreases with the internal field. But in contrast to MDMO-PPV:PC<sub>61</sub>BM, this decreasing  $Q_{pre}$  is compensated by an increasing  $Q_{col}$ . The charge carriers not extracted during  $t_{delay}$ , because of the lower internal field, do not recombine geminately and can therefore be extracted by the collection field, resulting in an almost constant  $Q_{tot}$ . The weak dependence on the electric field can be attributed to field-dependent charge photogeneration as explained above. Nevertheless, a minor influence of the thermalized CTS (especially at low internal fields) cannot be excluded. The overall field-dependence of 20% can therefore be interpreted as an upper limit for the fraction of geminate recombination in free charge carrier generation. These findings agree well to previous reports based on Monte Carlo simulations [104] and our photocurrent measurements [51] (see chapter 6), which detected a field-dependence of about 15%. In addition, transient absorption measurements indicated fast direct generation of free charge carriers with an upper limit for geminate re-

combination of about 15% [58]. These results lead to the conclusion that most free charge carriers in P3HT:PC<sub>61</sub>BM are either generated directly or via a “hot” CTS. Both scenarios provide very efficient charge photogeneration with high yields.

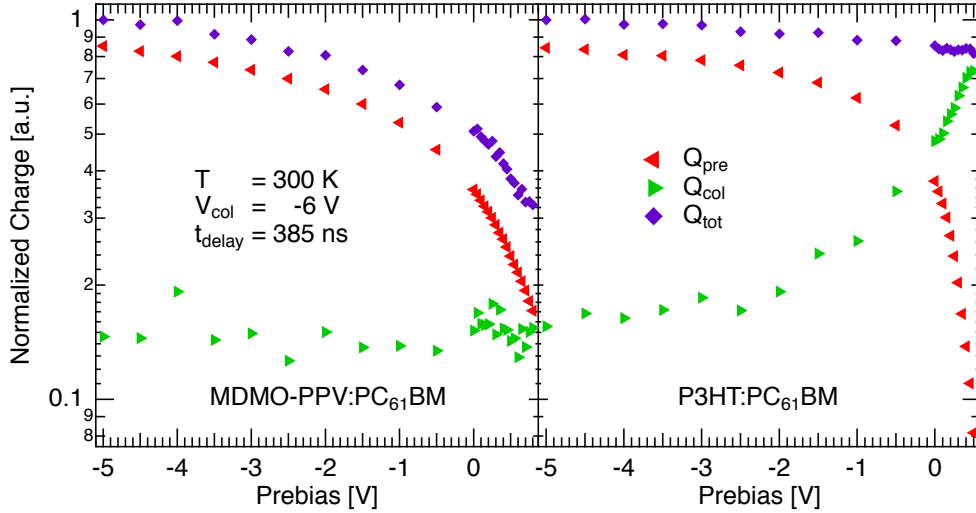


Figure 7.1: Field-dependence of charge photogeneration: For MDMO-PPV:PC<sub>61</sub>BM (left)  $Q_{tot}$  (purple diamonds) clearly depends on the internal electric field, which can be explained by free charge generation via a thermalized CTS. In contrast, P3HT:PC<sub>61</sub>BM (right) is almost independent on the field as almost all charges not extracted by the prebias are extracted by the collection field (increasing  $Q_{col}$ , green triangles). This indicates, that free charge carriers are either generated directly or via a “hot” CTS.

To verify our findings, we performed temperature-dependent TDCF measurements between 180 and 300 K. In case of the CTS mediated charge carrier generation, the polaron pair dissociation is not only influenced by the internal field, but is also thermally activated. However, this effect was expected to be rather small, as the thermal energy at room temperature  $k_B T \approx 25$  meV is already small in comparison to the exciton binding energy of up to 200 meV. Figure 7.2 shows the results of the temperature-dependent measurements for MDMO-PPV:PC<sub>61</sub>BM (left) and P3HT:PC<sub>61</sub>BM (right). The data were normalized to  $Q_{tot}(-5V)$  to provide a better comparability of the different temperatures, even though not all curves were saturated, yet. The latter results in a slight underestimation of the temperature effect, observable for MDMO-PPV:PC<sub>61</sub>BM. As expected, the field-dependence increases with decreasing temperature and supports our understanding of free charge generation via a

thermalized CTS. For lower temperatures, the thermal energy is reduced to 15 meV at 180 K and thus, it is more difficult to overcome the exciton binding energy. In contrast, the already weak field-dependence of P3HT:PC<sub>61</sub>BM is not influenced by any temperature effects in the investigated temperature regime. These findings are also in good agreement to our scenario of fast, highly efficient generation of free charge carriers, as mentioned above.

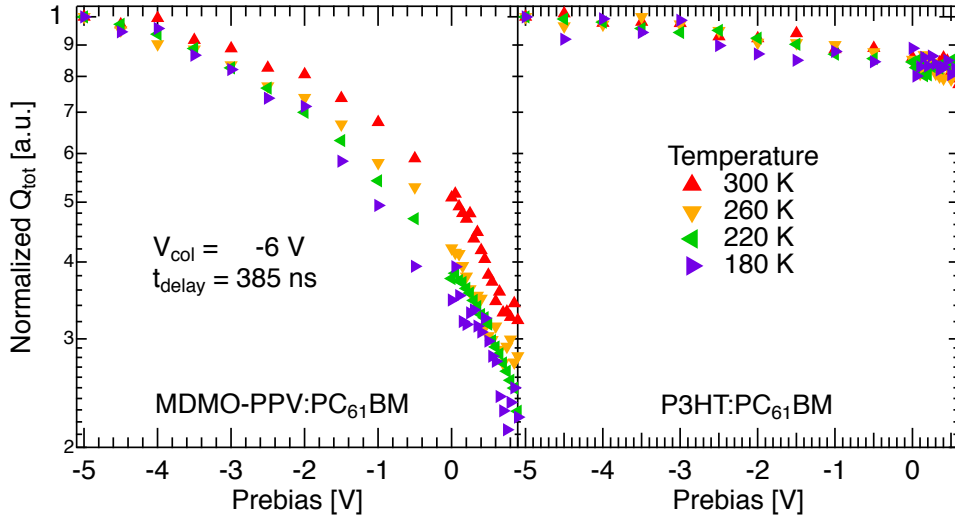


Figure 7.2: Field and temperature-dependent charge photogeneration. In MDMO-PPV:PC<sub>61</sub>BM (left) the increasing field-dependence for lower temperatures accounts for a thermally activated process, according to CTS mediated free charge carrier generation. In P3HT:PC<sub>61</sub>BM (right) no temperature-dependence is observable, supporting the scenario of direct free charge generation or via a “hot” CTS.

In comparison to the results from our pulsed photocurrent measurements (see section 6.2), these findings also indicate that the Braun–Onsager model overestimates the influence of field-dependent polaron pair dissociation. As shown in this chapter, the fraction of field-dependent processes in P3HT:PC<sub>61</sub>BM is limited to a maximum of about 20%, while most of the free charge carriers are generated via a different, more efficient route. Thus, the Braun–Onsager model should be more appropriate for material systems with a stronger field-dependence, such as MDMO-PPV:PC<sub>61</sub>BM.

## 7.2 Nongeminate Recombination

After canceling out nongeminate recombination (see section 5.3.2) in the last section to study the geminate processes, we now focus on the nongeminate processes. To do so, prebias and collection field were set constant in the corresponding TDCF measurements while the delay time was varied between 150 ns and 100  $\mu$ s. As geminate recombination is a very fast process, its influence is independent on the delay time. Thus, the variation of  $t_{delay}$  solely affects the amount of bimolecular recombination in the device. To make sure that charge carriers were only lost due to bimolecular recombination during delay time, we chose open circuit conditions as prebias to prevent a current flow in the sample. However, it is important to note that we applied  $V_{OC}$  as determined by a sun simulator under an illumination level equal to one sun. Thus, as  $V_{OC}$  depends on the charge carrier density in the device (e.g. illumination) [34],  $V_{OC}(\text{sun simulator})$  is not necessarily equal to  $V_{OC}(\text{laser})$ . Hence, it was not possible to completely avoid current flow. Nevertheless, this effect was negligible, as bimolecular recombination was still the dominating process in our measurements and extraction was accounted for.

The data for MDMO-PPV:PC<sub>61</sub>BM and P3HT:PC<sub>61</sub>BM is shown in Figure 7.3. As expected,  $Q_{pre}$  (red triangles) increases with increasing delay time, while  $Q_{col}$  (green triangles) decreases. The resulting  $Q_{tot}$  (purple diamonds) also decreases with increasing delay time due to bimolecular recombination. In order to determine the Langevin recombination prefactor  $\gamma$  (see Equation 4.2), we applied an iterative fit forward in time (black dashed line), which was introduced by Kniepert et al. [77]. As previously shown in section 5.3.2, this fit routine is solely based on bimolecular recombination and agrees well to the experimental data for both material systems. Neglecting bimolecular recombination in the model, e.g. taking only charge extraction into account, yields the yellow dash-dotted line.

In case of MDMO-PPV:PC<sub>61</sub>BM, the model gave the best agreement to the experimental data for  $\gamma = 8.2 \times 10^{-17} \frac{m^3}{s}$ . In order to decide, if the recombination process investigated here was really Langevin type, we calculated the reduction factor  $\zeta$ , which is based on Equation 4.2 and defined as

$$\zeta = \gamma \cdot \frac{\epsilon_r \epsilon_0}{e\mu} \quad (7.1)$$

with elementary charge  $e$  and  $\mu$  being the average electron and hole mobility. Assuming an approximated dielectric constant of  $\epsilon_r = 3.5$  and  $\mu = 3 \times 10^{-8} \frac{m^2}{Vs}$  [109], the resulting  $\zeta$  is about 0.5 and thus close to unity. We therefore conclude that the recombination is Langevin type at room temperature for this material system, which is in good agreement to literature [110]. In contrast,

the corresponding Langevin recombination prefactor for P3HT:PC<sub>61</sub>BM of  $\gamma = 5.3 \times 10^{-18} \frac{m^3}{s}$  is more than one order of magnitude smaller than for the PPV based device. Even though the extracted  $\gamma$  is consistent with literature [77], such a low recombination prefactor is surprising at first glance, since mobility ( $\mu = 5.5 \times 10^{-8} \frac{m^2}{Vs}$  [100, 111]) and dielectric constant ( $\epsilon = 3.3$ ) are similar to MDMO-PPV:PC<sub>61</sub>BM. Altogether, this results in a very small reduction factor of  $\zeta \approx 0.02$ , which is able to explain the discrepancy between both material systems and accords to previous findings [64, 112].

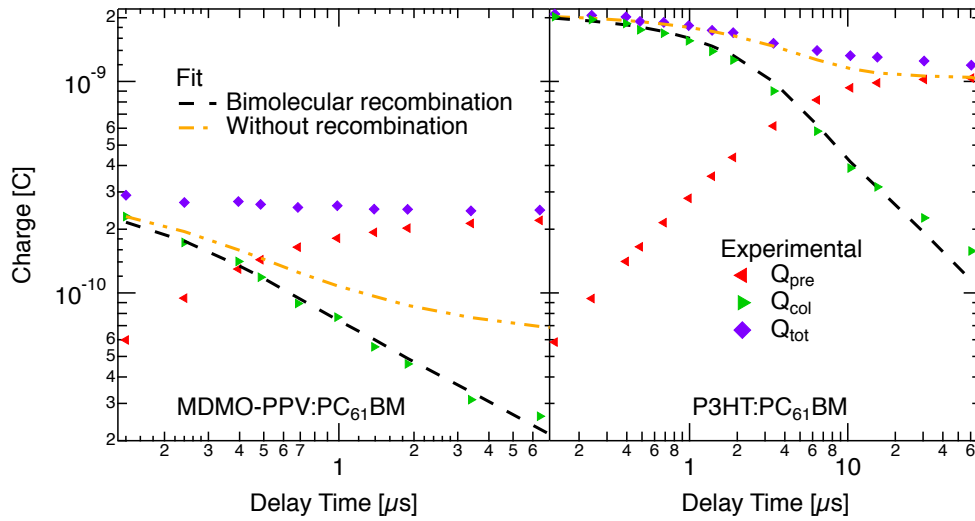


Figure 7.3: Time-delay dependent measurements of MDMO-PPV:PC<sub>61</sub>BM (left) and P3HT:PC<sub>61</sub>BM (right). The samples were kept under open circuit conditions during  $t_{delay}$  to prevent a current flow.  $Q_{tot}$  decreases due to bimolecular recombination. To extract the Langevin recombination prefactor,  $Q_{col}$  was modeled by an iterative fit forward in time, solely based on bimolecular recombination.

An explanation for this strongly reduced Langevin recombination in P3HT:PC<sub>61</sub>BM was given by Deibel et al. [64]. They attributed the discrepancy between theoretical and experimental Langevin recombination prefactor (e.g.  $\zeta$ ) to the incorrect assumption in Langevin theory of spatially constant charge carrier densities for electrons  $n(x)$  and holes  $p(x)$  in the device. In fact,  $n(x)$  is very high and  $p(x)$  extremely low at the cathode and vice versa at the anode. Thus, recombination in vicinity of the contacts is very unlikely and takes predominantly place in the bulk, where both charge carrier densities are sufficiently high. Other possible explanations were given by Koster et al. [111] and Arkhipov et al. [113], who attributed the low  $\zeta$  to the minimum mobil-

ity of both charge carriers or random potential fluctuations in an ambipolar material, respectively.

Temperature-dependent measurements down to 180 K (not shown) yielded good agreement of experimental data and model for P3HT:PC<sub>61</sub>BM, which leads to the conclusion, that bimolecular recombination is still the predominant process. As expected,  $\gamma$  decreased for lower temperature due to decreasing mobility [114]. In contrast, no good agreement of experimental data and model was found for MDMO-PPV:PC<sub>61</sub>BM [114]. This behaviour may indicate that the recombination is no longer Langevin type and the order of recombination is higher than two, which can be attributed to trapping effects [59, 60, 62].

## 7.3 Conclusion

To conclude, we investigated the field-dependence of free charge carrier generation in two well-known material systems by means of temperature-dependent time-delayed collection field measurements. For MDMO-PPV:PC<sub>61</sub>BM we found a strong field-dependence, which became even more prominent at low temperatures. We therefore conclude that free charge carriers are generated via a thermalized CTS, which is in good agreement to photoluminescence measurements exhibiting considerable exciton binding energies up to 200 meV for this system [55, 56]. In contrast, we observed a very weak field-dependence of less than 20% in case of P3HT:PC<sub>61</sub>BM, which was independent of temperature. Hence, the influence of geminate recombination in the generation of free charge carriers is clearly below 20%, as part of the field-dependence can also be attributed to field-dependent charge photogeneration. These findings are also in good agreement to transient absorption measurements [58] and lead to the conclusion that free charge carriers are either generated directly or via an excited, or “hot”, CTS [57].

Furthermore, nongeminate recombination processes were investigated by TDCF measurements with variable delay-times. An iterative fit forward in time was applied in order to extract the Langevin recombination prefactors of both material systems. We found that despite similar mobilities and dielectric constants this prefactor is one order of magnitude smaller in case of P3HT:PC<sub>61</sub>BM. These findings result in a reduction factor  $\zeta$  which is close to unity for MDMO-PPV:PC<sub>61</sub>BM and about 0.02 for P3HT:PC<sub>61</sub>BM. In accordance to previous results [64, 112, 110] we therefore conclude Langevin type recombination for MDMO-PPV:PC<sub>61</sub>BM and a strongly reduced one for P3HT:PC<sub>61</sub>BM. The latter can be explained by the incorrect assumption of spatially constant charge carrier densities for electrons and holes [64] across the whole device.





# Influence of the Bridging Atom on Charge Photogeneration

---

The morphology of the photoactive layer plays an important role in organic BHJ solar cells, as it can directly influence charge carrier generation, transport and recombination, and therefore the device performance [20, 8]. Already slight changes in the chemical structure of the employed materials (e.g. substitution of the bridging atom of the polymer) can result in considerable changes in morphology and device performance. In this chapter, we will therefore compare two almost identical low bandgap polymers, which only differ by the bridging atom in the cyclopentadithiophene. In case of PCPDTBT, a carbon bridging atom results in an amorphous material, while a silicon atom leads to the more crystalline Si-PCPDTBT as shown by Scharber et al. [115]. All results presented here refer to standard BHJ solar cells containing blends of the respective material with the electron acceptor PC<sub>71</sub>BM. As in the previous chapter, the field-dependence of charge photogeneration will be investigated by means of time-delayed collection field measurements. These results will then be set into relation to atomic force microscopy (AFM) measurements and current–voltage characteristics to gain further insights on how the different bridging atoms alter the morphology of the active layer and influence the device efficiency.

## 8.1 Field-Dependent Charge Photogeneration

As explained before (see section 5.3.2), the illumination intensity for TDCF measurements was set low enough to exclude nongeminate recombination losses during field-dependent measurements. It is important to note that it is only possible to exclude nongeminate recombination for voltages below the applied prebias voltage during the preceding illumination-dependent measurements (0 V). In order to investigate the field-dependence of charge photogeneration, collection voltage (-6 V) and delay time (385 ns) were set constant while sweeping the applied prebias voltage. The corresponding data is shown in Figure 8.1 for PCPDTBT:PC<sub>71</sub>BM (left, blend ratio 1:2.7) and Si-PCPDTBT:PC<sub>71</sub>BM (right, blend ratio 1:1.15). The different blend ra-

tios were chosen to obtain the best performing solar cells for each material system. For the sake of comparability, the data was normalized to  $Q_{tot}(-5 \text{ V})$ , even though the saturation value had not been reached in case of PCPDTBT:PC<sub>71</sub>BM. Thus, the field-dependence observed in this case is still underestimated. In principle, both materials showed a field-dependence of  $Q_{pre}$  (red triangles) and  $Q_{col}$  (green triangles) which is qualitatively similar to that of P3HT:PC<sub>61</sub>BM (see previous chapter).

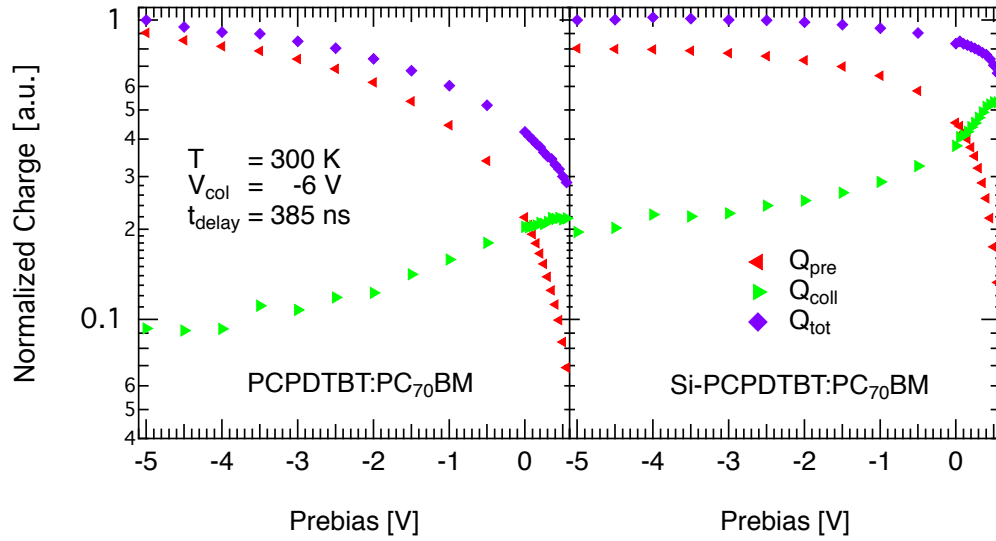


Figure 8.1: The field-dependence of PCPDTBT:PC<sub>71</sub>BM (left) is much more pronounced than in Si-PCPDTBT:PC<sub>71</sub>BM (right), indicating two different dominating scenarios of free charge carrier generation: Strong field-dependence due to a predominant pathway via a thermalized CTS (left) or highly efficient free charge carrier generation either directly or via a “hot” CTS (right). The data were normalized to  $Q_{tot}(-5 \text{ V})$ .

As expected, less charge carriers were extracted during the delay time with decreasing internal field, resulting in an decreasing  $Q_{pre}$ . In contrast to MDMO-PPV:PC<sub>61</sub>BM, the additional charges remaining in the device were not completely lost due to geminate recombination. A considerable part of them could still be extracted by the collection field, resulting in an increasing  $Q_{col}$  for low internal fields (i.e. prebias voltages approaching  $V_{OC}$ ). However,  $Q_{col}$  does not increase as much as  $Q_{pre}$  decreases, resulting in a considerable overall field-dependence of  $Q_{tot}$  (purple diamonds) for both blends. Even the better performing Si-PCPDTBT:PC<sub>71</sub>BM shows a stronger field-dependence than P3HT:PC<sub>61</sub>BM, where the influence of geminate recombination was estimated to be clearly below 20%. In case of Si-PCPDTBT:PC<sub>71</sub>BM,  $Q_{tot}$

decreased by 35% between its saturation value at -5 V and  $V_{OC}$ , which means that at least 65% of the free charge carriers were either generated directly or via a “hot” CTS. Both routes provide a fast and highly efficient generation of free charge carriers but cannot be distinguished in TDCF measurements. In PCPDTBT:PC<sub>71</sub>BM,  $Q_{tot}$  decreased below 30% of its (not saturated) maximum value at -5 V, indicating that the less efficient scenario of free charge carrier generation via a thermalized CTS is the dominating process with a fraction clearly exceeding 70%. These results are in good agreement to previously published photoluminescence measurements by Morana et al. [116], who observed CTS emission above 900 nm for PCPDTBT:PC<sub>71</sub>BM, which was almost completely quenched or rendered inactive in the Si-PCPDTBT blend. We can therefore conclude, that the substitution of the carbon bridging atom in PCPDTBT by a silicon atom improves the charge photogeneration by clearly increasing the amount of free charge carriers generated via the more efficient routes of either direct generation or via a “hot” CTS. This is one explanation for the different power conversion efficiencies of Si-PCPDTBT:PC<sub>71</sub>BM (4.3%) and PCPDTBT:PC<sub>71</sub>BM (2.7%), which were observed despite comparable HOMO (-5.3 eV) and LUMO (-3.6 eV) levels of both systems [115].

It is also interesting to note that Si-PCPDTBT:PC<sub>71</sub>BM exhibits strongly reduced Langevin recombination ( $\zeta \approx 0.005$ , determined by transient photovoltage spectroscopy), while PCPDTBT:PC<sub>71</sub>BM features a reduction factor of about one and indicates Langevin type recombination [115]. As in the previous chapter, a predominantly fast and direct generation of free charge carriers (Si-PCPDTBT:PC<sub>71</sub>BM) is again connected to strongly reduced Langevin recombination. In contrast, the domination of the less efficient, field-dependent scenario of free charge carrier generation via a thermalized CTS is related to Langevin type recombination.

## 8.2 Morphological Aspects

So far, our investigations lead to the conclusion that different dominating pathways of free charge carrier generation are responsible for the differences in performance of the two almost identical materials. This section will therefore focus on the influence of the bridging atom on the active layer morphology and relate these findings to the preceding TDCF measurements. Previous grazing incidence X-ray measurements showed that the substitution of the carbon bridging atom by a silicon atom results in a stronger stacking of the polymer chains and thus a more crystalline phase, in contrast to the more amorphous PCPDTBT. This is also valid when both materials are blended with PC<sub>71</sub>BM [115]. To further investigate the influence of the

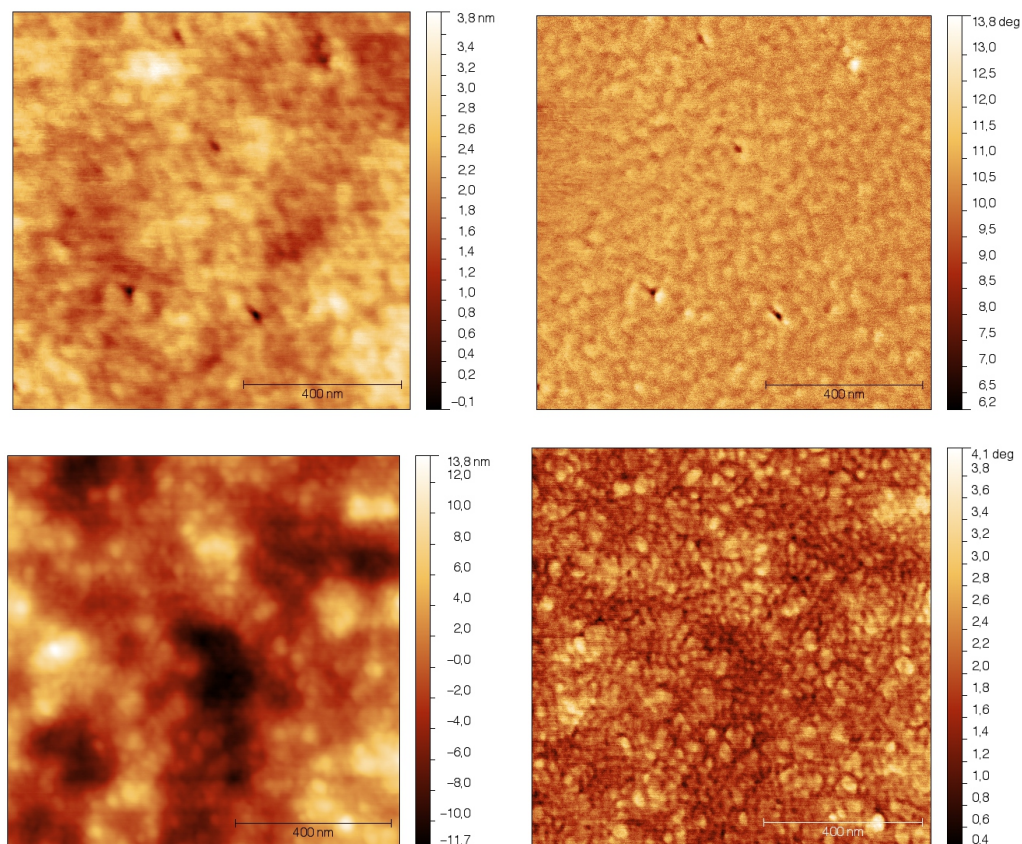


Figure 8.2: Height (left) and phase (right) diagrams of PCPDTBT:PC<sub>71</sub>BM (top) and Si-PCPDTBT:PC<sub>71</sub>BM (bottom). Replacing the carbon bridging atom by silicon results in a rougher surface and a more defined phase separation, which enhances the amount of free charge carriers generated either directly or via a hot CTS.

bridging atom, we performed AFM measurements for both blends, which are shown in Figure 8.2. The top row contains height profile (left) and phase (right) of PCPDTBT:PC<sub>71</sub>BM and the bottom row the corresponding data for Si-PCPDTBT:PC<sub>71</sub>BM. Concerning the height profiles, PCPDTBT:PC<sub>71</sub>BM features a very smooth surface with maximum height differences of only 4 nm, which coincides with an amorphous, well intermixed blend. In contrast, a considerably rougher surface was found for Si-PCPDTBT:PC<sub>71</sub>BM with height differences up to 26 nm, indicating a stronger separation of polymer and fullerene phase and thus the formation of larger domains. This interpretation is supported by the phase diagrams of both blends, showing a more defined phase separation in case of Si-PCPDTBT:PC<sub>71</sub>BM. These findings agree well with the higher crystallinity of Si-PCPDTBT:PC<sub>71</sub>BM found by the grazing

incidence X-ray measurements mentioned before.

In combination with the field-dependent TDCF measurements shown before, these observations indicate that a stronger spatial separation of the polymer and fullerene phase in Si-PCPDTBT:PC<sub>71</sub>BM is connected to a much weaker field-dependence of charge photogeneration than in the amorphous, well intermixed PCPDTBT:PC<sub>71</sub>BM. Hence, larger domains yield a more efficient dissociation of the excitons, which is in good agreement to kinetic Monte Carlo simulations: Deibel et al. [102] showed that long conjugation lengths result in higher and less field-dependent polaron pair dissociation yields, as the delocalization of the hole on the polymer phase increases. The binding energy of the polaron pair is thereby reduced and thus the probability for geminate recombination. In addition, larger domains mean more percolated pathways for charge transport, which coincides with the strongly reduced Langevin recombination observed in Si-PCPDTBT:PC<sub>71</sub>BM [115] as well as in P3HT:PC<sub>61</sub>BM. On the other hand, if polymer and fullerene phase are well intermixed, the probability for nongeminate recombination is high, as there are more interfaces where the charge carriers can recombine. Similar observations have been reported by Albrecht et al. [117], who found a lower field-dependence of free charge carrier generation in PCPDTBT:PC<sub>71</sub>BM when using diiodooctane as solvent additive due to a better phase separation.

### 8.3 Influence on the Current–Voltage Characteristics

The typical current–voltage curves of PCPDTBT:PC<sub>71</sub>BM and Si-PCPDTBT:PC<sub>71</sub>BM under illumination equal to one sun are shown in Figure 8.3 (left axis, lines with open symbols) and the corresponding device characteristics can be found in table 8.1. As the absorption spectra of both blends are rather similar [115], this effect cannot explain the clear difference in the device efficiency. In addition, similar HOMO and LUMO levels of both materials [115] result in similar open circuit voltages, which are slightly lower for the better performing Si-PCPDTBT:PC<sub>71</sub>BM devices. Thus, the differences in device performance mainly arise from the different short circuit current densities and fill factors. Altogether, these findings indicate that the generation of free charge carriers and their transport to the electrodes are crucial to explain the different power conversion efficiencies. An explanation for the much higher short circuit current in Si-PCPDTBT:PC<sub>71</sub>BM is the improved phase separation (see previous section), yielding larger domains and better pathways for charge transport and thus reduced losses due to nongeminate recombination. As shown before, the better phase

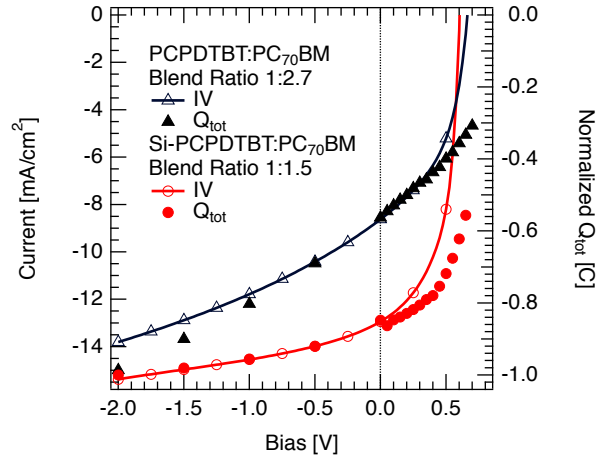


Figure 8.3: Left axis: Current–voltage characteristics of both material systems under one sun (lines with open symbols). The Si-PCPDTBT:PC<sub>71</sub>BM sample features clearly higher fill factor and short circuit current and thus power conversion efficiency. Right axis: Total amount of extracted charge carriers ( $Q_{tot}$ ) from TDCF measurements (solid symbols) normalized to -1 at -2 V.

separation coincides with an improved, less field-dependent free charge carrier generation in Si-PCPDTBT:PC<sub>71</sub>BM, which also contributes to a higher short circuit current. In order to explain the differences in the fill factors, the field-dependence of the charge photogeneration has to be taken into account. We therefore added  $Q_{tot}$  from field-dependent TDCF measurements to Figure 8.3 (solid symbols, right axis) and normalized the data for better comparability to -1 at an applied prebias of -2 V. In case of Si-PCPDTBT:PC<sub>71</sub>BM (red), the increasing current density in reverse direction corresponds to the weak field-dependence of  $Q_{tot}$ , which means the field-dependence of charge photogeneration. Close to open circuit conditions, the field-dependence of  $Q_{tot}$  increases drastically, which corresponds to an increasing influence of geminate recombination, as still 35% of the free charge carriers are generated via the less efficient scenario of a thermalized CTS (see previous section). This behavior results in a reduced fill factor (56%) in comparison to P3HT:PC<sub>61</sub>BM, where almost no field-dependence of  $Q_{tot}$  close to open circuit conditions was observed, which coincides with a high fill factor of about 70% (see chapter 7) and a good spatial separation of the polymer and fullerene phase. In case of carbon bridged PCPDTBT:PC<sub>71</sub>BM, a strong influence of geminate recombination over the whole voltage range is reflected by a strongly increasing current density in reverse direction and results in an even lower fill factor of 48%.

Table 8.1: Solar cell characteristics under illumination corresponding to one sun of two typical devices containing PCPDTBT:PC<sub>71</sub>BM and Si-PCPDTBT:PC<sub>71</sub>BM.

Blend	$V_{OC}$ [V]	$J_{SC}$ [ $\frac{mA}{cm^2}$ ]	FF [%]	$\eta$ [%]
PCPDTBT:PC <sub>71</sub> BM	0.65	8.5	48	2.7
Si-PCPDTBT:PC <sub>71</sub> BM	0.60	13.0	56	4.3

## 8.4 Conclusion

In this chapter, we compared two PCPDTBT derivatives, which only differed by the bridging atom (carbon or silicon) in the cyclopentadithiophene. Nevertheless, they revealed clear differences in the solar cell performance when blended with PC<sub>71</sub>BM. In case of PCPDTBT:PC<sub>71</sub>BM (carbon bridging atom) a strong field-dependence of the free charge carrier generation was observed, indicating a predominant scenario of charge photogeneration via a thermalized CTS, leading to a rather low fill factor and short circuit current. In addition, AFM measurements revealed a fine intermixing of the polymer and fullerene phase, which results in a strong influence of nongeminate recombination. The latter prevents an efficient transport of the free charge carriers to their respective electrode and therefore reduces the short circuit current. These results are in good agreement to previous kinetic Monte Carlo simulations by Deibel et al. [102], who showed that short delocalization lengths of the hole on the polymer phase result in low polaron pair dissociation yields. In contrast, the substitution of the carbon bridging atom by a silicon atom resulted in a lower field-dependence of charge photogeneration, favoring the more efficient scenarios of either direct generation of free charge carriers or via an excited CTS. Both would result in a higher short circuit current and fill factor. Furthermore, AFM measurements showed a stronger phase separation in the blend, resulting in more percolated pathways and therefore less nongeminate recombination losses which reduce the short circuit current. These observations also agree to the kinetic Monte Carlo simulations mentioned above, as longer delocalization lengths result in higher polaron pair dissociation yields. In combination, our findings can explain the improved current–voltage characteristics of the Si-PCPDTBT:PC<sub>71</sub>BM compared to the PCPDTBT:PC<sub>71</sub>BM blend, which are mainly due to a higher short circuit current and fill factor.





# Validity of Mott–Schottky Analysis in Organic BHJ Solar Cells

---

The built-in potential is defined as the difference of the electrode work functions [118] and is a very important key parameter of solar cells. It determines the internal electric field and can therefore influence polaron pair separation and charge transport inside the device. In addition,  $V_{Bi}$  is an upper limit for the open circuit voltage [34] and thus has a strong, direct influence on the device efficiency. A powerful and well established tool to obtain the built-in potential of a device is the Mott–Schottky (MS) analysis, which is based on impedance measurements (see section 5.3.3). In this chapter, the validity of the direct transfer of Mott–Schottky analysis from inorganic systems to organic BHJ solar cells will be discussed. Major parts of the work presented here are published in paper 6 by Mingeback et al. [98]. For all investigations done here, we chose the well known reference system P3HT:PC<sub>61</sub>BM.

## 9.1 Mott–Schottky Analysis

As stated before, Mott–Schottky analysis was derived for metal–semiconductor interfaces [80, 81, 82] and is also valid for abrupt pn-junctions [83]. Both cases describe bilayer systems, which is not true for the organic BHJ solar cells investigated here. In the latter, the photoactive layer consists of a blend of two semiconducting materials and therefore has to be considered as an effective medium. Hence, the samples need to be interpreted as ambipolar devices with two slightly non-ohmic contacts, which cannot be explained by MS theory. This can be seen as a first hint that a direct transfer of Mott–Schottky analysis to typical organic devices is not entirely correct. Therefore, we will denote the potential obtained from MS analysis of our devices as  $V_{CV}$  in the following.

In order to investigate the validity of Mott–Schottky analysis for organic BHJ solar cells, we performed capacitance–voltage (CV) measurements as

described in section 5.3.3. The resulting experimental data and the Mott–Schottky plot for a P3HT:PC<sub>61</sub>BM device with an active layer thickness of 250 nm are shown in Figure 9.1. First of all, the left graph displays the area normalized capacitance versus the applied voltage (red open diamonds). A general interpretation of the data was given by Bisquert et al. [84], who distinguished three major capacitance domains with respect to the built-in potential, as highlighted in the graph. At sufficiently high reverse bias ( $V \ll V_{Bi}$ ), the active layer is totally depleted, and hence the resulting capacitance is independent on the applied dc bias voltage (blue domain). In this case, the device can be treated as a plate capacitor, where the blend acts as dielectric and the resulting capacitance corresponds to the geometrical capacitance ( $C_{geo}$ ) of the device given by Equation 5.20. The red domain ( $V < V_{Bi}$ ) marks the Mott–Schottky region, where the capacitance increases inverse quadratically with the applied voltage. Hence, the MS analysis will focus on this part of the capacitance–voltage curve. If the dc bias is further increased (yellow domain), charge injection starts to influence the device properties and results in a decreasing capacitance. However, using the built-in potential as reference for this interpretation seems not to be appropriate, since it refers to flat energy bands and therefore zero electrical field inside the device. As already explained in section 6.1.1, diffusion-induced band-bending occurs in organic BHJ solar cells in the vicinity of metal contacts [95] and results in a finite electric field throughout the whole device (see Figure 6.2). Hence, a case of completely flat energy bands does not exist (at  $T > 0 K$ ), which is another indication, that MS analysis cannot exactly lead to the built-in potential ( $V_{CV} \neq V_{Bi}$ ).

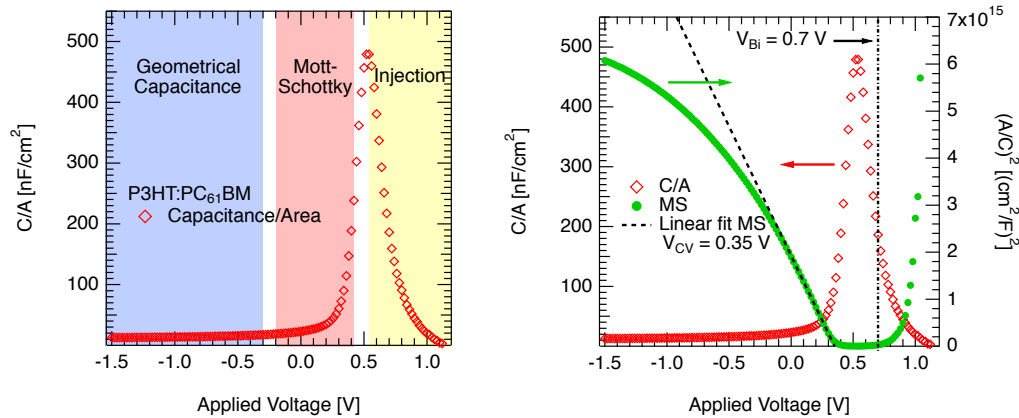


Figure 9.1: Capacitance–voltage signal of a P3HT:PC<sub>61</sub>BM BHJ solar cell (red open diamonds). Left: The blue region corresponds to the geometrical capacitance, the red to the MS region, and the yellow one denotes beginning charge injection due to high forward bias. Right: Corresponding MS plot (green circles) and linear fit for MS analysis (black dashed lines).

The right hand graph in Figure 9.1 displays in addition to the capacitance–voltage data the MS plot (green circles) as well as the linear fit to the MS domain (black dashed line). The intercept of the linear fit with the abscissa yields  $V_{CV} = 0.35 \text{ V}$ , which is well below the built-in potential ( $V_{Bi} = 0.7 \text{ V}$ ), obtained from temperature-dependent measurements of the open circuit voltage. The latter will be explained in more detail later on in this chapter. The values deduced here from Mott–Schottky analysis are similar to those presented by other groups. For example, Garcia-Belmonte et al. found a Mott–Schottky potential of  $0.43 \text{ V}$  for a P3HT:PC<sub>61</sub>BM device with an active layer thickness of  $200 \text{ nm}$ , applying Al as top contact [85]. In addition to  $V_{CV}$ , the slope of the linear fit to the MS plot gives the acceptor doping density in the active layer, which yields reasonable values  $\sim 10^{16} \text{ cm}^{-3}$  that are in good agreement to literature [84, 87]. Thus, these experimental results agree well with the considerations mentioned above and further support the assumption of  $V_{CV}$  not being equal to the built-in potential.

Moreover, a thickness-dependence of the MS potential can be observed. The active layer thickness  $L$  was varied in the range from  $65$  to  $250 \text{ nm}$  and determined with a Veeco Dektak 150 profilometer. To verify these values, the geometric capacitance of the devices was determined by CV-measurements at high reverse bias, in order to calculate  $L$  from equation 5.20. Here, we used a relative permittivity of  $\epsilon_s = 3.3$  for a 1:1 blend ratio of P3HT:PC<sub>61</sub>BM, which was derived experimentally (see section 5.3.3) and is similar to literature values from Koster et al. ( $\epsilon_s = 3.4$ ) [89]. The resulting active layer thicknesses were in good agreement with the profilometric measurements mentioned before. As it can be seen in Figure 9.2 (green dots), the variation of the active layer thickness resulted in an exponential increase of  $V_{CV}$  with decreasing  $L$ . To highlight the strong thickness-dependence, the dotted green line is added as a guide to the eyes and shows an exponential fit to  $V_{CV}$ . In case of thick samples ( $250 \text{ nm}$  active layer)  $V_{CV}$  was as low as  $0.35 \text{ V}$ , reaching up to  $0.56 \text{ V}$  for very thin samples ( $65 \text{ nm}$  active layer). This behavior cannot be explained by classical MS analysis, that does not predict any thickness-dependence at all (see equation 5.19). Hence, this is another experimental indication that MS analysis does not result in the built-in potential.

As already mentioned above,  $V_{Bi}$  — in contrast to  $V_{CV}$  — does not correspond to flat energy bands (zero electric field conditions) in organic BHJ solar cells. Instead, a case of flat energy bands in the bulk of the device (denoted as QFB, see section 6.1.1), which is well below  $V_{Bi}$ , can be reached. The corresponding voltage  $V_{POS} \approx 0.56 \text{ V}$ , determined by pulsed photocurrent measurements (see section 6.1), does not show any unexpected dependency on the active layer thickness (Figure 9.2, violet squares). Hence, for thin samples with active layer thicknesses below  $100 \text{ nm}$ , the MS potential can be close

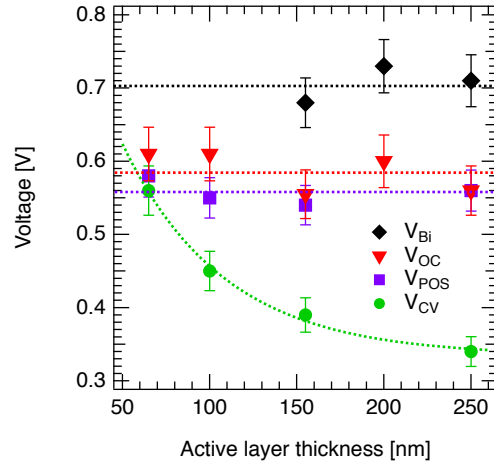


Figure 9.2:  $V_{Bi}$  (black diamonds, determined as shown in Fig. 9.3),  $V_{OC}$  (red triangles),  $V_{POS}$  (purple squares) and  $V_{CV}$  (green circles) for P3HT:PC<sub>61</sub>BM bulk heterojunction solar cells with varying active layer thickness. In contrast to  $V_{OC}$ ,  $V_{POS}$  and  $V_{Bi}$ ,  $V_{CV}$  shows a clear dependency on the active layer thickness (increases with decreasing thickness) and approaches  $V_{POS}$ . The dotted lines are guides to the eyes and mark the mean values of the corresponding potentials respectively an exponential fit to  $V_{CV}$ .

or even equal to  $V_{POS}$ , and therefore quasi-flat band conditions. However, with increasing active layer thickness, the difference of both values increases, reaching more than 0.15 V for thick samples above 150 nm. Due to these findings, the QFB (as proposed in chapter 3) seems to be a more reliable measure for flat band conditions in organic BHJ solar cells, while  $V_{CV}$  yields neither built-in potential nor the case of quasi-flat bands.

In addition, Figure 9.2 displays the open circuit voltage (red triangles) and the built-in potential (black diamonds), which are both independent on the active layer thickness. The latter was determined by temperature-dependent measurements of  $V_{OC}$ , as shown in Figure 9.3 (red triangles). This method was introduced by Rauh et al. [34] and will be explained here briefly. In general, the open circuit voltages can be separated into two temperature regions. For high temperatures (above 160 K),  $V_{OC}$  increases linearly with decreasing temperature, until a constant value is reached at low temperatures (below 160 K). In this case the energetic barriers at the contacts dominate the behaviour of the device. It has previously been shown experimentally and by simulations that the constant value for low temperatures yields  $V_{Bi}$ , while a linear fit to the high temperature region leads to the effective band gap ( $E_g$ ), when extrapolated to zero Kelvin. The resulting built-in potentials reach values between 0.67 and 0.73 V that are not dependent on the active layer

thickness (see Fig. 9.2, black diamonds). They clearly exceed the thickness-dependent  $V_{CV}$  from MS analysis (0.35 to 0.56 V, green dots) and therefore support the idea that MS analysis does not lead to the built-in voltage. Furthermore, temperature-dependent CV measurements, as shown in Figure 9.3 (green dots), result in an exponentially increasing  $V_{CV}$  with decreasing temperature and without any connection to  $V_{Bi}$ .

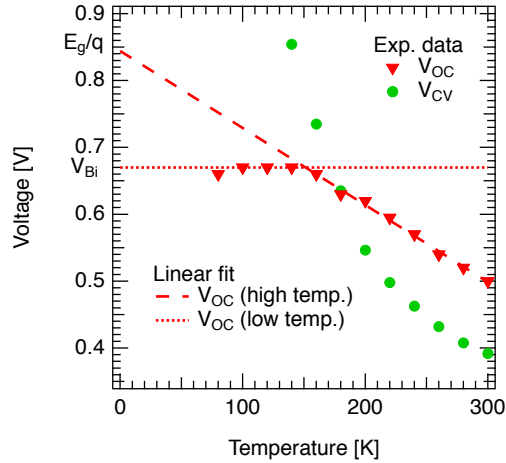


Figure 9.3: Temperature-dependent measurements of  $V_{CV}$  (green dots) and the open circuit voltage (red triangles). An extrapolation of the low temperature region of  $V_{OC}$  (dotted red line) leads to the built-in potential, while a linear extrapolation of the high temperature region (dashed red line) leads to the effective band gap  $E_g$  (at  $T = 0$  K) [34].  $V_{CV}$  increases exponentially with decreasing temperature and shows no connection to the built-in potential.

## 9.2 Conclusion

In this chapter the validity of Mott–Schottky analysis of organic BHJ solar cells was discussed. Due to the findings presented here, a direct transfer of MS analysis from inorganic systems to organic BHJ solar cells seems not to be appropriate. Thus, the MS potential ( $V_{CV}$ ) does not correspond to the built-in potential, as it is the case in inorganic systems. First of all, MS theory was derived for a metal–semiconductor interface (or an abrupt pn-junction), which are both unipolar bilayer system. This is not entirely correct for organic BHJ solar cells, where the photoactive blend has to be treated as an effective medium, thus an ambipolar device. Experimentally, a clear discrepancy between  $V_{CV}$  (0.35 to 0.56 V) and  $V_{Bi}$  (0.7 V), determined by temperature-dependent measurements of the open circuit voltage,

was observed. Additionally,  $V_{CV}$  showed — in contrast to  $V_{Bi}$  and  $V_{POS}$  — an unexpected dependency on the active layer thickness, which cannot be explained by classical MS theory. Temperature-dependent measurements of  $V_{CV}$  did not show any connection to  $V_{Bi}$  as well. Instead, the case of quasi-flat bands, determined by pulsed photocurrent measurements is independent on the active layer thickness and seems to be more appropriate to determine flat band conditions in an organic BHJ solar cell.

# Printed Paper Photovoltaics - 3PV

---

In the following chapter I will mainly present the results, obtained in the framework of the MOPS (Massengedruckte Organische Papier-Solarzellen) project, funded by the German Federal Ministry of Education and Research (project ID 13N9867). In collaboration with our project partners, the first completely roll-to-roll printed organic solar cells on a paper substrate were developed, characterized and compared to macroscopic device simulations. The corresponding results are published in paper 5 by Hübler et al. [119].

## 10.1 Printing Organic Photovoltaics on Paper

As already pointed out in the introduction, solar energy conversion is a fast growing part of the renewable energies sector. Nevertheless its contribution to the energy market is rather low (e.g. 3% in Germany) [3], which is mainly due to the high material and production costs for solar modules. Hence, besides increasing the device efficiency and lifetime, it is crucial to drastically reduce the production costs. A promising approach are thin film technologies which reduce the material consumption. Here, especially organic photovoltaics have the potential to provide low-cost photovoltaic modules, since they allow for mass production techniques as roll-to-roll (R2R) printing. Further advantages of R2R printing are its high production output and the possibility to use cheap, flexible substrates as plastic foils or paper. A low substrate price is essential, as it accounts for 25 to 60% of current solar modules [120, 121]. From this point of view, paper is by far the best substrate material, as its price is about 1000 times lower than normal glass [120, 121, 122] and still 100 times lower than standard plastic foils [122, 123]. Using paper as a substrate for printing organic solar cells is not only based on the idea of employing an inexpensive, flexible substrate which is also compatible with well-established printing processes. In fact, this new approach also provides the opportunity to realize environmentally and economically-friendly devices, which could be recycled together with food packages [119]. Recently, Barr et al. [122] presented organic photovoltaics on as-purchased paper substrates by applying vacuum



deposition processes with a rather low production output in comparison to R2R printing. Nevertheless, the printing technique was up to now limited to plastic foils due to the high surface roughness, porosity and poor wettability of the paper substrates [123, 124], making processing difficult. Its worth mentioning that R2R printing on plastic foils often involved expensive ITO or Ag electrodes, which is counterproductive in reducing production costs. But there were also approaches to replace the ITO contact [125], which resulted in power conversion efficiencies of up to 2% on plastic substrates [126]. For the interested reader, a review on roll-to-roll printing of polymer solar cells on plastic substrates was recently given by S ndergaard et al. [127]. A general review on electronic devices on paper substrates was given by Tobj rk et al. [123].

## 10.2 Results and Discussion

### Printed Paper Photovoltaics (3PV) Cell Architecture

In contrast to the standard organic BHJ solar cells discussed in the previous chapters, the R2R printed samples feature an inverted cell architecture. Due to the nontransparent paper substrate the samples need to be illuminated via the transparent top electrode. In order to keep the production costs low, the device layout had to be as simple as possible with a minimum of required printing steps, and expensive electrodes such as ITO or Ag should be avoided, too. The resulting device architecture is depicted in Figure 10.1 (right in the bottom). As substrate a glossy paper was used, on which the Zn cathode was applied by cold-foil transfer printing from a polypropylene foil. Since all production took place under ambient conditions, the metallic Zn cathode was oxidized and hence covered by a thin ZnO layer, which acts as a hole-blocking layer, making the electrode selective. Furthermore, the conduction band minimum of ZnO (4.4 eV) is close to the LUMO of PC<sub>61</sub>BM, enabling an efficient electron transfer from PC<sub>61</sub>BM to ZnO [128], without losing much excess energy. Other advantages of the ZnO interlayer are its qualities as optical spacer and oxygen barrier layer [128]. Thereafter, the photoactive layer consisting of P3HT:PC<sub>61</sub>BM was deposited by gravure printing and finally, the PEDOT:PSS anode was applied by a flexographic printing step as depicted in Figure 10.1. The sample preparation by R2R printing was done by the Institute for Print and Media Technology at the Chemnitz University of Technology (pmTUC) and a more detailed description of the specific printing steps can be found in our publication [119].

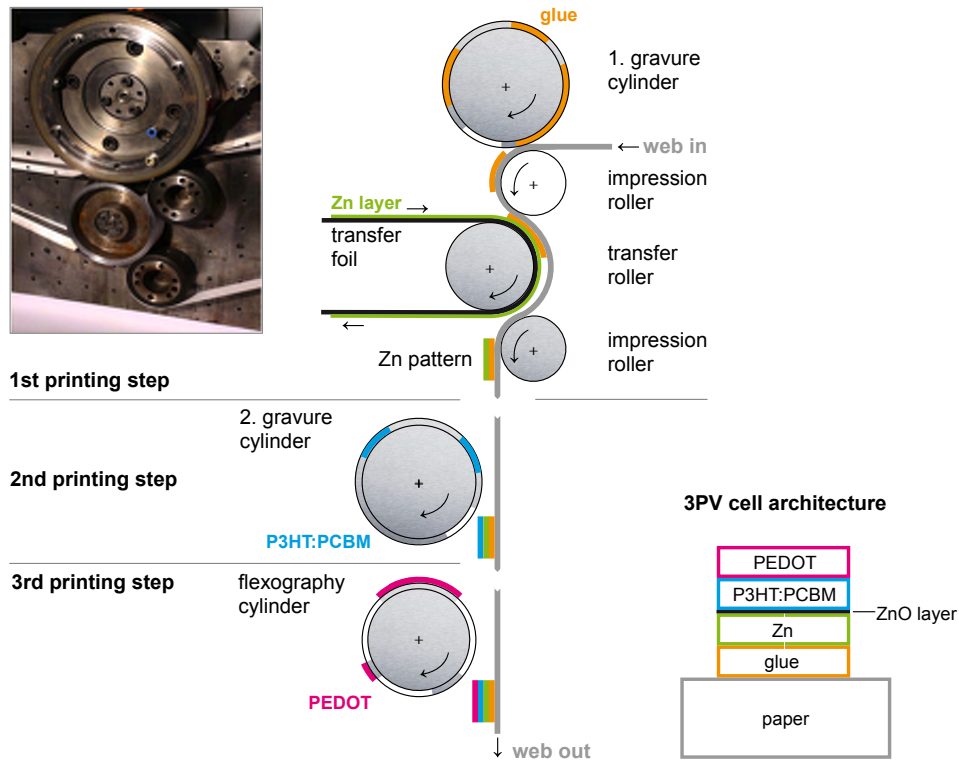


Figure 10.1: Printing processes and layer architecture: 1. Printing step: Gravure assisted transfer printing of the Zn layer from polypropylene foil to paper substrate with subsequent oxidation of the Zn cathode due to ambient conditions (not shown). The photograph shows a lab printing unit. 2. Step: Gravure printing of the photoactive P3HT:PC<sub>61</sub>BM layer on top of the oxidized zinc layer. 3. Step: Flexographic printing of PEDOT:PSS as transparent anode on top of the printed photoactive layer. Right in the bottom: layer architecture of the final 3PV cell. (from [119])

## Device Characterization

As mentioned before, a major obstacle of using paper as a substrate for thin film technologies is its high surface roughness and porosity [123]. This problem could be circumvented by the application of the Zn cathode. The several  $\mu\text{m}$  thick layer of glue is necessary to attach the Zn layer onto the paper substrate and compensates for the rough surface of the paper. For further processing the roughness of the oxidized Zn cathode, given by the polypropylene transfer foil, is the determining factor. Thus, the cathode surface was investigated by means of scanning electron microscopy (SEM) with a Carl Zeiss gemini ULTRApus and by 3D scanning microscopy with a VK 9700 Keyence (pmTUC). Figure 10.2 (a) shows the SEM image of the dense ZnO

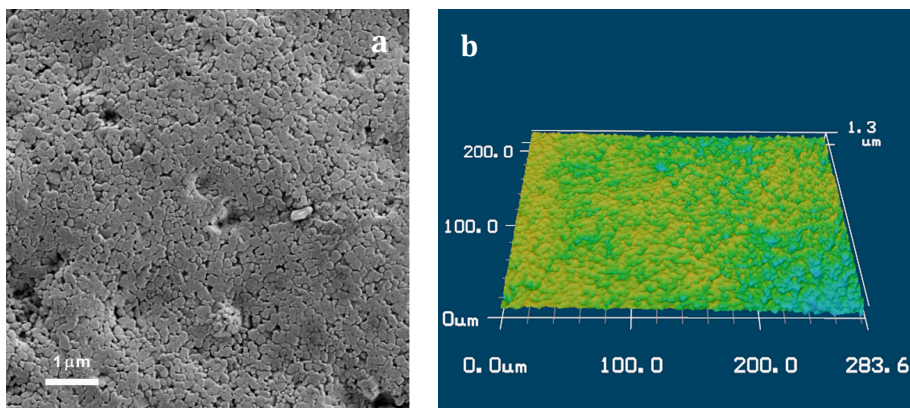


Figure 10.2: Surface of an oxidized zinc layer printed on a paper substrate: Scanning electron microscope (SEM) image (left) and surface morphology by 3D laser scanning microscope (right). (from [119])

surface with its of the hexagonal crystal structure and crystal sizes of about 100 to 200 nm. The thickness of the ZnO layer could be controlled by the exposure time to ambient conditions and the temperature of the Zn cathode [129]. 3D scanning microscopy (see Figure 10.2 b) resulted in an average surface roughness of  $R_a \approx 80$  nm, which is clearly smoother in comparison to standard, as-purchased paper with  $R_a \sim 1.5 \mu\text{m}$  [130]. Thus, the application of the photoactive layer is now possible without provoking short circuits between both electrodes.

A cross-sectional SEM view of the completely R2R printed device is shown in Figure 10.3. The left side (a) shows the whole device, including paper substrate, while the right side (b) depicts a magnification of the printed layers. Except for the thin ZnO interlayer on top of the Zn cathode, all other layers are clearly distinguishable. The corresponding layer thicknesses can be roughly estimated to about  $1 \mu\text{m}$  for Zn/ZnO, at least 120 nm for the photoactive layer and 150 - 200 nm for the PEDOT:PSS anode. Nevertheless, the existence of the ZnO layer was proven by energy dispersive X-ray spectroscopy (EDX) of the cathode surface (not shown).

A major obstacle for current–voltage measurements was the nontransparent paper substrate, which did not allow for sample illumination with our standard solar simulator (LOT Oriel) setup, integrated into a glovebox system. Hence, we used a setup including a 150 W Xe arc lamp (LOT Oriel) and performed comparative measurements with the solar simulator. The latter was calibrated by measurements of the external quantum efficiency (EQE) of non-inverted P3HT:PC<sub>61</sub>BM solar cells on glass substrates to simulate standard testing conditions (STC) at  $100 \frac{\text{mW}}{\text{cm}^2}$  [35]. For the comparative measurements,

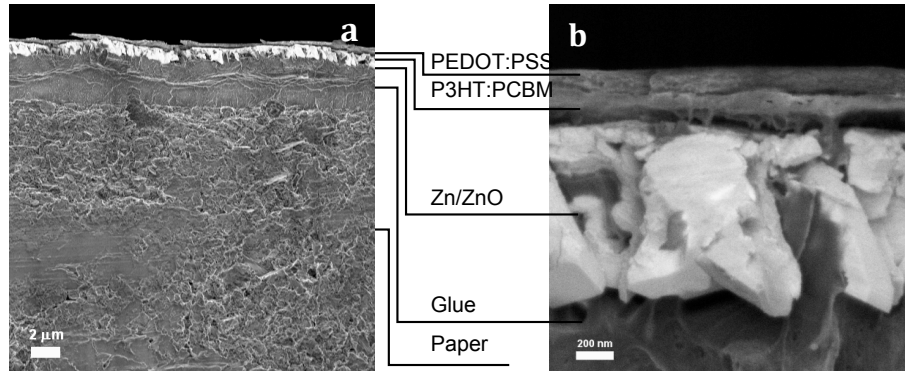


Figure 10.3: SEM image of the 3PV device cross-section and layer architecture (paper/glue/Zn/ZnO/P3HT:PC<sub>61</sub>BM/PEDOT:PSS). Left: Whole device including paper substrate. Right: Closeup view without substrate. In both images, Zn and ZnO layers are not distinguishable. (from [119])

we used a standard, non-inverted device and a Si-diode (Hamamatsu, S1133) with an optical filter (320 - 730 nm) to obtain a similar absorption range as P3HT:PC<sub>61</sub>BM. In both cases the short circuit current decreased to 60% for the inverted device setup, while open circuit voltage and fill factor remained constant. Assuming a linear dependency of  $I_{SC}$  on the illumination intensity results in an illumination level of  $60 \frac{mW}{cm^2}$  for our inverted device setup, which has to be taken into account for the determination of the device power conversion efficiency (see Equation 2.2). The whole characterization as well as the production of the 3PV devices took place under ambient conditions and did not include any vacuum or inert atmosphere steps, which is crucial for a low-cost mass production of the devices.

The 3PV devices had active areas of  $0.09 \text{ cm}^2$  and reached power conversion efficiencies of 1.3%, despite showing slight S-shape behavior above  $V_{OC}$  under illumination (see Figure 10.4). The open circuit voltage ( $V_{OC} = 0.59 \text{ V}$ ) is slightly higher than in non-inverted devices on ITO covered glass substrates ( $\approx 0.57 \text{ V}$ ). Nevertheless, short circuit current density ( $J_{SC} = 3.6 \text{ mA/cm}^2$ ) and fill factor ( $FF = 37\%$ ) are still clearly below those of the standard devices ( $J_{SC} \approx 9 \text{ mA/cm}^2$ ,  $FF \approx 70\%$ ). Reasons for the lower short circuit current are the not yet fully optimized layer thicknesses, which are harder to control for R2R printing processes than for spin coating on small substrates. Furthermore, the PEDOT:PSS anode is quite thick (150 - 200 nm) in comparison to non-inverted devices ( $\approx 40 \text{ nm}$ ), which results in higher losses due to light absorption and hence short circuit current and efficiency decrease. This points at a major obstacle of R2R printing, which does not yet allow for very thin but also dense layers. Nonetheless, a thinner PEDOT:PSS layer

would not automatically solve this problem, as the conductivity of the layer would decrease. In order to explain the S-shape behavior under illumination, macroscopic device simulations of the current–voltage characteristics were performed. In principle, they were based on a numerical approach of solving a system out of Poisson, continuity, and drift-diffusion equations, assuming a reduced bimolecular recombination ( $\zeta = 0.1$ ) according to Langevin [131]. The layer thicknesses of ZnO, P3HT:PC<sub>61</sub>BM and PEDOT:PSS were set to 100, 100 and 300 nm, respectively, while the Zn layer was assumed to be macroscopically thick. Further important simulation parameters are listed in table 10.1, but for a more detailed description of the macroscopic simulations I refer the interested reader to our paper [119].

Table 10.1: Parameters used in the macroscopic device simulation (current–voltage characteristics) (from [119])

Parameter [unit]	P3HT:PC <sub>61</sub> BM	ZnO
Layer thickness [nm]	100	100
LUMO energy [eV]	-4.3	-4.55
HOMO energy [eV]	-5.4	-7.95
Electron mobility [cm <sup>2</sup> (Vs) <sup>-1</sup> ]	$5 \cdot 10^{-4}$	50
Hole mobility [cm <sup>2</sup> (Vs) <sup>-1</sup> ]	$5 \cdot 10^{-4}$	20
Doping concentration [cm <sup>-3</sup> ]	0	$2 \cdot 10^{17}$
Effective electron density [cm <sup>-3</sup> ]	$7 \cdot 10^{19}$	$4 \cdot 10^{18}$
Effective hole density [cm <sup>-3</sup> ]	$7 \cdot 10^{19}$	$9 \cdot 10^{18}$
Permittivity	3.4	10.0

The current–voltage characteristics of a 3PV device in the dark and under illumination as well as the corresponding macroscopic simulation are shown in Figure 10.4 and are in good agreement. In order to be able to describe the S-shape behavior, additional trap-assisted recombination processes had to be taken into account, which were based on a model by Shockley, Reed and Hall [132]. The recombination processes were set to occur with an increasing rate towards the interface of the photoactive blend and the ZnO layer. The monoenergetic traps which acted as recombination centers for the electrons, were located between the HOMO and LUMO of the photoactive blend and their number increased exponentially while approaching the ZnO layer. Hence, the S-shape above  $V_{OC}$  as observed here can be attributed to the PCBM/ZnO interface. A detailed discussion of different kinds of S-shapes in organic BHJ

solar cells was presented by Wagenpfahl et al. [131].

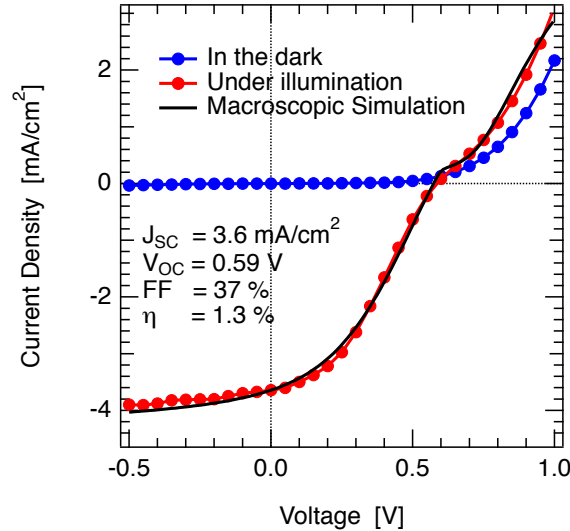


Figure 10.4: Current–voltage characteristics of a 3PV device under ambient conditions with an illumination intensity of  $60 \frac{\text{mW}}{\text{cm}^2}$  and an active area of  $0.09 \text{ cm}^2$ . The illuminated curve was fitted by a macroscopic device simulation with the parameters given in table 10.1.

## 10.3 Conclusion

In this chapter, the first completely roll-to-roll printed organic BHJ solar cells on paper substrate were presented, which are also free from expensive ITO or Ag electrodes. Instead, a naturally oxidized Zn film and a highly conductive, transparent PEDOT:PSS layer were applied as cathode and anode, respectively. Furthermore, all processing took place under ambient conditions, applying only three standard R2R printing steps, keeping device processing as simple as possible. The device architecture (paper/glue/Zn/ZnO/P3HT:PC<sub>61</sub>BM/PEDOT:PSS) was investigated by means of SEM and 3D scanning microscopy, revealing a low surface roughness of the Zn/ZnO cathode ( $R_a = 80 \text{ nm}$ ) despite the high surface roughness of the paper substrate ( $R_a = 1.5 \mu\text{m}$ ). Overcoming of this obstacles was an important step in achieving power conversion efficiencies of 1.3% under an illumination level of  $60 \text{ mW/cm}^2$  without any further optimization of material properties, layer thicknesses and process parameters. Under illumination the current–voltage characteristics of the 3PV devices featured a S-shape behavior above the open circuit voltage, which could be attributed to the PCBM/ZnO

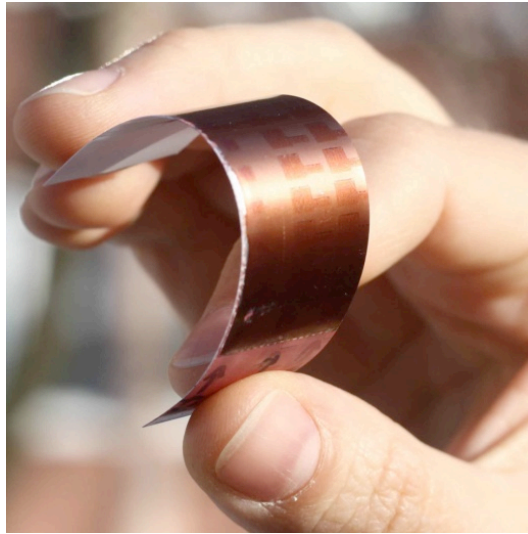


Figure 10.5: Photograph of completely roll-to-roll printed 3PV devices with photoactive areas of  $0.09 \text{ cm}^2$ . (from pmTUC)

interface by means of macroscopic device simulations. To conclude, our work can be seen as a first proof of concept for printed paper photovoltaics (3PV), leading the way to a low-cost mass production of economically-friendly solar modules, which can easily be recycled together with food packages. Figure 10.5 shows a photograph of such completely roll-to-roll printed 3PV devices with photoactive areas of  $0.09 \text{ cm}^2$ , applying the layout described above.

## CHAPTER 11

# Conclusion

---

### Conclusion

The main objective of this work was to investigate the photocurrent of organic BHJ solar cells from a macroscopic and a microscopic point of view. The macroscopic photocurrent investigations were done by means of a pulsed measurement technique in order to prevent any undesirable influences due to device heating. P3HT:PC<sub>61</sub>BM was chosen for these studies as an already well-known reference system. In addition, the underlying microscopic processes determining the photocurrent were investigated by time-delayed collection field (TDCF) in two comparative studies.

The pulsed photocurrent measurements of organic BHJ solar cells revealed a point symmetric voltage dependence of the photocurrent with respect to the point of optimal symmetry (POS) at about 0.53 to 0.64 V. Due to diffusion-induced band-bending at the contacts, the POS does not correspond to the built-in potential as proposed by Ooi et al. [71], but is slightly lower. We denote this as the case of quasi-flat energy bands (QFB). As confirmed by macroscopic simulations, the QFB accounts for flat energy bands in the bulk of the device and is able to explain the point symmetry of the photocurrent with respect to the POS.

On closer inspection, two contributions to the photocurrent can be identified. The first one is a voltage-independent offset, which depends on the processing parameters and was attributed to band-bending in the vicinity of the contacts. The second, voltage-dependent contribution was ascribed to the bulk properties of the device and exhibits the point symmetry. Finally, it was shown that the voltage-dependent photocurrent can be described by a combined model of Braun–Onsager (field-dependent polaron pair dissociation) and Sokel–Hughes (charge extraction) theory for a wide range of different devices.

The dynamics of charge carrier generation and recombination were investigated on a microscopic scale by temperature-dependent TDCF measurements. Here, a comparative study with the two well-known reference systems MDMO-PPV:PC<sub>61</sub>BM and P3HT:PC<sub>61</sub>BM was done. In case of MDMO-PPV:PC<sub>61</sub>BM, a strong field-dependence of charge photogeneration was observed, favoring a scenario of free charge carrier generation via a thermalized charge transfer state (CTS). This effect was even more pronounced at low tem-



peratures and is in good agreement to the considerable exciton binding energy of up to 200 meV, as determined by photoluminescence measurements [55]. In contrast, P3HT:PC<sub>61</sub>BM exhibited — independent on the temperature — a very weak field-dependence below 20%, indicating that more than 80% of the free charge carriers were generated either directly or via an excited, “hot” CTS. Investigations of the nongeminate recombination dynamics revealed Langevin type recombination in case of MDMO-PPV:PC<sub>61</sub>BM and strongly reduced Langevin recombination for P3HT:PC<sub>61</sub>BM. These findings were in good agreement to the clearly higher short circuit current and fill factor of the better performing P3HT:PC<sub>61</sub>BM devices.

In the second comparative study, two novel low bandgap polymers were investigated, which differed only by the bridging atom in the cyclopentadithiophene, but exhibited clear differences in the current–voltage characteristics. The substitution of the carbon bridging atom in PCPDTBT by a silicon one (Si-PCPDTBT) resulted in a considerably lower field-dependence of charge photogeneration in Si-PCPDTBT:PC<sub>71</sub>BM in comparison to PCPDTBT:PC<sub>71</sub>BM. While for the latter the scenario of free charge carrier generation via a thermalized CTS dominated, more than 65% of the free charges were generated either directly or via an excited CTS in case of Si-PCPDTBT:PC<sub>71</sub>BM. These findings were, again, reflected by a higher fill factor and short circuit current of the latter. Additionally, atomic force microscopy (AFM) measurements revealed an improved spatial phase separation in Si-PCPDTBT:PC<sub>71</sub>BM in contrast to the fine intermixed PCPDTBT:PC<sub>71</sub>BM. Due to the fine intermixing, the influence of nongeminate recombination during charge transport to the electrodes was more pronounced. These results were also in good agreement to kinetic Monte Carlo simulations by Deibel et al. [102], who showed that long delocalization lengths of the hole on the polymer phase result in higher polaron pair dissociation yields.

As the built-in potential is another important factor limiting solar cell performance, its correct determination is essential. In inorganics, Mott–Schottky analysis is an established tool to determine the built-in potential and therefore flat band conditions in the device. However, this work showed that a direct transfer of this method to organic BHJ solar cells, which correspond to a bipolar effective medium, is not appropriate. Thus, several theoretical prerequisites are not met for organic BHJ devices and, additionally, a dependence of the experimentally determined Mott–Schottky potential on the active layer thickness was observed, which also contradicts Mott–Schottky theory. Furthermore, it was already shown in this thesis that the built-in potential did not result in a zero field situation. Hence, we conclude that the case of quasi flat bands is a more reliable measure for flat band conditions in organic BHJ

solar cells.

Finally, the first completely roll-to-roll printed organic BHJ solar cells on a paper substrate were presented. They were realized in cooperation with our project partners from the the Institute for Print and Media Technology at the Chemnitz University of Technology in the framework of the MOPS-project (Massengedruckte Organische Papier-Solarzellen) and reached power conversion efficiencies of up to 1.3%.

## Zusammenfassung

Das Hauptziel dieser Arbeit war die Untersuchung des Photostroms organischer BHJ Solarzellen sowohl aus der makroskopischen als auch der mikroskopischen Sichtweise. Die Untersuchungen des makroskopischen Photostroms wurden mittels einer gepulsten Technik durchgeführt, die unerwünschte Einflüsse durch das Aufheizen der Proben verhindern soll. Die Messungen wurden an P3HT:PC<sub>61</sub>BM durchgeführt, da es sich um ein bereits wohl-bekanntes Referenzsystem handelt. Ergänzend dazu wurden die mikroskopischen, dem Photostrom zugrunde liegenden Prozesse mittels time-delayed collection field (TDCF) Messungen in zwei vergleichenden Studien untersucht.

Die gepulsten Photostrom Messungen organischer Solarzellen wiesen eine punktsymmetrische Spannungsabhängigkeit des Photostroms in Relation zu dem “point of optimal symmetry” (POS) auf, der sich in etwa bei 0.54 bis 0.64 V befindet. Auf Grund der diffusions-induzierten Bandverbiegung an den Kontakten entspricht der POS allerdings nicht wie von Ooi et al. [71] postuliert der Diffusionsspannung (built-in potential). Ihm wird vielmehr ein etwas geringeres Potential, das wir als den Quasi-Flachbandfall (“case of quasi flat bands” — QFB) bezeichnen, zugeordnet. Makroskopische Simulationen haben gezeigt, dass der QFB flachen Energiebändern im Inneren der aktiven Schicht entspricht, und dass er in der Lage ist, die Punktsymmetrie des Photostroms bezüglich des POS zu erklären.

Bei genauerer Betrachtung lassen sich zwei Beiträge zum Photostrom identifizieren. Der erste Beitrag wurde der Bandverbiegung an den Kontakten zugeschrieben und führte zu einem spannungsunabhängigen Offset des Photostroms, der sich durch unterschiedliche Prozessparameter beeinflussen lässt. Der zweite, spannungsabhängige Beitrag konnte dagegen dem Inneren der aktiven Schicht (dem “bulk”) zugeordnet werden und ist für die Punktsymmetrie verantwortlich. Abschließen konnte außerdem gezeigt werden, dass sich der spannungsabhängige Photostrom für eine Vielzahl unterschiedlicher organischer BHJ Solarzellen durch ein kombiniertes Modell — basierend auf den Theorien von Braun–Onsager (feldabhängige Polaronenpaartrennung) und Sokel–Hughes (Ladungsträgerextraktion) — beschreiben lässt.

Die Dynamik der Ladungsträgergeneration und -rekombination wurde auf mikroskopischer Ebene mittels temperaturabhängiger TDCF Messungen untersucht. Dazu wurden im Rahmen dieser Arbeit die beiden wohl-bekanntesten Referenzsystemen MDMO-PPV:PC<sub>61</sub>BM und P3HT:PC<sub>61</sub>BM verwendet. Im Falle des MDMO-PPV:PC<sub>61</sub>BM zeigte sich eine starke Feldabhängigkeit der Ladungsträgergeneration, was für die Erzeugung freier Ladungsträger über das Szenario eines relaxierten Ladungstransferzustands (“charge transfer state” — CTS) spricht. Dieser Effekt zeigte sich bei tiefen Temperaturen

noch deutlicher und stimmt gut mit der erheblichen Exzitonenbindungsenergie von bis zu 200 meV überein, die mit Photolumineszenz Messungen bestimmt wurde [55]. Im Gegensatz dazu konnte für P3HT:PC<sub>61</sub>BM temperaturunabhängig nur eine sehr schwache Feldabhängigkeit von weniger als 20% beobachtet werden, was darauf hindeutet, dass mehr als 80% der freien Ladungsträger entweder direkt oder über einen angeregten (“hot”) CTS generiert werden. Untersuchungen der nichtgeminalen Ladungsträgerrekombinationsprozesse ließen eine Langevin-artige Rekombination im Falle des MDMO-PPV:PC<sub>61</sub>BM und eine deutlich reduzierte Langevin-artige Rekombination in P3HT:PC<sub>61</sub>BM erkennen. Alle diese Ergebnisse lassen sich gut mit dem deutlich höheren Kurzschlussstrom und Füllfaktor der leistungsstärkeren P3HT:PC<sub>61</sub>BM Proben vereinbaren.

In einer zweiten Studie wurden zwei neuartige Polymere mit kleinen Bandlücken verglichen, die sich nur durch das Brückenatom im Cyclopentadithiophen unterscheiden, um die deutlichen Unterschiede in deren Strom-Spannungs Charakteristiken zu erklären. Das Ersetzen des Kohlenstoffbrückenatom (PCPDTBT) durch ein Siliziumatom (Si-PCPDTBT) resultierte in einer deutlich geringeren Feldabhängigkeit der Ladungsträgergeneration in Si-PPDTBT:PC<sub>71</sub>BM im Vergleich zu PCPDTBT:PC<sub>71</sub>BM. Während bei letzterem das Szenario der Generation freier Ladungsträger über einen relaxierten CTS dominierte, wurden im Falle des Si-PCPDTBT:PC<sub>71</sub>BM mehr als 65% der freien Ladungsträger entweder direkt oder über einen angeregten CTS erzeugt. Dies spiegelte sich wie bereits zuvor in dem höheren Kurzschlussstrom und Füllfaktor leistungsfähigeren Si-PCPDTBT:PC<sub>71</sub>BM Solarzellen wieder. Darüber hinaus wurden rasterkraftmikroskopische (AFM) Untersuchungen durchgeführt, die eine verbesserte räumliche Phasenseparation des Si-PCPDTBT:PC<sub>71</sub>BM im Vergleich zu dem feiner durchmischten PCPDTBT:PC<sub>71</sub>BM zeigten. Die feinere Durchmischung führt zu deutlich höheren Verlusten auf Grund von nichtgeminaler Rekombination während des Ladungsträgertransports zu den jeweiligen Elektroden. Diese Resultate stimmen außerdem gut mit kinetischen Monte Carlo Simulationen von Deibel et al. [102] überein, die eine erhöhte Trennungswahrscheinlichkeit der Polaronenpaare durch eine größere Delokalisation des Lochs auf der Polymerphase zeigten.

Da die Diffusionsspannung ein weiterer wichtiger, die Leistung einer Solarzelle limitierender Faktor ist, ist deren korrekte Bestimmung äußerst wichtig. In der Halbleiterphysik hat sich dabei die Mott-Schottky Analyse als verlässliche Methode zur Bestimmung der Diffusionsspannung und damit des Flachbandfalls etabliert. Allerdings wurde im Verlauf dieser Arbeit gezeigt, dass ein direktes Übertragen dieser Methode auf organische BHJ Solarzellen nicht möglich ist, da hier die aktive Schicht aus einem bipolaren, effektiven

Medium besteht. Zum Einen werden dadurch einige Voraussetzungen der Mott–Schottky Theorie nicht erfüllt, und zum Anderen zeigte sich eine Abhängigkeit des experimentell bestimmten Mott–Schottky Potentials von der aktiven Schichtdicke, die ebenfalls der Mott–Schottky Theorie widerspricht. Außerdem wurde in dieser Arbeit bereits gezeigt, dass die Diffusionsspannung nicht dem angestrebten Flachbandfall entspricht und daher der QFB eine verlässlichere Definition von Flachbandbedingungen in organischen BHJ Solarzellen darstellt.

Abschließend wurden noch die ersten komplett von Rolle-zu-Rolle auf Papier gedruckten organischen BHJ Solarzellen präsentiert. Diese wurden in Zusammenarbeit mit dem Institut für Print- und Medientechnik der TU Chemnitz im Rahmen des MOPS-Projekts (Massengedruckte Organische Papier-Solarzellen) entwickelt und erzielten dabei Wirkungsgrade von bis zu 1.3%.

# Bibliography

- [1] J. Schindler and W. Zittel. Zukunft der weltweiten Erdölversorgung. Technical report, 2008.
- [2] International Energy Agency. *World Energy Outlook 2010*. Organisation for Economic Co-operation and Development OECD, 1st edition, 2010.
- [3] D. Wedepohl. So viel solarenergie wie noch nie. Technical report, Bundesverband Solarwirtschaft e.V., 2011.
- [4] D. M. Chapin, C. S. Fuller, and G. L. Pearson. A new silicon p-n junction photocell for converting solar radiation into electrical power. *J. Appl. Phys.*, 25(5):676, 1954.
- [5] M. A. Green, K. Emery, Y. Hishikawa, W. Warta, and E. D. Dunlop. *Prog. Photovolt: Res. Appl.*, pages 12–20.
- [6] W. Shockley and H. J. Queisser. Detailed balance limit of efficiency of p-n junction solar cells. *J. Appl. Phys.*, 32(3):510, 1961.
- [7] R. Gaudiana. Third-generation photovoltaic technology – The potential for low-cost solar energy conversion. *J. Phys. Chem. Lett.*, 1(7):1288–1289, 2010.
- [8] C. J. Brabec, S. Gowrisanker, J. J. M. Halls, D. Laird, S. Jia, and S. P. Williams. Polymer-fullerene bulk-heterojunction solar cells. *Adv. Mater.*, 22(34):3839–56, 2010.
- [9] H. Akamatu, H. Inokuchi, and Y. Matsunaga. Electrical conductivity of the Perylene - Bromine complex. *Nature*, 173(4395):168–169, 1954.
- [10] H. Shirakawa, E. J. Louis, A. G. MacDiarmid, C. K. Chiang, and A. J. Heeger. Synthesis of electrically conducting organic polymers: halogen derivatives of polyacetylene, (CH)<sub>x</sub>. *J. Chem. Soc. Chem. Commun.*, pages 578–580, 1977.
- [11] G. Chamberlain. Organic solar cells: A review. *Solar Cells*, 8(1):47–83, 1983.
- [12] C. W. Tang. Two-layer organic photovoltaic cell. *Appl. Phys. Lett.*, 48(2):183, 1986.

- 
- [13] N. S. Sariciftci, L. Smilowitz, A. J. Heeger, and F. Wudl. Photoinduced electron transfer from a conducting polymer to buckminsterfullerene. *Science*, 258(5087):1474–6, 1992.
- [14] G. Yu, J. Gao, J. C. Hummelen, F. Wudl, and A. J. Heeger. Polymer photovoltaic cells: Enhanced efficiencies via a network of internal donor-acceptor heterojunctions. *Science*, 270(5243):1789, 1995.
- [15] S. E. Shaheen, C. J. Brabec, N. S. Sariciftci, F. Padinger, T. Fromherz, and J. C. Hummelen. 2.5% efficient organic plastic solar cells. *Appl. Phys. Lett.*, 78(6):841, 2001.
- [16] J. Peet, J. Y. Kim, N. E. Coates, W. L. Ma, D. Moses, A. J. Heeger, and G. C. Bazan. Efficiency enhancement in low-bandgap polymer solar cells by processing with alkane dithiols. *Nature Mater.*, 6(7):497–500, 2007.
- [17] F. Padinger, R. S. Rittberger, and N. S. Sariciftci. Effects of postproduction treatment on plastic solar cells. *Adv. Funct. Mater.*, 13(1):85–88, 2003.
- [18] M. Jørgensen, K. Norrman, and F. C. Krebs. Stability/degradation of polymer solar cells. *Sol. Energ. Mat. Sol. C.*, 92(7):686–714, 2008.
- [19] M. Jørgensen, K. Norrman, S. A. Gevorgyan, T. Tromholt, B. Andreasen, and F. C. Krebs. Stability of Polymer Solar Cells. *Adv. Mater.*, 24:580–612, 2011.
- [20] C. Deibel and V. Dyakonov. Polymer-fullerene bulk heterojunction solar cells. *Rep. Prog. Phys.*, 73(9):096401, 2010.
- [21] R. A. Marcus. On the theory of oxidation-reduction reactions involving electron transfer. I. *J. Chem. Phys.*, 24(5):966, 1956.
- [22] A. Miller. Impurity conduction at low concentrations. *Phys. Rev.*, 257(3):745–755, 1960.
- [23] R. A. Marcus. Electron transfer reactions in chemistry. Theory and experiment. *Rev. Mod. Phys.*, 65(3):599–610, 1993.
- [24] F. Schmidlin. Theory of trap-controlled transient photoconduction. *Phys. Rev. B*, 16(6):2362–2385, 1977.
- [25] J. Noolandi. Multiple-trapping model of anomalous transit-time dispersion in a-Se. *Phys. Rev. B*, 16(10):4466–4473, 1977.

- [26] D. Monroe. Hopping in exponential band tails. *Phys. Rev. Lett.*, 54(2):146–149, 1985.
- [27] S. D. Baranovskii, T. Faber, and F. Hensel. On the Einstein relation for hopping electrons. *J. Non-Crystal. Sol.*, 227-230:158–161, 1998.
- [28] H. Bässler. Charge transport in disordered organic photoconductors. *Phys. Stat. Sol.*, 175(15):15–56, 1993.
- [29] H. Bässler and A. Köhler. Charge transport in organic semiconductors. *Top. Curr. Chem.*, 312(October 2011):1–65, 2012.
- [30] J. Frenkel. On the transformation of light into heat in solids. I. *Phys. Rev.*, 37(1):17–44, 1931.
- [31] J. Frenkel. On the transformation of light into heat in solids. II. *Phys. Rev.*, 37(10):1276–1294, 1931.
- [32] H. Hertz. Ueber einen Einfluss des ultravioletten Lichtes auf die elektrische Entladung. *Ann. Phys.*, 267(8):983–1000, 1887.
- [33] A. Einstein. Über einen die Erzeugung und Verwandlung des Lichtes betreffenden heuristischen Gesichtspunkt. *Ann. Phys.*, 322(6):132–148, 1905.
- [34] D. Rauh, A. Wagenpfahl, C. Deibel, and V. Dyakonov. Relation of open circuit voltage to charge carrier density in organic bulk heterojunction solar cells. *Appl. Phys. Lett.*, 98:133301, 2011.
- [35] V. Shrotriya, G. Li, Y. Yao, T. Moriarty, K. Emery, and Y. Yang. Accurate measurement and characterization of organic solar cells. *Adv. Funct. Mater.*, 16(15):2016–2023, 2006.
- [36] S. Hegedus, D. Desai, and C. Thompson. Voltage dependent photocurrent collection in CdTe/CdS solar cells. *Prog. Photovolt: Res. Appl.*, 15(7):587–602, 2007.
- [37] D. Hertel and H. Bässler. Photoconduction in amorphous organic solids. *ChemPhysChem*, 9(5):666–88, 2008.
- [38] C. J. Brabec, V. Dyakonov, and U. Scherf. *Organic Photovoltaics: Materials, Device Physics, and Manufacturing Technologies*. Wiley-VCH, 1st edition, 2008.



- [39] C. Deibel, D. Mack, J. Gorenflot, D. Rauh, and V. Dyakonov. Energetics of excited states in the conjugated polymer poly(3-hexylthiophene). *Phys. Rev. B*, 81(8):1–5, 2010.
- [40] L. Lüer. Oxygen-induced quenching of photoexcited states in polythiophene films. *Organic Electronics*, 5(1-3):83–89, 2004.
- [41] P. E. Shaw, A. Ruseckas, and I. D. W. Samuel. Exciton diffusion measurements in poly(3-hexylthiophene). *Adv. Mater.*, 20(18):3516–3520, 2008.
- [42] I. W. Hwang, D. Moses, and A. J. Heeger. *J. Phys. Chem. C*, (11):4350–4354.
- [43] L. Onsager. Initial recombination of ions. *Phys. Rev.*, 54:554–557, 1938.
- [44] L. C. Braun. Electric field assisted dissociation of charge transfer states as a mechanism of photocarrier production. *J. Chem. Phys.*, 80(9):4157–4161, 1983.
- [45] R. M. Fuoss and F. Accascina. *Electrolytic Conductance*. 1959.
- [46] P. Langevin, D. S. Lemons, and A. Gythiel. On the theory of brownian motion. *C. R. Acad. Sci. (Paris)*, 146:530, 1908.
- [47] C. Deibel, T. Strobel, and V. Dyakonov. Role of the charge transfer state in organic donor-acceptor solar cells. *Adv. Mater.*, 22(37):4097–111, 2010.
- [48] R. Sokel and R. C. Hughes. Numerical analysis of transient photoconductivity in insulators. *J. Appl. Phys.*, 53(11):7414–7424, 1982.
- [49] C. Deibel, A. Wagenpfahl, and V. Dyakonov. Influence of charge carrier mobility on the performance of organic solar cells. *Phys. Stat. Sol. (RRL)*, 2(4):175–177, 2008.
- [50] V. Mihailechi, L. Koster, J. Hummelen, and P. Blom. Photocurrent generation in polymer-fullerene bulk heterojunctions. *Phys. Rev. Lett.*, 93(21):19–22, 2004.
- [51] M. Limpinsel, A. Wagenpfahl, M. Mingebach, and C. Deibel. Photocurrent in bulk heterojunction solar cells. *Phys. Rev. B*, 81(8):085203, 2010.
- [52] M. Pope and C. E. Swenberg. *Electronic processes in organic crystals and polymers*. Oxford University Press, 2nd edition, 1999.

- [53] S. De, T. Pascher, M. Maiti, K. G. Jespersen, T. Kesti, F. Zhang, O. Inganäs, A. Yartsev, and V. Sundström. Geminate charge recombination in alternating polyfluorene copolymer/fullerene blends. *J. Am. Chem. Soc.*, 129(27):8466–72, 2007.
- [54] D. Veldman, O. Ipek, S. C. J. Meskers, J. Sweelssen, M. M. Koetse, S. C. Veenstra, J. M. Kroon, S. S. van Bavel, J. Loos, and R. A. J. Janssen. Compositional and electric field dependence of the dissociation of charge transfer excitons in alternating polyfluorene copolymer/fullerene blends. *J. Am. Chem. Soc.*, 130(24):7721–35, 2008.
- [55] J. Kern, S. Schwab, C. Deibel, and V. Dyakonov. Binding energy of singlet excitons and charge transfer complexes in MDMO-PPV:PCBM solar cells. *Phys. Status Solidi RRL*, 5(10-11):364–366, 2011.
- [56] M. Hallermann, S. Haneder, and E. Da Como. Charge-transfer states in conjugated polymer/fullerene blends: Below-gap weakly bound excitons for polymer photovoltaics. *Appl. Phys. Lett.*, 93(5):053307, 2008.
- [57] J.-L. Brédas, J. E. Norton, J. Cornil, and V. Coropceanu. Molecular understanding of organic solar cells: The challenges. *Acc. Chem. Res.*, 42(11):1691–9, 2009.
- [58] I. A. Howard and F. Laquai. Optical probes of charge generation and recombination in bulk heterojunction organic solar cells. *Macromol. Chem. Phys.*, 211(19):2063–2070, 2010.
- [59] C. G. Shuttle, B. O'Regan, A. M. Ballantyne, J. Nelson, D. D. C. Bradley, J. de Mello, and J. R. Durrant. Experimental determination of the rate law for charge carrier decay in a polythiophene:fullerene solar cell. *Appl. Phys. Lett.*, 92(9):093311, 2008.
- [60] G. Juška, K. Genevičius, N. Nekrašas, G. Sliaužys, and G. Dennler. Tri-molecular recombination in polythiophene:fullerene bulk heterojunction solar cells. *Appl. Phys. Lett.*, 93(14):143303, 2008.
- [61] C. Deibel, A. Baumann, and V. Dyakonov. Polaron recombination in pristine and annealed bulk heterojunction solar cells. *Appl. Phys. Lett.*, 93(16):163303, 2008.
- [62] A. Foertig, A. Baumann, D. Rauh, V. Dyakonov, and C. Deibel. Charge carrier concentration and temperature dependent recombination in polymer-fullerene solar cells. *Appl. Phys. Lett.*, 95(5):052104, 2009.

- [63] P. Langevin. Recombinaison et mobilités des ions dans les gaz. *Ann. Chim. Phys.*, 28:433, 1903.
- [64] C. Deibel, A. Wagenpfahl, and V. Dyakonov. Origin of reduced polaron recombination in organic semiconductor devices. *Phys. Rev. B*, 80(7):1–7, 2009.
- [65] N. Sivaraman, R. Dhamodaran, I. Kaliappan, T. G. Srinivasan, P. R. V. Rao, and C. K. Mathews. *J. Org. Chem.*, (22):6077–6079.
- [66] M. M. Wienk, J. M. Kroon, W. J. H. Verhees, J. Knol, J. C. Hummelen, P. A. van Hal, and R. A. J. Janssen. Efficient methano[70]fullerene/MDMO-PPV bulk heterojunction photovoltaic cells. *Angew. Chem., Int. Ed.*, 42(29):3371–5, 2003.
- [67] X. Gong, M. Tong, F. G. Brunetti, J. Seo, Y. Sun, D. Moses, F. Wudl, and A. J. Heeger. Bulk heterojunction solar cells with large open-circuit voltage: electron transfer with small donor-acceptor energy offset. *Adv. Mater.*, (20):2272–7.
- [68] S. D. Dimitrov, C. B. Nielsen, S. Shoaee, P. S. Tuladhar, J. Du, I. McCulloch, and J. R. Durrant. Efficient charge photogeneration by the dissociation of PC<sub>70</sub>BM excitons in polymer/fullerene solar cells. *J. Phys. Chem. Lett.*, 3(1):140–144, 2012.
- [69] T. J. Savenije, J. E. Kroeze, X. Yang, and J. Loos. The effect of thermal treatment on the morphology and charge carrier dynamics in a polythiophene-fullerene bulk heterojunction. *Adv. Func. Mater.*, 15(8):1260–1266, 2005.
- [70] Z. E. Ooi. *On the corrected photocurrent of organic bulk heterojunction solar cells*. Dissertation, Imperial College London, 2008.
- [71] Z. E. Ooi, R. Jin, J. Huang, Y. F. Loo, A. Sellinger, and J. C. DeMello. On the pseudo-symmetric current-voltage response of bulk heterojunction solar cells. *J. Mater. Chem.*, 18(14):1644, 2008.
- [72] I. Riedel, J. Parisi, V. Dyakonov, L. Lutsen, D. Vanderzande, and J. C. Hummelen.
- [73] J. Mort, I. Chen, A. Troup, M. Morgan, J. Knights, and R. Lujan. *Phys. Rev. Lett.*, (16):1348–1351.
- [74] J. Mort, I. Chen, M. Morgan, and S. Grammatica. Geminate and nongeminate recombination in a-As<sub>2</sub>Se<sub>3</sub>. *Solid State Commun.*, 39:1329–1331, 1981.

- [75] D. Hertel, E. V. Soh, B. Heinz, and L. J. Rothberg. Electric field dependent generation of geminate electron-hole pairs in a ladder-type pi-conjugated polymer probed by fluorescence quenching and delayed field collection of charge carriers. *Chem. Phys. Lett.*, 361:99–105, 2002.
- [76] T. Offermans, S. C. J. Meskers, and R. A. J. Janssen. Time delayed collection field experiments on polymer:fullerene bulk-heterojunction solar cells. *J. Appl. Phys.*, 100(7):074509, 2006.
- [77] J. Kniepert, M. Schubert, J. C. Blakesley, and D. Neher. *Phys. Chem. Lett.*, pages 700–705.
- [78] E. Barsoukov and J. R. Macdonald. *Impedance Spectroscopy: Theory, Experiment, and Applications*. Wiley-Interscience, second edition, 2005.
- [79] K. S. Cole and R. H. Cole. Dispersion and absorption in dielectrics I. alternating current characteristics. *J. Chem. Phys.*, 9(4):341, 1941.
- [80] N. F. Mott. Note on copper-cuprous oxide photocells. *Proc. R. Soc. Lond. A*, 171(946):281–285, 1939.
- [81] W. Schottky. Zur Halbleitertheorie der Sperrschicht- und Spitzengleichrichter. *Z. Phys. A*, 367:367–414, 1939.
- [82] W. Schottky. Vereinfachte und erweiterte Theorie der Randschichtgleichrichter. *Z. Phys. A*, 539:539–592, 1942.
- [83] S. M. Sze and N. Kwok. *Physics of Semiconductor Devices*. Wiley-Interscience, 3rd edition, 2007.
- [84] J. Bisquert, G. Garcia-Belmonte, A. Munar, M. Sessolo, A. Soriano, and H. J. Bolink. Band unpinning and photovoltaic model for P3HT:PCBM organic bulk heterojunctions under illumination. *Chem. Phys. Lett.*, 465(1-3):57–62, 2008.
- [85] G. Garcia-Belmonte, A. Munar, E. Barea, J. Bisquert, I. Ugarte, and R. Pacios. Charge carrier mobility and lifetime of organic bulk heterojunctions analyzed by impedance spectroscopy. *Org. Electron.*, 9(5):847–851, 2008.
- [86] J. C. Nolasco, A. Sánchez-Díaz, R. Cabré, J. Ferré-Borrull, L. F. Marsal, E. Palomares, and J. Pallarès. Relation between the barrier interface and the built-in potential in pentacene/C<sub>60</sub> solar cell. *Appl. Phys. Lett.*, 97(1):013305, 2010.

- [87] D. Ray, L. Burtone, K. Leo, and M. Riede. Detection of trap charge in small molecular organic bulk heterojunction solar cells. *Phys. Rev. B*, 82(12):125204, 2010.
- [88] P. P. Boix, G. Garcia-Belmonte, U. Muñecas, M. Neophytou, C. Waldauf, and R. Pacios. Determination of gap defect states in organic bulk heterojunction solar cells from capacitance measurements. *Appl. Phys. Lett.*, 95(23):233302, 2009.
- [89] L. J. A. Koster, V. D. Mihailetschi, and P. W. M. Blom. Ultimate efficiency of polymer/fullerene bulk heterojunction solar cells. *Appl. Phys. Lett.*, 88(9):093511, 2006.
- [90] P. Schilinsky, C. Waldauf, J. Hauch, and C. J. Brabec. Simulation of light intensity dependent current characteristics of polymer solar cells. *J. Appl. Phys.*, 95(5):2816, 2004.
- [91] M. Limpinsel. *Investigation of the photocurrent in organic bulk heterojunction solar cells*. PhD thesis, University of Würzburg, 2009.
- [92] V. D. Mihailetschi, P. W. M. Blom, J. C. Hummelen, and M. T. Rispens. Cathode dependence of the open-circuit voltage of polymer:fullerene bulk heterojunction solar cells. *J. Appl. Phys.*, 94(10):6849, 2003.
- [93] M. C. Scharber, D. Mühlbacher, M. Koppe, P. Denk, C. Waldauf, A. J. Heeger, and C. J. Brabec. Design rules for donors in bulk-heterojunction solar cells - Towards 10 % energy-conversion efficiency. *Adv. Mater.*, 18(6):789–794, 2006.
- [94] R. J. de Vries, S. L. M. van Mensfoort, R. A. J. Janssen, and R. Coehoorn. Relation between the built-in voltage in organic light-emitting diodes and the zero-field voltage as measured by electroabsorption. *Phys. Rev. B*, 81(12):1–5, 2010.
- [95] J. G. Simmons. *J. Phys. Chem. Solids*, (8):1987–1999.
- [96] I. Lange, J. Blakesley, J. Frisch, A. Vollmer, N. Koch, and D. Neher. Band bending in conjugated polymer layers. *Phys. Rev. Lett.*, 106(21):1–4, 2011.
- [97] M. Kemerink, J. M. Kramer, H. H. P. Gommans, and R. A. J. Janssen. Temperature-dependent built-in potential in organic semiconductor devices. *Appl. Phys. Lett.*, 88(19):192108, 2006.

- [98] M. Mingeback, C. Deibel, and V. Dyakonov. Built-in potential and validity of the Mott-Schottky analysis in organic bulk heterojunction solar cells. *Phys. Rev. B*, 84(15):153201, 2011.
- [99] W. Ma, C. Yang, X. Gong, K. Lee, and A. J. Heeger. Thermally atable, efficient polymer solar cells with nanoscale control of the interpenetrating network morphology. *Adv. Funct. Mater.*, 15(10):1617–1622, 2005.
- [100] A. Baumann, J. Lorrmann, C. Deibel, and V. Dyakonov. Bipolar charge transport in poly(3-hexyl thiophene)/methanofullerene blends: A ratio dependent study. *Appl. Phys. Lett.*, 93(25):252104, 2008.
- [101] J. Guo, H. Ohkita, H. Benten, and S. Ito. Charge generation and recombination dynamics in poly(3-hexylthiophene)/ fullerene blend films with different regioregularities and morphologies. (6):6154–6164, 2010.
- [102] C. Deibel, T. Strobel, and V. Dyakonov. Origin of the efficient polaron-pair dissociation in polymer-fullerene blends. *Phys. Rev. Lett.*, 103(3):1–4, 2009.
- [103] V. I. Arkhipov, P. Heremans, and H. Bässler. Why is exciton dissociation so efficient at the interface between a conjugated polymer and an electron acceptor? *Appl. Phys. Lett.*, 82(25):4605, 2003.
- [104] C. Deibel. Charge carrier dissociation and recombination in polymer solar cells. *Phys. Status solidi A*, 2736(12), 2009.
- [105] M. Mingeback, S. Walter, V. Dyakonov, and C. Deibel. Direct and charge transfer state mediated photogeneration in polymer-fullerene bulk heterojunction solar cells. *Appl. Phys. Lett.*, 100(19):193302, 2012.
- [106] R. A. Street and M. Schoendorf. Interface state recombination in organic solar cells. *Phys. Rev. B*, 81(20):1–12, 2010.
- [107] C. Deibel and A. Wagenpfahl. Comment on "Interface state recombination in organic solar cells". *Phys. Rev. B*, 82(20):1–4, 2010.
- [108] A. A. Bakulin, A. Rao, V. G. Pavelyev, P. H. M. van Loosdrecht, M. S. Pshenichnikov, D. Niedzialek, J. Cornil, D. Beljonne, and R. H. Friend. The role of driving energy and delocalized states for charge separation in organic semiconductors. *Science*, 335:1340, 2012.
- [109] G. Dennler, A. J. Mozer, G. Juška, A. Pivrikas, R. Österbacka, A. Fuchs-bauer, and N. S. Sariciftci. Charge carrier mobility and lifetime versus composition of conjugated polymer/fullerene bulk-heterojunction solar cells. *Org. Electron.*, 7(4):229–234, 2006.

- [110] A. Mozer, G. Dennler, N. Sariciftci, M. Westerling, A. Pivrikas, R. Österbacka, and G. Juška. Time-dependent mobility and recombination of the photoinduced charge carriers in conjugated polymer/fullerene bulk heterojunction solar cells. *Phys. Rev. B*, 72(3):1–10, 2005.
- [111] L. J. A. Koster, V. D. Mihailetschi, and P. W. M. Blom. Bimolecular recombination in polymer/fullerene bulk heterojunction solar cells. *Appl. Phys. Lett.*, 88(7):052104, 2006.
- [112] A. Pivrikas, G. Juška, A. Mozer, M. Scharber, K. Arlauskas, N. S. Sariciftci, H. Stubb, and R. Österbacka. Bimolecular recombination coefficient as a sensitive testing parameter for low-mobility solar-cell materials. *Phys. Rev. Lett.*, 94(17):1–4, 2005.
- [113] G. J. Adriaenssens and V. I. Arkhipov. Non-Langevin recombination in disordered materials with random potential distributions. *Solid State Commun.*, 103(9):541–543, 1997.
- [114] S. Walter. *Photogeneration and recombination in organic bulk heterojunction solar cells*. PhD thesis, University of Würzburg, 2012.
- [115] M. C. Scharber, M. Koppe, J. Gao, F. Cordella, M. A. Loi, P. Denk, M. Morana, H.-J. Egelhaaf, K. Forberich, G. Dennler, R. Gaudiana, D. Waller, Z. Zhu, X. Shi, and C. J. Brabec. Influence of the bridging atom on the performance of a low-bandgap bulk heterojunction solar cell. *Adv. Mater.*, 22(3):367–70, 2010.
- [116] M. Morana, H. Azimi, G. Dennler, H.-J. Egelhaaf, M. Scharber, K. Forberich, J. Hauch, R. Gaudiana, D. Waller, Z. Zhu, K. Hingerl, S. S. van Bavel, J. Loos, and C. J. Brabec. Nanomorphology and charge generation in bulk heterojunctions based on low-bandgap dithiophene polymers with different bridging atoms. *Adv. Funct. Mater.*, 20(7):1180–1188, 2010.
- [117] S. Albrecht, W. Schindler, J. Kurpiers, J. Kniepert, J. C. Blakesley, I. Dumsch, S. Allard, K. Fostiropoulos, U. Scherf, and D. Neher. On the field dependence of free charge carrier generation and recombination in blends of PCPDTBT/PC<sub>70</sub>BM: Influence of solvent additives. *J. Phys. Chem. Lett.*, 3(5):640–645, 2012.
- [118] G. Malliaras, J. Salem, P. Brock, and C. Scott. Electrical characteristics and efficiency of single-layer organic light-emitting diodes. *Phys. Rev. B*, 58(20):R13411–R13414, 1998.

- [119] A. Hübler, B. Trnovec, T. Zillger, M. Ali, N. Wetzold, M. Mingeback, A. Wagenpfahl, C. Deibel, and V. Dyakonov. Printed paper photovoltaic cells. *Adv. Energy Mater.*, 1(6):1018–1022, 2011.
- [120] K. Zweibel. Thin film PV manufacturing: Materials costs and their optimization. *Sol. Energy Mater. & Sol. Cells*, 63(4):375–386, 2000.
- [121] J. Kalowekamo and E. Baker. Estimating the manufacturing cost of purely organic solar cells. *Sol. Energy*, 83(8):1224–1231, 2009.
- [122] M. C. Barr, J. A. Rowehl, R. R. Lunt, J. Xu, A. Wang, C. M. Boyce, S. G. Im, V. Bulović, and K. K. Gleason. Direct monolithic integration of organic photovoltaic circuits on unmodified paper. *Adv. Mater.*, 23(31):3499–3505, 2011.
- [123] D. Tobjörk and R. Österbacka. Paper Electronics. *Adv. Mater.*, 23(17):1935–61, 2011.
- [124] B. Lamprecht, R. Thünauer, M. Ostermann, G. Jakopic, and G. Leising. Organic photodiodes on newspaper. *Phys. Stat. Sol A*, 202(5):R50–R52, 2005.
- [125] F. C. Krebs. All solution roll-to-roll processed polymer solar cells free from indium-tin-oxide and vacuum coating steps. *Org. Electron.*, 10(5):761–768, 2009.
- [126] Y. Galagan, J.-E. J. M. Rubingh, R. Andriessen, C.-C. Fan, P. W. M. Blom, S. C. Veenstra, and J. M. Kroon. *Sol. Energy Mater. & Sol. Cells*, (5):1339–1343.
- [127] R. Søndergaard, M. Hösel, D. Angmo, T. T. Larsen-Olsen, and F. C. Krebs. Roll-to-roll fabrication of polymer solar cells. *Mater. Today*, 15(1):36–49, 2012.
- [128] H.-L. Yip, S. K. Hau, N. S. Baek, and A. K.-Y. Jen. Self-assembled monolayer modified ZnO/metal bilayer cathodes for polymer/fullerene bulk-heterojunction solar cells. *Appl. Phys. Lett.*, 92(19):193313, 2008.
- [129] V. O. Nwoko and H. H. Uhlig. Logarithmic oxidation kinetics of zinc. *J. Electrochem. Soc.*, 112(12):1181, 1965.
- [130] B. Trnovec, M. Stanel, U. Hahn, A. C. Hübler, H. Kempa, R. Sangl, and M. Forster. Coated paper for printed electronics. *Professional Papermaking*, 1:48–51, 2009.



- [131] A. Wagenpfahl, D. Rauh, M. Binder, C. Deibel, and V. Dyakonov. S-shaped current-voltage characteristics of organic solar devices. *Phys. Rev. B*, 82(11):1–8, 2010.
- [132] W. Shockley and W. Read. Statistics of the recombinations of holes and electrons. *Phys. Rev.*, 87(5):835–842, 1952.

# List of Publications

---

## Full Papers

- Paper-1 Textile electrodes as substrates for the electrodeposition of porous ZnO, T. Loewenstein, A. Hastall, **M. Minge**bach, Y. Zimmermann, A. Neudeck, D. Schlettwein *Phys. Chem. Chem. Phys.* **10**, 1844-1847 (2008).
- Paper-2 Polymeric Squaraine Dyes as Electron Donors in Bulk Heterojunction Solar Cells, S. Völker, S. Uemura, **M. Minge**bach, M. Limpinsel, C. Deibel, V. Dyakonov, C. Lambert *Macromol. Chem. Phys.*, **21**, 1098-1108, (2010).  
Selected for the May 17, 2010 issue Front Cover.
- Paper-3 Textile-Compatible Substrate Electrodes with Electrodeposited ZnO - A new Pathway to Textile-Based Photovoltaics, T. Loewenstein, M. Rudolph, **M. Minge**bach, K. Strauch, Y. Zimmermann, A. Neudeck, S. Sensfuss, D. Schlettwein *ChemPhysChem* **11**, 783-788 (2010).
- Paper-4 Photocurrent in bulk heterojunction solar cells, M. Limpinsel, A. Wagenpfahl, **M. Minge**bach, C. Deibel, V. Dyakonov, *Phys. Rev. B*, **81**, 085203, (2010).
- Paper-5 Printed paper photovoltaic cells, A. Hübner, B. Trnovec, T. Zillger, M. Ali, N. Wetzold, **Markus Minge**bach, A. Wagenpfahl, C. Deibel, V. Dyakonov, *Adv. Energy Mater.*, **1**, 1018-1022, (2011).
- Paper-6 Built-in potential and validity of the Mott-Schottky analysis in organic bulk heterojunction solar cells, **M. Minge**bach, C. Deibel, V. Dyakonov, *Phys. Rev. B*, **84**, 153201, (2011).
- Paper-7 Direct and charge transfer state mediated photogeneration in polymer-fullerene bulk heterojunction solar cells, **M. Minge**bach, S. Walter, V. Dyakonov and C. Deibel, *Appl. Phys. Lett.*, **100**, 193302, (2012).

Selected for the May 21, 2012 issue of Virtual Journal of Nanoscale Science & Technology

Paper-8 Influence of the bridging atom in PCPDTBT and Si-PCPDTBT blends on Charge Photogeneration, A. Zusan, **M. Minge**bach, S. Walter, V. Dyakonov and C. Deibel, in preparation

## Contributions to Conferences

### Invited Talks

1. Field- and Temperature Dependence of Charge Photogeneration in Organic Bulk Heterojunction Solar Cells, **M. Minge**bach, S. Walter, J. Lorrmann, J. Kern, S. Schwab, C. Deibel and V. Dyakonov, *Materials Research Society – Fall Meeting in Boston*, I8.3 (2011)

### Talks

1. Pulsed Photocurrent Measurements in Bulk Heterojunction Solar Cells, **M. Minge**bach, M. Limpinsel, A. Wagenpfahl, C. Deibel, V. Dyakonov, *DPG-Frühjahrstagung in Regensburg*, HL17.1 (2010).
2. Pulsed Photocurrent Measurements in Bulk Heterojunction Solar Cells, **M. Minge**bach, M. Limpinsel, A. Wagenpfahl, C. Deibel, V. Dyakonov, *Plastic Electronics in Dresden*, C4.3.01 (2010).
3. Quasi Flat Bands and Built-in Potential in Organic Solar Cells, **M. Minge**bach, A. Wagenpfahl, C. Deibel, V. Dyakonov, *DPG-Frühjahrstagung in Dresden*, HL46.10 (2011).
4. Built-in Potential and Validity of Mott-Schottky Analysis in Organic Bulk Heterojunction Solar Cells, **M. Minge**bach, C. Deibel, V. Dyakonov, *Materials Research Society – Fall Meeting in Boston*, H10.7 (2011)

### Poster presentations

1. Electrodeposition of porous ZnO on textile substrates, **M. Minge**bach, T. Loewenstein, Y. Zimmermann, A. Neudeck, D. Schlettwein, *DPG-Frühjahrstagung in Berlin*, DS17.59 (2008).
2. Hydrodynamic aspects of the electrochemical ZnO deposition, **M. Minge**bach, T. Loewenstein, E. Lorenz, Y. Zimmermann, A. Neudeck,

- D. Schlettwein, *Materialforschungstag Mittelhessen 2008 in Marburg* (2008).
3. Pulsed Photocurrent and Field Dependent Photoluminescence Measurements, **M. Minge**bach, J. Kern, S. Walter, S. Schwab, A. Wagenpfahl, C. Deibel, V. Dyakonov, *Fundamental Function of Organic Solar Cells - Interdisciplinary Workshop in Munich* (2011).
  4. Built-in Potential and Validity of Mott-Schottky Analysis in Organic Bulk Heterojunction Solar Cells, **M. Minge**bach, C. Deibel, V. Dyakonov, *DPG-Frühjahrstagung in Berlin*, CPP6.29 (2012)



## ANHANG B

# Danksagung

---

An dieser Stelle möchte ich mich bei Allen bedanken, die mich während meiner Arbeit am Lehrstuhl der Experimentellen Physik VI begleitet und unterstützt haben. Dabei möchte ich meinen besonderen Dank nochmals an folgende Personen richten:

- Prof. Dr. Vladimir Dyakonov für die Aufnahme an seinem Lehrstuhl, die hier bestehenden exzellenten Voraussetzungen für das Anfertigen meiner Dissertation sowie das Ermöglichen meiner Teilnahme an vielen nationalen und internationalen Konferenzen. Vor allem die intensiven Diskussionen meiner Forschungsergebnisse um sie im Rahmen wissenschaftlicher Tagungen zu präsentieren oder in der Fachliteratur zu veröffentlichen waren sehr hilfreich.
- Prof. Dr. Derck Schlettwein für die Begutachtung dieser Arbeit und auch nochmals für die Betreuung meiner Diplomarbeit an seinem Lehrstuhl.
- PD Dr. Carsten Deibel für seine Betreuung und Unterstützung sowie dafür, dass seine Tür immer offen stand für Fragen und kritische Diskussionen meiner Forschungsergebnisse. Dabei hat er mir immer wieder geholfen bestehende Probleme auch aus neuen Blickwinkeln zu betrachten und zu verstehen.
- Meinen Kollegen Andreas Baumann, Volker Lorrmann und Daniel Rauh für die tolle Atmosphäre im Büro E06 und die allwöchentliche Aufarbeitung des vorangegangenen Bundesligaspieltages.
- Unseren Simulanten Alexander Wagenpahl und Jens Lorrmann für viele interessante Diskussionen zur Interpretation der Messdaten.
- Den Leuten aus dem Transportlabor Alexander Förtig, Andreas Baumann, Andreas Zusan, Jens Lorrmann, Julia Rauh und Maria Hammer für die Unterstützung bei den unterschiedlichen Versuchsaufbauten, der Fehlersuche sowie der anschließenden Diskussion der Messergebnisse.
- Meinen Diplomanden: Moritz Limpinsel für die umfangreiche Unterstützung im Rahmen der Photostrom-Messungen, Alexander Goldmann für

die Hilfe bei der Impedanzspektroskopie und Stefan Walter für die Unterstützung bei den TDCF Messungen sowie für hart umkämpfte Kniffel-Matches während den langen, nächtlichen Mess-Marathons.

- Den Kollegen aus der Photophysik Gruppe Björn Giesecking, Julia Kern, Julien Gorenflot, Moritz Liedtke und ihren Diplomanden für viele anregende Diskussionen.
- Unseren IT-Spezialisten Andreas Sperlich und Hannes Kraus, die für jedes Problem immer die passende Lösung parat hatten.
- André Thiem-Riebe, der immer die Labore (insbesondere die Gloveboxen) am Laufen gehalten und uns immer wieder auf die nötigen Sicherheitsvorkehrungen hingewiesen hat. Weiterhin gilt mein spezieller Dank für die Hilfe bei den REM-Messungen der Papier-Solarzellen am ZAE.
- Valentin Baianov für die Hilfe bei den optischen Versuchsaufbauten um verlässliche Messbedingungen realisieren zu können.
- Diep Phan für die Unterstützung bei der anfallenden Bürokratie, sei es im Rahmen von Projekten, Bestellungen, Dienstreisen oder allen anderen erdenklichen Problemen.
- Dem gesamten Lehrstuhl der EP VI für die tolle Arbeitsatmosphäre und viele Lustige Weihnachts- sowie Grillfeiern.
- Den Chemiker-Gruppen aus Wuppertal und Würzburg um Prof. Dr. Ulrich Scherf (Dr. Michael Forster und Kristina Schottler) bzw. um Prof. Dr. Christoph Lambert (Sebastian Völker) für die gute Zusammenarbeit und das Bereitstellen neuer interessanter Materialien für die Solarzellenproduktion.

Insbesondere möchte ich mich noch bei meinen Eltern Evelyn und Harald Mingebach sowie meinen Geschwistern und Großeltern bedanken. Sie haben mein Studium sowie die daran anschließende Doktorarbeit erst ermöglicht, mich jederzeit unterstützt und immer an mich geglaubt.

ANHANG C

# Curriculum Vitæ

---

## Biographische Daten

Geboren am 10. Januar 1982  
Geburtsort Limburg a. d. Lahn  
Familienstand Ledig  
Nationalität Deutsch

## Kontakt

Arbeit Experimentelle Physik VI  
Physikalisches Institut  
Universität Würzburg  
Am Hubland  
D-97074 Würzburg

Telefon 0931 31 83114

Email [Markus.Mingebach@physik.uni-wuerzburg.de](mailto:Markus.Mingebach@physik.uni-wuerzburg.de)

Privat Rottendorfer Straße 3  
D-97072 Würzburg  
Telefon: 0931 32095990

## Schulbildung

1988–1992 Grundschule, Elz-Süd

1992–2001 Fürst-Johann-Ludwig-Schule Hadamar  
Abitur, Note 2.2 (gut)

## Studium

10/2002–09/2008 Physik (Dipl.-Phys.) an der  
Justus-Liebig-Universität Giessen



- 04/2005 Vordiplom, Note 1.6 (gut)
- 08/2005–06/2006 Auslandsstudium an der Umeå Universität, Schweden
- 12/2007–09/2008 Diplomarbeit am Institut für Angewandte Physik bei Prof. Derck Schlettwein, Justus-Liebig-Universität Gießen  
Thema: *Abscheidung photoaktiven Zinkoxids auf textilen Elektroden*
- 09/2008 Diplom-Physiker (Univ.), Note 1.1 (sehr gut)
- 12/2008– Promotion an der Julius-Maximilians-Universität Würzburg am Lehrstuhl für Experimentelle Physik 6  
Thema: *Photocurrent in Organic Bulk Heterojunction Solar Cells*

### Lehre

- SS 2007 Betreuung Nebenfachpraktikum für Mediziner (Dr. Novotny, Uni Giessen)
- WS 2007/08 Betreuung des Tutoriums Experimentalphysik I für Lehramt und Chemiker (Prof. Schlettwein, Uni Giessen)  
Betreuung Nebenfachpraktikum für Mediziner (Dr. Novotny, Uni Giessen)
- SS 2008 Betreuung des Tutoriums Experimentalphysik I für Lehramt und Chemiker (Prof. Schlettwein, Uni Giessen)
- WS 2009 - 2012 Betreuung Praktikum zur physikalischen Technologie der Materialsynthese (Prof. Pflaum, Uni Würzburg)

### Berufliche Erfahrungen

- 07/2001–04/2002 Zivildienst in der Jugendherberge Limburg a. d. Lahn
- 05/2002–07/2002 Praktikum bei der Deutschen Bundesbank - Hauptverwaltung Frankfurt am Main
- seit 12/2008 Wissenschaftlicher Mitarbeiter der Universität Würzburg

### Stipendien

- 09/2005–06/2006 ERASMUS Auslandsstipendium

ANHANG D

# Erklärung gemäß §5(2) der Promotionsordnung

---

Gemäß §5 Abs. 2 Ziff. 2 und 5 der Promotionsordnung der Fakultät für Physik und Astronomie der Julius-Maximilians-Universität Würzburg.

Hiermit erkläre ich, dass ich die vorliegende Arbeit selbstständig und ohne Hilfe eines Promotionsberaters angefertigt, und keine weiteren als die angegebenen Quellen und Hilfsmittel benutzt habe.

Die Dissertation wurde bisher weder vollständig noch teilweise einer anderen Hochschule mit dem Ziel einen akademischen Grad zu erwerben vorgelegt.

Am 17. September 2008 wurde mir von der Justus-Liebig-Universität Giessen der akademische Grad "Diplom-Physiker" verliehen.

Weitere akademische Grade habe ich weder erworben noch versucht zu erwerben.

(Markus Mingebach)  
Würzburg, den

